
Development of New Sustainable Tool Steel Powders for Additive Manufacturing Processes

Mariana Sofia Teixeira da Cunha

FEUP Supervisor:
Prof. Dr. Manuel Vieira

INEGI Supervisor:
Dr. Omid Emadina

Dissertation submitted to the Faculty of Engineering of the
University of Porto for the degree of Master in
Materials Engineering

Porto, September 2023

This page was intentionally left blank

CANDIDATO Mariana Sofia Teixeira da Cunha

Código 201806584

TÍTULO Development of New Sustainable Tool Steel Powders for Additive Manufacturing Processes

DATA 29 de setembro de 2023

LOCAL Faculdade de Engenharia da Universidade do Porto - Sala F106 - 09:30h

JÚRI Presidente Elsa Sequeiros

DEMM/FEUP

Arguente Ana Reis

DEM/FEUP

Orientador Manuel Vieira

DEMM/FEUP

This page was intentionally left blank

“Curiosity is the engine of achievement.”

Ken Robinson

This page was intentionally left blank

Resumo

Os resíduos metálicos gerados pela indústria da maquinagem passam frequentemente por um processo de downcycling, o que limita bastante o seu potencial para a sua posterior utilização. No entanto, é de grande importância realçar a necessidade de aumentar o valor desses materiais residuais, conferindo-lhes uma utilidade renovada em diversas aplicações. Isto pode ser alcançado pela utilização de métodos de estado sólido e/ou baseados em fusão, exemplificados pela moagem mecânica e atomização a gás, respetivamente, os quais facilitam a criação de matérias-primas adequadas para aplicações de pulverometalurgia. Contudo, deve-se dar máxima atenção à eficiência da produção e às características inerentes dos pós resultantes.

O objetivo deste estudo foi investigar a viabilidade da produção de pós de aço AISI P20+Ni para o fabrico aditivo utilizando aparas metálicas da maquinagem através de moagem mecânica. O processo de produção envolveu dois métodos diferentes, moagem em moinho vibratório de disco (DM) e moagem em moinho de bolas planetário (BM), para produzir pós destinados ao *Direct Energy Deposition* (DED) e fusão seletiva por laser (L-PBF), respetivamente.

O pó destinado ao DED (com tamanho de 38-212 μm) foi produzido utilizando três procedimentos de moagem distintos utilizando DM a uma velocidade constante numa atmosfera não controlada. Para o pó destinado ao L-PBF (com tamanho de 20-53 μm), foi utilizada a técnica BM, onde se aplicou diferentes procedimentos com uma relação constante de esferas para pó (BPR), variando o tempo total de moagem e a velocidade de rotação para maximizar o rendimento do pó na faixa de tamanho requerida e alcançar as características desejadas. Os pós produzidos por DM apresentaram uma morfologia achatada, enquanto os produzidos por BM resultaram numa morfologia arredondada; ambos os procedimentos reduziram com sucesso as aparas para a faixa de tamanho de partícula desejada.

Os pós produzidos por cada método de moagem foram caracterizados para obter mais informações sobre a morfologia, distribuição do tamanho de partícula, capacidade de escoamento, microdureza e presença de defeitos. O pó obtido por DM foi utilizado para imprimir linhas e camadas únicas usando DED. Ao avaliar cuidadosamente a geometria do cordão, diluição e defeitos, a combinação de parâmetros otimizados foi determinada. Com isto, produziu-se um bloco final. O bloco foi submetido a uma análise abrangente, que incluiu a caracterização da microestrutura, mapeamento de microdureza, variação na composição química e identificação de defeitos. Os resultados deste estudo afirmaram que a matéria-prima do aço AISI P20+Ni obtida por meio do processo de reciclagem pode ser utilizada na tecnologia de DED. No entanto, é essencial realçar a necessidade de uma rigorosa atmosfera controlada, durante o processo de moagem e na impressão. Adicionalmente, para garantir a estabilidade da composição química da liga, outras medidas de otimização devem ser cuidadosamente consideradas.

Palavras-chave: Fabrico Aditivo de Metal, Direct Energy Deposition, Sustentabilidade, Moagem Mecânica, Reciclagem, Aparas de Metal, Pós Metálicos, AISI P20+Ni, AISI 4140, Características e Propriedades do Pó, Composição Química, Microdureza.

This page was intentionally left blank

Abstract

Metal residues generated from machining industry often undergoes downcycling, a practice that limits its potential for further use. Nevertheless, it is of great significance to enhance the value of these residual materials, thereby bestowing them with renewed utility in diverse applications. This aspiration can be realized through the adoption of solid-state and/or fusion-based methods, exemplified by mechanical milling and gas atomization, respectively, which facilitate the creation of feedstocks suitable for powder metallurgy applications. Nonetheless, utmost attention must be given to production efficiency and the inherent characteristics of the resultant powders.

The aim of this study was to investigate the feasibility of producing AISI P20+Ni steel powders for additive manufacturing using scrap metal machining chips by mechanical milling. The production process involved two different routes i.e., Vibratory disc milling (DM) and planetary ball milling (BM) to produce powders for Directed energy deposition (DED) and Laser powder bed fusion (L-PBF) respectively.

Powder for DED (sized 38-212 μm) was produced using three different milling procedures employing DM at a constant speed in an un-controlled environment. BM was used to produce powder for L-PBF (sized 20-53 μm) by applying different procedures with a constant ball-to-powder ratio (BPR), varying the total milling time and the rotation speed to maximize the powder yield in the required size range and achieve desired powder characteristics. Powders produced by DM presented a flaky morphology while those produced by BM procedure resulted in a rounded powder morphology; both procedures successfully reducing the chips to desired particle size range.

The powders produced by either processing route were characterized for further insights into the morphology, particle size distribution, flowability, micro-hardness and presence of defects. The powder obtained by DM was utilized for printing lines and single layers using DED. By carefully assessing the bead geometry, dilution, and defects, the optimal combination of laser processing parameters was determined. This ultimately led to the production of a multilayered volume. This volume underwent a comprehensive analysis encompassing characterization of microstructure, microhardness mapping, variation in chemical composition, and identification of defects. The findings of this research affirm that the upcycled AISI P20+Ni feedstock can be utilized in DED printing. However, it is essential to emphasize the necessity for strict atmospheric control both during the milling and printing phase. Additionally, to ensure the stability of the chemical composition in the printed alloy, further optimization measures should be carefully considered.

Key words: Metal Additive Manufacturing; Direct Energy Deposition, Sustainability, Mechanical Milling, Upcycling, Metal Chips, Metal Powders, AISI P20+Ni, AISI 4140, Powder Characteristics and Properties, Chemical Composition, Microhardness.

This page was intentionally left blank

Acknowledgments

First and foremost, I extend my heartfelt gratitude to Dr. Omid Emadinia for his unwavering commitment to this work. His patience, continuous availability, and dedication to elevating the quality of my research have been truly remarkable. His extensive experience and undeniable expertise in the field of metallurgy have played a pivotal role in establishing the solid theoretical foundations of this research. I am deeply grateful of the knowledge he has imparted.

To Prof. Dr. Manuel Vieira for entrusting me with the opportunity to conduct this dissertation in a field I am deeply passionate about, under his expert guidance. I am profoundly grateful for his guidance and vast experience, it contributed significantly to my growth and learning.

To Engineer Lara Castanheira, Engineer Helder Nunes, Engineer Pedro Nunes and Engineer Fahad Zafar for their invaluable contributions to this work. Their extensive experience and unwavering availability for assistance have greatly enriched the project.

To Engineer Jorge Wolfs and Tiago Santos for all the patience and availability during the performance of DED at INEGI.

To Ramiro, Cândida, Aníbal, Maria José and Paula from the Department of Metallurgical and Materials for all the kindness and prompt assistance.

To all my colleagues and friends from DEMM, especially to Bernardo, Beatriz, Francisca, Ricardo, João and Luís, for all the support during our study sessions, for the company and for the motivation during the toughest times.

To all the friends who understand the meaning of “Grupamos”. Your companionship, unwavering support, and the incredible moments we have shared have made these years truly unforgettable.

To Cátia and Telma for the motivation and friendship during these years.

To Bambi, for being my unwavering best friend. Through every up and down in life, Bambi has been a source of comfort and companionship, a loyal presence that has brightened my days.

To my parents and sisters, I owe a debt of gratitude that words can hardly express. Your unwavering love, encouragement, and belief in my abilities have been the foundation upon which my academic pursuits were built. Thank you for always being there, for understanding the challenges I faced, and for celebrating my successes with me. I aspire to one day possess the wisdom and grace that you exemplify.

To Guidinha, whose inspiration has helped shape the person I am today. Thank you for your love and loyalty. I hope I've made you proud.

To Avô Lino for the love and life lessons. I know you will be always looking for me. I hope I've made you proud as well.

This page was intentionally left blank

Institutional Acknowledgments

I gratefully acknowledge CEMUP (Materials Center of the University of Porto) for expert assistance with SEM, and to the Department of Metallurgical and Materials Engineering for providing powder analysis and milling facilities.

I also acknowledge INEGI (Institute of Science and Innovation in Mechanical and Industrial Engineering) for their invaluable expertise and support in the field of Additive Manufacturing.

Finally, I acknowledge to Dr. Alice Marciel from Prifergroup for supplying metal chips.

This page was intentionally left blank

Contents

Resumo	i
Abstract	iii
Acknowledgments	v
Institutional Acknowledgments	vii
List of Abbreviations and Symbols	xiv
Introduction.....	1
1.1 Framework and motivation	1
1.2 Objectives.....	2
1.3 Structure	2
Literature Review	3
2.1 Recycling of Tool Steel Residues from the Metalworking Industries.....	3
2.2 Metal Powders.....	4
2.2.1 Mechanical Milling Processes	4
2.2.2 Powder Characteristics	6
2.2.3 Powder Properties.....	8
2.3 Additive Manufacturing: Direct Energy Deposition.....	10
2.3.1 Process Description	10
2.3.2 Process Applications	11
2.3.3 Printing Parameters	12
2.3.4 Component Analysis.....	15
2.4 Tool Steel Printing through DED	18
Materials and Methods.....	19
3.1 Materials.....	19
3.1.1 AISI P20+Ni Tool Steel	19
3.1.2 AISI 4140 - 42CrMo4 Steel	20
3.2 Powder Production	20
3.2.1 Metal chips.....	20
3.3 Printing through Direct Energy Deposition	25
3.3.1 Selection of Printing Parameters	25
3.3.2 DED Setup	26
3.4 Characterization	27
3.4.1 Microstructural Characterization.....	27

3.4.2 Mechanical characterization	27
Results and Discussion.....	28
4.1 Powder Production	28
4.1.1 Chemical Composition	28
4.2 Powder Production for DED.....	29
4.2.1 Powder Production and Characterization.....	29
4.2.2 Density Measurements.....	33
4.2.3 Flowability Measurements	35
4.3 Powder Production for SLM.....	35
4.3.1 Powder Production and Characterization.....	35
4.3.2 Microhardness Measurements	40
4.4 Printings through Direct Energy Deposition	41
4.4.1 Parametrization Process	41
Conclusions and Future Works	55
5.1 Conclusions	55
5.2 Future Works	56
References	57
Appendices.....	i

List of Figures

Figure 2.1 - Grinding bodies of a disc mill. Adapted from [8].....	5
Figure 2.2 - Working principle of planetary ball milling [10].....	6
Figure 2.3 - Typical powder particle shapes, according to ISO 3252:2019 [12].....	6
Figure 2.4 - Particle Aspect Ratio Definition [13].	7
Figure 2.5 - Scheme of the powder-fed DED process [30].....	10
Figure 2.6 - Scheme of the wire-fed DED process [30].	11
Figure 2.7 - Printing strategies for DED [33].	13
Figure 2.8 - Hatch spacing and overlapping between two printed lines. Adapted from [35].	14
Figure 2.9 - Cross section of a single layer deposition and geometrical properties: d - depth, h - height, w - width, θ - wet angle, A_p - printed area and A_m - melted area. Adapted from [40].	15
Figure 2.10 - Typical shapes of the melted area. Adapted from [42].	16
Figure 2.11 - Gaussian distribution for the laser energy and for the particles for a lateral nozzle. Adapted from [43].	17
Figure 2.12 - Wetting angle variation with interfacial energies. Adapted from [43]	17
Figure 3.1- a) AISI P20+Ni Metal Chips supplied by metalworking industry. b) SEM image of metal chip used for SEM-EDS and microhardness measurements.	21
Figure 3.2- Milling conditions carried out in the current study using dic type	22
Figure 3.3 - DED equipment used for the printings.	26
Figure 4.1 - Particles after 5 minutes of milling.	29
Figure 4.2 - Milled chips content in wt. % for each condition... ..	29
Figure 4.3 - Particle size distribution for PND 1, measured by Image J.... ..	31
Figure 4.4 - SEM image of particles with a size between 38 μm and 212 μm resultant from PND 1	32
Figure 4.5 - SEM image of polished powder particle in the size range of 38 μm to 212 μm from PND 1.... ..	32
Figure 4.6 - SEM image of particles with a size between 38 μm and 212 μm resultant from PND 2.... ..	33
Figure 4.7 - Comparison between the tap and loose density for PND 1.....	34
Figure 4.8 - Milled chips content in wt. % for each condition.... ..	36
Figure 4.9 - Particle size distribution for PNB 5, measured with Image J.... ..	37
Figure 4.10 - SEM images of particles with a size between 20 μm and 53 μm resultant from a) PNB 2, b) PNB 3, c) PNB 4 and d) PNB 5.... ..	38
Figure 4.11 - SEM images of: a) particles with a size between 20 μm and 53 μm resultant for PNB 5. b) polished particles with a size between 20 μm and 53 μm resultant for PNB 5.....	40
Figure 4.12 - Top views of the first 8 printed lines.... ..	42
Figure 4.13 - Cross section views of the first 8 printed lines.....	43
Figure 4.14 - Top views of lines 9 to 19.... ..	44
Figure 4.15 - Cross section views of lines 9 to 19.... ..	45
Figure 4.16 - Top view of the layers with combination of parameters from line 16 with: a) 40% overlapping, b) 50% overlapping and c) 60% overlapping.....	47

Figure 4.17 - Cross section view of the layers with combination of parameters from line 16 with: a) 40% overlapping, b) 50% overlapping and c) 60% overlapping.....	47
Figure 4.18 - Top and Cross-section views of the layers with combination of parameters from line 16 (laser power of 1900 W) with: a) 50% overlapping, b) 60% overlapping, c) 50% overlapping and c) 60% overlapping..	48
Figure 4.19 - Printed multilayered volume with the optimized parameters..	49
Figure 4.20 - Cross section view of the printed multilayered volume.....	50
Figure 4.21 - SEM-BEI images of the porosities of the printed multilayered volume.	51
Figure 4.22 - OM images of the deposited material.....	51
Figure 4.23 - Chemical Composition Profile for the printed multilayered volume ..	52
Figure 4.24 - SEM images from the top surface of the deposited material AISI P20+Ni material	53
Figure 4.25 - Microhardness along the printed multilayered volume (deposited material)	54

List of Tables

Table 3.1- Chemical composition (wt. %) of the AISI P20+Ni steel [47].....	19
Table 3.2- AISI P20+Ni steel properties [47,48]	19
Table 3.3- Chemical composition of the AISI 4140 [49]	20
Table 3.4 - AISI 4140 steel properties [49]	20
Table 3.5 - Planetary Ball Milling Procedures (PNB)	23
Table 3.6- Parameters for the AISI P20+Ni printings.....	25
Table 3.7 - Common parameters used for the AISI P20+Ni printings.	26
Table 4.1 - Semi-quantitative chemical composition (wt. %) of metal chips and powder particles (except C and S)	28
Table 4.2 - D ₁₀ , D ₅₀ and D ₉₀ values for PND 1	31
Table 4.3 - Loose density results for PND 1	33
Table 4.4 - Tap density results for PND 1	34
Table 4.5 - Flowability results for PND 1	35
Table 4.6 - D ₁₀ , D ₅₀ and D ₉₀ values for PNB 5, according to Image J measurements.	37
Table 4.7 - Microhardness of the chips and powder particles	40
Table 4.8 - Printing parameters according to the literature review, combined considering the Taguchi L9	42
Table 4.9 - Geometrical measurement results of the first 8 printed lines.	43
Table 4.10 - Printing parameters for lines 17 to 19.....	44
Table 4.11 - Geometrical measurement results of lines 9 to 19.	46
Table 4.12 - Combination of printing parameters and porosity area for one-layered printing samples.....	49
Table 4.13 - Chemical composition of different parts of the printed block.....	52

List of Abbreviations and Symbols

Abbreviations

AM	Additive Manufacturing
AR	Aspect Ratio
ASTM	American Society for Testing and Materials
BCC	Body-centred cubic
BPR	Ball-to-Powder Ratio
CAD	Computer-aided design
DED	Direct Energy Deposition
DM	Vibratory Disc Milling
DOE	Design of Experiments
EBSD	Electron Backscatter Diffraction
EDS	Energy Dispersive Spectroscopy
FCC	Face Centred Cubic
HAZ	Heat Affected Zone
INEGI	Institute of Science and Innovation in Mechanical and Industrial Engineering
LD	Laser Diffraction
L-PBF	Laser Powder Bed Fusion
MAM	Metal Additive Manufacturing
OM	Optical Microscope
PBM	Planetary Ball Milling
PCA	Process Control Agent
PSA	Particle Size Analyzer
PND	Disc Milling Procedure
PNB	Planetary Ball Milling Procedure
SEM	Scanning Electron Microscopy
SLM	Selective Laser Melting
SLS	Static Light Scattering
SM	Stereoscopic Macroscope

List of Abbreviations and Symbols

Abbreviations

TEM	Transmission Electron Microscopy
XRD	X-ray diffraction
XRF	X-ray fluorescence spectrometry

List of Abbreviations and Symbols

Symbols

A_m	Melted Area
A_p	Printed Area
d	Depth
D	Dilution
FR	Powder Feed Rate
h	Height
M	Mass
P	Power
SS	Scanning Speed
V	Volume
w	Width
γ_{LV}	Interface liquid-vapor
γ_{SL}	Interface solid-liquid
γ_{SV}	Interface solid-vapor
φ	Laser Spot Size
θ	Wetting Angle

Introduction

1.1 Framework and motivation

In recent years, there has been a growing interest in Metal Additive Manufacturing (MAM) as a viable alternative to traditional manufacturing methods for various applications. MAM offers unique capabilities, allowing the production of complex and intricate three-dimensional structures that would be impossible with conventional processes. MAM also enables rapid prototyping and on-demand production, reducing lead times and facilitating agile product development. Additionally, it allows for the creation of lightweight and optimized structures, leading to improved performance and efficiency. This technology minimizes material waste by utilizing only the necessary amount of material, contributing to cost-effectiveness and sustainability. Despite its advantages, MAM processes also come with certain limitations that need to be addressed. Residual stresses resulting from multiple heat cycles, low productivity, high equipment and feedstock costs are issues that require further investigation before widespread industrial application.

In the metalworking industry, significant amounts of metal residues in the form of chips are generated daily. While the conventional approach has been to melt and cast these waste materials in foundry industries, there are more sustainable alternatives with considerable potential. A particularly intriguing process that has captured significant attention is the mechanical milling of wasted chips, transforming them into fine metal powder. This approach holds the potential to revolutionize the AM industry, leading to a substantial reduction in feedstock material costs and paving the way for enhanced sustainability.

The focus of this study is to upcycle AISI P20+Ni scrap chips from metalworking industry by employing disc milling and planetary ball milling technique to produce new raw material as powder feedstock suitable for AM processes. The powder particles are thoroughly characterized in terms of their shape, size, and size distribution. Essential powder properties such as flowability and density are carefully measured, while chemical composition and hardness are also evaluated.

Furthermore, this research investigates the feasibility of printing these powders through Direct Energy Deposition (DED) on a non-preheated AISI 4140 substrate. An exciting potential application of this project in the industry could be the repair of highly machinable components like moulds, offering a practical solution to enhance component life and reduce manufacturing costs.

This dissertation resulted in one accepted conference submission to the third European Conference on the Structural Integrity of Additively Manufactured Materials, ESIAM23 (Appendix A).

1.2 Objectives

This dissertation has a central objective to convert chips into powder particles and subsequently employ the DED process to print AISI P20+Ni tool steel on an AISI 4140 steel substrate, followed by an extensive analysis of the results. The critical steps involved in this work are as follows:

- Extensive literature review encompassing diverse milling methods, powder characterization, powder properties, and additive manufacturing processes, with a particular focus on DED, including parameters and process analysis. The properties of AISI P20+Ni and AISI 4140 steels will be thoroughly examined.
- Transformation of AISI P20+Ni chips into powder particles using disc milling and planetary ball milling. The resultant powder particles will be characterized using sieving methods to evaluate the efficiency of production and size distribution in mass. Additionally, chemical analysis through Energy Dispersive Spectroscopy (EDS) will be carried out. Particle size and shape will be studied through image analysis. Flowability, tap density, and loose density measurements will provide further insights.
- Printing of AISI P20+Ni tool steel on an AISI 4140 steel substrate using DED, considering essential parameters such as laser power, scanning speed, and powder feed rate. The printed lines will be subjected to visual and metallography evaluation from both top and cross-sectional perspectives, respectively.
- Printing of a multilayered volume, followed by comprehensive analyses of its microstructure, chemical composition, and microhardness.

1.3 Structure

This dissertation comprises five distinct chapters. Chapter 1 corresponds to the introduction, providing a comprehensive framework and rationale for the research. It outlines the primary objectives of the dissertation and details the proposed work plan. Moving on to Chapter 2, an extensive literature review is presented. This section lays the foundation for the practical aspects of the study by exploring research on key topics, including mechanical methods for powder production, powder characterization (size, shape, size distribution, flowability, and density), a comprehensive description of the DED process, its parameters, and analysis of previous studies involving AISI P20+Ni or similar steels deposited via DED. In Chapter 3, the materials and methods employed in the research are elucidated in thorough detail. All procedures, tests, equipment, standards, and materials are specified, providing clarity on the experimental setup. The subsequent Chapter 4 is dedicated to the presentation and discussion of the results. Data gathered from the tests described in Chapter 3 are critically examined and analysed, offering insightful discussions and implications. Finally, Chapter 5 offers a concise summary of the conclusions drawn from the study, aligning them with the initial objectives and obtained results. Additionally, this section proposes potential future directions for the research. Suggestions are made for further tests and studies that could either validate the current findings through more specific investigations or expand the scope of the research to explore broader aspects.

Literature Review

2.1 Recycling of Tool Steel Residues from the Metalworking Industries

The global evolution of technology and population growth have influenced society towards a culture of consumerism, leading to significant industrial expansion with notable environmental consequences. These impacts are particularly evident in the steel industry, characterized by extensive mineral consumption, energy generation, and waste production. Recycling metal residues offers a multitude of benefits, including a noteworthy decrease in emissions, energy consumption, and resource usage compared to the production of metals from raw ores [1,2].

The process of recycling one tonne of steel results in the conservation of 1.4 tonnes of iron ore, 0.8 tonnes of coal, 0.3 tonnes of limestone and additives, and 1.67 tonnes of CO₂ emissions. Consequently, the concept of circular economy has gained prominence, focusing on recycling practices and finding innovative approaches to augment value, upcycling, through the development of new applications. [1,3,4].

Tool steel residues can be collected from various sources such as machining operations, tool manufacturing facilities, and metalworking industries. Note it is important to segregate the different types of tool steel residues based on their composition and characteristics to ensure effective recycling. In the context of milling and machining wastes, particularly chip scraps, there is a limited number of recycling methods available. Traditionally, metal scraps are subjected to the process of remelting and casting in foundry industries. However, this approach entails significant energy consumption, contributes to environmental pollution, particularly air contamination, and incurs substantial expenses and labour costs [5].

An alternative method for recycling steel chips involves the utilization of milling processes to produce metal powders. In the study conducted by Fullenwider et al. [6], the focus was on investigating alternative and sustainable approaches to producing feedstock for metal additive manufacturing. Using the ball milling technique, they successfully fabricated steel powders from recycled machining chips. These powders were then employed in additive manufacturing, specifically in laser engineered net shaping, where single tracks were effectively deposited to assess their usability.

In a review conducted by Batista C. et al [2], various mechanical powder production methods were examined, focusing on transforming metal chips into powder particles while considering the characteristics of the powder and the milling conditions. The study concluded that milling processes have the potential to produce powder particles suitable for advanced manufacturing applications such as composite production or additive manufacturing (AM), making it a viable option for repurposing metal chips.

2.2 Metal Powders

This chapter discusses the common methods employed in creating metal powder particles, which involves the mechanical milling process. During this process, metalworking industry scraps are converted into powder particles. The milling process variables are thoroughly examined, along with their impact on powder characteristics such as particle size, shape, size distribution, and structure. The chapter concludes by explaining the crucial properties of powder, including flowability, loose density, and tap density.

2.2.1 Mechanical Milling Processes

Metal powder production techniques are extensively utilized for manufacturing a diverse range of metal powders that are customized to fulfil the specific requirements of various applications. Metal powders can be produced through liquid metal atomization, mechanical, chemical, and electrolytic methods. Liquid metal atomization methods include water and gas atomization, while chemical methods involve oxide reduction, thermal decomposition, or precipitation from solutions [7].

Conversely, mechanical method, typically known as milling method, is a solid-state process that rely on the plastic deformation and subsequent fracturing of cleaned and dried chips/swarf. The fragmentation of particles occurs through compaction or impaction, and the presence or absence of friction depends on the specific milling technique and procedure employed. Additionally, the milling conditions and energy play a crucial role in determining the occurrence of cold welding between particles. Ball milling, disc milling, planetary milling, vibration milling, attritor milling, shaker milling, cryogenic milling, and jet milling are among the most used milling processes. Each technique possesses different capacities, velocities, abilities to minimize powder contamination, and options for process control through temperature adjustments or the addition of additives. Subsequently, after selecting the milling technique, several variables, such as milling time, velocity, container properties, BPR for techniques involving grinding balls, temperature, atmosphere, and process control agents, exert a substantial influence on the evolution of powder characteristics [2,7]. Note that it is important to select the adequate milling technique for a certain goal since it has a high influence in the final powder characteristics.

2.2.1.1 Disc Milling

For this study, the disc milling technique was selected as one of the methods for metallic powder production due to its well-known reputation for high efficiency in transforming industrial chips into metal powders [2]. Figure 2.1 illustrates the arrangement of the grinding bodies and the material disposal in the disc milling process. The particles, positioned between the ring and the grinding jar, undergo fragmentation and destruction through the impact and friction exerted by the disc and/or ring (grinding bodies). This intensity of friction is contingent upon the weight and differential velocity of the grinding bodies. Higher friction levels yield higher fineness and reproducible results in a shorter period [8].

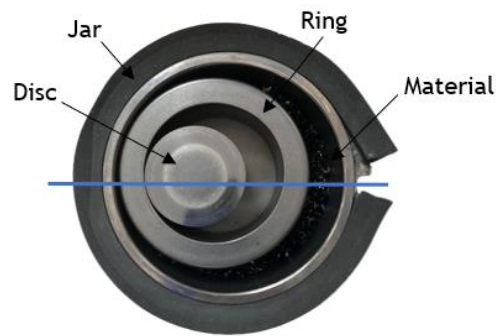


Figure 2.1 - Grinding bodies of a disc mill. Adapted from [8]

In practice, the grinding jar is securely attached to the plate of a vibratory machine, ensuring stability. Moreover, the entire grinding set is enclosed with a cover, providing containment and safety during operation. The plate undergoes circular horizontal vibrations, resulting in a centrifugal force that acts on the grinding bodies, generating high levels of friction, impact, and pressure forces that directly affect the material, leading to its fragmentation [9]. In the practical application, to enhance reproducibility and achieve optimal pulverization, it is important to position the grinding bodies in an eccentric manner and ensure that they make contact at a single point, as illustrated by the blue line in Figure 1. The material should be positioned between the ring and the grinding jar, occupying at most one-third of the total jar volume. Additionally, it is recommended to leave the space between the disc and the ring unoccupied [8].

While disc milling has proven effective for metal powder production from industrial chips, it is important to note that its suitability for AM processes may vary. Further research is required to investigate the impact of disc milling parameters on powder properties relevant to AM, such as particle size distribution, morphology, and flowability.

2.2.1.2 Planetary Ball Milling

Planetary ball milling was another selected technique to produce metallic powders for the present study. The remarkable motion of the planetary ball mill finds its origin in the resemblance to planetary movement exhibited by its vials. These vials are strategically positioned on a rotating support disk, while a specially designed drive mechanism facilitates their rotation along their respective axes. The combined effects of centrifugal force generated by the vials' rotation and the rotating support disk influence the contents of the vials, which include the material to be ground and the grinding balls. Due to the opposing rotational directions of the vials and the supporting disk, the centrifugal forces exert themselves in alternating directions, both similar and opposite. Consequently, this intricate interplay prompts the grinding balls to cascade down the inner wall of the vial, known as the friction effect. Subsequently, the material being ground, and the grinding balls undergo a lifting motion, freely traversing the inner chamber of the vial and colliding with the opposing inner wall, creating an impact effect as it is possible to see in Figure 2.2 [10]. These milling tools are fashioned from resilient materials such as hardened, corrosion-resistant steel, zirconium dioxide, or tungsten carbide, which can withstand the demanding synthesis conditions. Employing such materials

serves to minimize tool degradation and potential contamination of the synthesized compounds [11].

2.2.2 Powder Characteristics

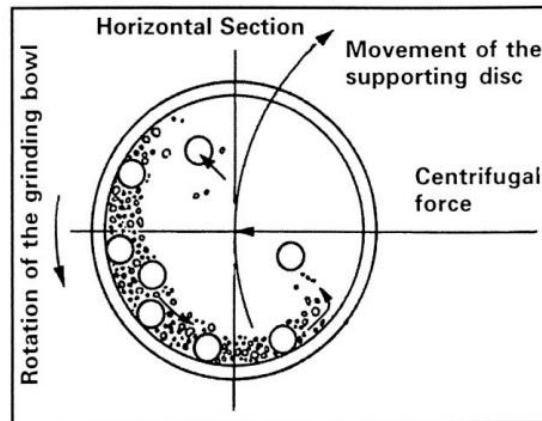


Figure 2.2 - Working principle of planetary ball milling [10]

Prior to using powder in conventional or AM technologies, it is necessary to ensure its suitability for the specific process. Key factors, such as particle size, particle size distribution, particle shape, and particle structure (collectively known as the "4S's"), directly impact the effectiveness of the process and the final properties of the fabricated material or component. Density and flowability are particularly critical properties for powder used in AM technologies. Subsequent chapters will delve into these terms, exploring their implications and influence on the manufacturing processes.

2.2.2.1 Particle Shape

ISO 3252:2019 provides a definition for particle shape, specifically referring to it as the external geometric form of a powder particle [12]. This standard also states the different particle shapes with support of microscopic images, as it is possible to see in Figure 2.3 [12].

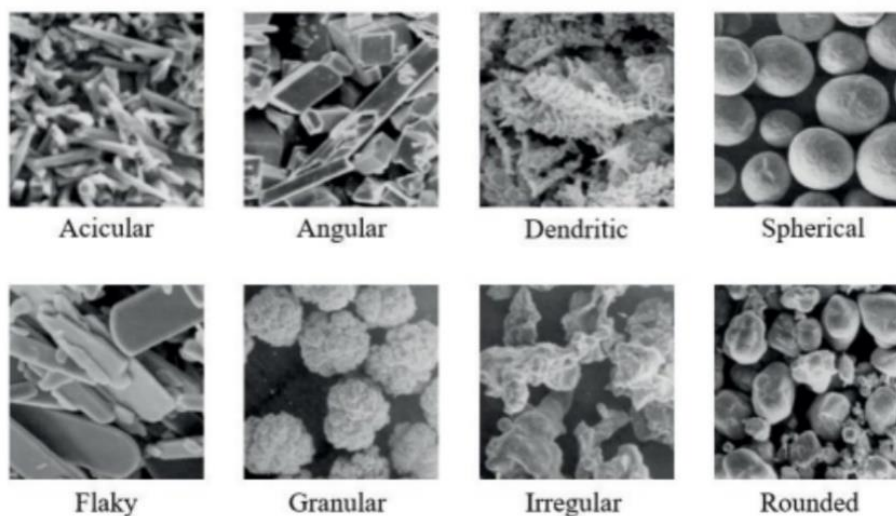


Figure 2.3 - Typical powder particle shapes, according to ISO 3252:2019 [12].

In addition to this qualitative method mentioned above, an interesting method for investigating particle shape involves quantifying the aspect ratio of the particles, which is the ratio of the maximum and minimum particle dimension that passes through the geometric particles centre - Figure 2.4 [13].

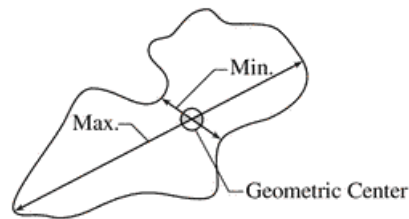


Figure 2.4 - Particle Aspect Ratio Definition [13]

Finally, particle shape is influenced by various factors, including the material properties, milling technique, milling time, ball size or the presence of a process control agent (PCA) [2]. According to a study conducted by Soufiani et al. [14], it was observed that the morphology of milled particles undergoes significant changes with varying milling time. Initially, flake-like shapes are obtained, but as the milling time is extended, the particles transform into spherical shapes. This transformation occurs because of repeated cold welding and fracturing processes taking place during milling. On the other hand, for the same study, it was stated that the milling technique plays a crucial role in determining the shape of the powder particles. Notably, the shaker milling technique was found to produce angular particles that were free from agglomeration, regardless of the milling time [14].

2.2.2.2 Particle Size Distribution

According to ISO 3252:2019, particle size distribution (PSD) is defined as the categorization of a powder sample into different fractions based on size, expressed as a percentage by mass, volume, or numbers [12]. The PSD of a powder plays a significant role in the particle packing behaviour, which, in turn, affects the final density of an additively manufactured component. Additionally, the PSD is believed to have an impact on powder feeding in directed-energy deposition and powder-bed fusion processes [3]. One common method of representing PSD is by using the D_{10} , D_{50} , and D_{90} values of the powder, which represent the maximum particle sizes for 10%, 50%, and 90% of the sample, respectively [2]. The analysis can be performed using various techniques such as sieving, Static Light Scattering (SLS), Scanning Electron Microscopy (SEM), or Laser Diffraction (LD) [2].

Like Particle Shape, PSD can also be influenced by the milling technique employed and the presence of additives, such as process control agents (PCA) or reinforcing materials [2]. Afshari and Ghambari [15] compared jet milling and ball milling and found that jet milling resulted in a narrower and more uniform size distribution compared to ball milling.

Rofman et al. [16] found that the use of stearic acid (SA) as a process control agent (PCA) in the milling process had a profound influence on both the morphology and size distribution of the powder. By adding SA at the early stages of milling, the researchers observed a significant reduction in the powder size distribution. This

indicates that the timing and method of introducing the PCA can effectively control and narrow the particle size distribution during the milling process.

Reinforcements such as Al₂O₃, carbon tungsten (WC), titanium carbide (TiC), silicon carbide (SiC), or niobium carbide (NbC) can also affect the particle size and PSD, with the addition of 3% NbC leading to decreased D₅₀ and D₉₀ values [17].

2.2.2.3 Particle Size

ISO 3252-2019 defines particle size as the “linear dimension of an individual particle as determined by analysis with sieves or other suitable means” [12]. It plays a crucial role in evaluating the extent of fragmentation achieved during the mechanical milling of chips for powder production. Various techniques can be employed to conduct this analysis, including sieving, which provides results in weight percentages. Additionally, image analysis using transmitting optical microscope (OM), stereoscopic macroscope (SM), or scanning electron microscope (SEM) can be utilized. Alternatively, techniques such as static light scattering (SLS), laser particle size analyser (LPSA), or laser diffraction (LD) particle size analyser (PSA) offer alternative means of particle size measurement. Some factors that influence particle size include fragmentation, material characteristics, milling processes and conditions, as well as the presence of additives [2].

2.2.2.4 Particle Structure

Particle structure is a crucial aspect of powder characterization, providing valuable insights into the behaviour and properties of powders. There are various methods available to analyse particle structure, including SEM, Electron Backscatter Diffraction (EBSD), Transmission Electron Microscopy (TEM), Selected Area Diffraction (SAD) mode, and X-ray Diffraction (XRD) [2]. These techniques offer detailed information on the morphology, crystal structure, and particle orientation, facilitating a comprehensive understanding of metal powders.

By employing these diverse analytical techniques, researchers gain profound insights into particle structure and its impact on powder behaviour. This knowledge allows for the optimization of processing conditions and the enhancement of material performance in a wide range of applications.

2.2.3 Powder Properties

2.2.3.1 Flowability

Flowability refers to the inherent ability of powder particles to resist differential movement under the influence of external stress or gravity. This behaviour is governed by several restraining forces, including friction, adhesion (which involves the attraction between particles and container walls), and cohesion (which involves the attraction between particles themselves) [18]. These forces collectively contribute to the overall flow properties of the powder, affecting its ability to flow freely and smoothly.

The flowability of a powder are influenced by various factors, including the characteristics of the powder feedstock. These characteristics encompass the particle size distribution, powder morphology, and surface chemistry. Additionally,

external variables such as humidity, triboelectric charge buildup, and processing history also play a role in determining the flowability of the powder [19].

Powder with spherical particle shapes tend to have higher flowability compared to powder with irregular particle shapes, as they cannot slide past each other with friction or interlocking. However, this advantage diminishes for very fine powders, regardless of their shape, which tend to have low or negligible flowability. On the other hand, larger particles often exhibit higher flowability [19, 20]. Density also plays a role, as higher density correlates with improved flowability. Additionally, ensuring the absence of moisture is crucial, as water can cause particles to adhere together, reducing flowability [19].

The Hall Flow Test is a widely used method for determining the flow rate of metal powders. It involves measuring the time taken for the powder to flow through the orifice of a flowmeter funnel, following the guidelines specified in ASTM Standard Test Method B 213 [21]. In cases where the metal powder fails to pass through the orifice of the Hall Flow funnel, the Carney flow test method is employed, which features a larger orifice size [19, 20]. This alternative method can be conducted in accordance with the ASTM Standard Test Method B 964 [a17].

2.2.3.2 Density

2.2.3.2.1 Bulk Density

Bulk density is a measure of the density of a powder particle and helps identify internal voids within the particle [23]. It is useful for comparing different powder particles, especially those produced through milling processes where internal voids are common. The gas pycnometer is commonly used to measure powder particle density, utilizing gases like helium to reach even the smallest pores [24].

2.2.3.2.2 Loose/Apparent Density

The loose or apparent density refers to the weight per unit volume of a loose powder expressed in grams per cubic centimetre. It is influenced by various factors, including particle size, particle size distribution, particle shape, and particle surface roughness [23]. To determine the loose/apparent density, the ASTM Standard Test Method B212 can be employed using the Hall flowmeter funnel. In cases where powders are non-free flowing, the ASTM Standard Test Method B417 is recommended [25,26].

2.2.3.2.3 Tap Density

Tap density is defined as the density of a powder when the volume container is tapped or vibrated under specified conditions. It is influenced by various factors including particle size distribution, particle shape, and surface roughness, and it is consistently higher than the loose/apparent density due to the compaction process involved [23]. The measurement of tap density is commonly performed using the ASTM Standard Test Method B527 [27].

2.3 Additive Manufacturing: Direct Energy Deposition

AM is an innovative manufacturing process defined by ASTM as the “process of joining materials to make objects from 3D model data, usually layer upon layer, as opposed to subtractive manufacturing methodologies.” [28]. This section focuses on the laser fused DED process, providing an explanation of the process itself.

2.3.1 Process Description

DED is a MAM process that uses a heat source with high energy density, such as a laser, electron beam, or plasma/electric arc, which is directed towards the substrate. This focused heat generates a small melt pool, while concurrently melting the feedstock material introduced into the melt pool. The feedstock material can take the form of either powder or wire [29-31]. Figure 2.5 illustrates a schematic representation of the DED process utilizing laser technology and powder feedstock material.

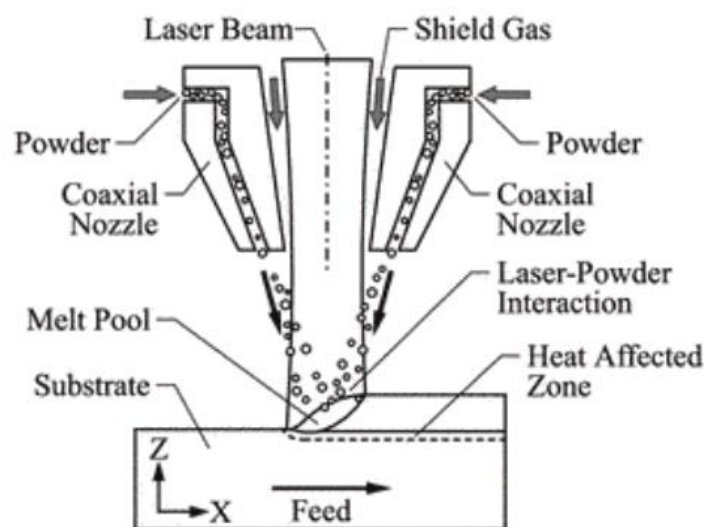


Figure 2.5 - Scheme of the powder-fed DED process [30]

The primary application of directed energy deposition involves the high-speed flow of metal powder through nozzles, which is directed into the focal point of a laser [31]. As the heat source advances, the molten metal undergoes solidification on the substrate or in a previously part, resulting in the formation of a metal track. These tracks overlap each other, aligning with a predetermined hatch spacing, which represents the distance between successive metal tracks. Once a layer is completed, the deposition head and feedstock delivery system move upwards by a small increment, equivalent to the slice thickness. This vertical movement enables the deposition of the subsequent layer. By repeating this layer-by-layer process, a three-dimensional (3D) near-net-shape component is created, closely resembling the computer-aided design (CAD) model. Prior to the deposition process, the 3D digital model is sliced using software to determine the desired slice thickness, hatch spacing, and deposition path for each layer [32].

To safeguard the molten metal from oxidation, a protective shield gas, such as argon or nitrogen, envelops the region where metal deposition takes place. Alternatively, an enclosed chamber filled with inert gas may be utilized to create a controlled environment for the entire build system. One fascinating aspect of the

powder-fed DED process is its capability to deposit multiple materials continuously, without the need to halt the machinery. By incorporating multiple hoppers, different materials can be loaded into each one, enabling the production of parts with diverse composition. This allows the production of functionally graded materials.

Motion devices in DED systems can be employed in various ways, including the movement of the processing head, the movement of the substrate or component, or a combination of both, where motion involves both the processing head and the substrate [30-31]. The most common ones are 3-axis systems. Nevertheless, there are also 4-axis and 5-axis systems that incorporate robotic arms and rotary tables. These advanced systems provide greater flexibility in terms of component geometry. By utilizing multi-axis printing motions, the printing process can be performed in non-vertical directions, enabling the fabrication of more complex geometries [32].

An alternative technique in DED involves the introduction of a metal wire from a spool directly into the focal point of an electron beam, as depicted in Figure 2.6 [30]. The electron beam exerts continuous energy onto the wire, causing it to melt within the beam's focal point. Simultaneously, the base plate moves underneath the beam and wire feed, allowing the part to be built up according to the instructions provided by the CAD file. This approach offers a distinct method for fabricating components in the DED process, utilizing the precise control of the electron beam and wire feed to achieve the desired results. The presence of a vacuum chamber is essential in this DED process to ensure that gases do not interfere or react with the electron beam. By maintaining a controlled vacuum environment, the electron beam can operate with maximum efficiency. Unlike the Powder-Fed DED process, which experiences material losses ranging from 20-60%, the Wire-Fed DED process exhibits no direct metal loss. This characteristic translates into an exceptionally high feedstock efficiency, approaching nearly 100%. However, due to the nature of these process involving weld metal build-up, the surface finish tends to be rough. Achieving the desired dimensions and surface finish often requires post-process machining to refine the entire surface [30,31].

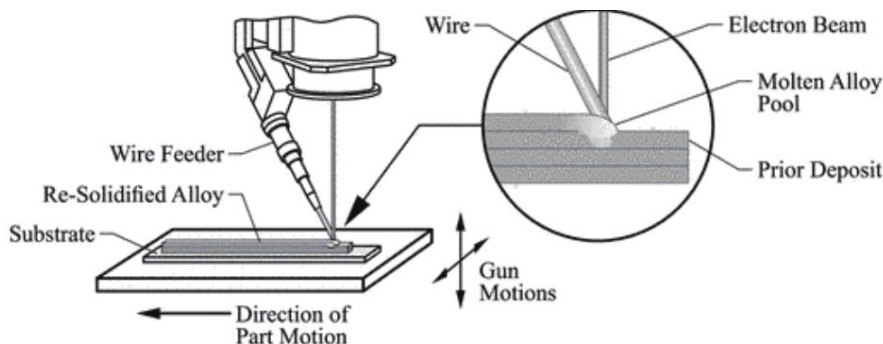


Figure 2.6 - Scheme of the wire-fed DED process [30]

2.3.2 Process Applications

The application of the DED process can be categorized into three main areas. Selective material addition on wrought product forms: This involves adding material to wrought product forms, like plates, flanges, ribs, and pipes, to create distinct

features. Dimension restoration and thick coating application: DED is employed to restore dimensions on worn or damaged components by selectively adding material to specific areas. This way, it is possible to reduce repairing time and extend lifespan. Additionally, it is used to apply relatively thick coatings on new components, imparting improved characteristics such as wear and corrosion resistance. These applications are highly effective as they limit material deposition to selected regions, leading to less waste. Production of near-net shapes: DED is used to fabricate near-net shapes, which are usually further machined to create components and structures [33].

2.3.3 Printing Parameters

The upcoming chapter will delve into the parameters that can impact the efficiency of DED process. The major influencers in these are the laser power, powder feed rate, and scanning speed.

2.3.3.1 Laser Power

Laser power refers to the quantity of heat energy emitted by the laser, which is utilized in the material processing, and it is measured in Watts [W] [34]. Controlling laser power is crucial throughout the entire process as it has the most significant influence on the physical, such as surface finishing, and microstructural properties of the printed part. Maintaining an appropriate laser power is crucial. Excessive laser power can lead to undesired effects such as high dilution, material vaporization, and plasma formation, which are not desirable in the deposition process. Conversely, too low laser power can result in inadequate melting of the deposited material, leading to porosity issues such as lack of fusion [34]. It is therefore of utmost importance to determine the optimal laser power in conjunction with other processing parameters for the specific material processing requirements.

2.3.3.2 Laser Spot Size

The laser spot size in laser metal deposition refers to the size of the laser beam at a specific focal distance, typically measured in millimetres. This parameter significantly affects the energy density during the process, as explained in sub-chapter 2.3.3.6. It follows an inverse relationship with the laser energy density: a larger laser spot size results in a lower energy density, while a smaller spot size leads to a higher energy density. In simpler terms, when the laser spot size is large, the energy delivered to the material is relatively low because the same amount of energy is spread over a larger area. While a larger spot diameter can enhance productivity, it may compromise the dimensional tolerances of the final part [34].

2.3.3.3 Scanning Speed

The scanning speed, typically measured in mm/s, represents the velocity of the printing head, comprising the laser and the nozzle. This parameter directly influences the injection of material into the melt pool and the energy density by determining the duration of the printing head's presence at a specific point. Furthermore, laser power and scanning speed are interconnected. Increasing the laser power enables higher scanning speeds, facilitating efficient powder melting

and resulting in thicker material deposition. However, if the scanning speed is set too high, it results in a decrease in energy density. This lower energy density can lead to undesirable outcomes such as lack of fusion, porosity, and the presence of unmelted powders in the deposited material [34, 35].

2.3.3.4 Powder Feed Rate

The powder feed rate refers to the quantity of feedstock, powder, that is introduced into the melt pool within a specific time frame. This rate is typically measured in grams per minute (g/min). Furthermore, it will also have an impact on the layer height and microstructure [33, 34]. As the previous parameters, it is important to correctly control powder feed rate to have a final product with quality. Powder feed rates too high can lead to non-melted powder, therefore leading to feedstock's waste and poor quality of the final part. In the other hand, when too low, it can result in defects like keyholes and in reduction of buildings efficiency [33].

2.3.3.4 Printing Strategy

By selecting appropriate scanning patterns, it is possible to minimize the generation of residual stresses and thermal distortion during the manufacturing processes [33]. Generally, there are four commonly used deposition patterns in AM: zigzag (bi-directional), raster, offset and fractal in AM. Figure 2.7 provides schemes of each printing strategy.

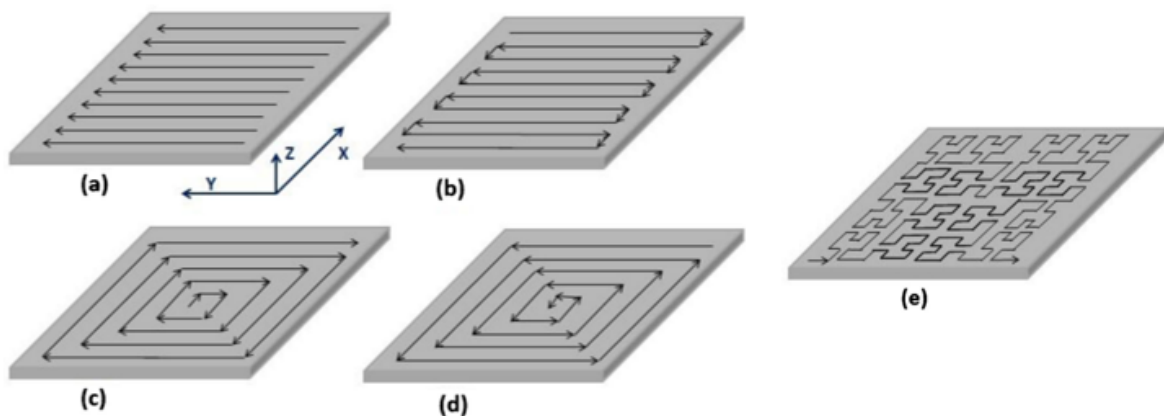


Figure 2.7 - Printing strategies for DED [33]

The raster pattern is widely favoured due to its ease of implementation and versatility, as it can be applied to any type of part regardless of its shape. Conversely, the fractal and offset patterns pose challenges when dealing with complex geometries; however, they offer the potential to achieve high levels of geometric accuracy [33].

2.3.3.5 Hatch Spacing

Hatch Spacing refers to the distance between the centres of two consecutive printed tracks or lines. It plays a significant role in determining the level of overlapping between tracks and the resulting quality of the printed part. When the hatch spacing is smaller than the sum of half the width of the tracks, it indicates overlapping between adjacent tracks. Overlap percentage represents the

percentage of a preceding deposition track covered by an adjacent track. In general, a lower hatch spacing leads to a higher degree of overlapping between tracks. On the other hand, high hatch spacing can lead to the formation of inter-track pores due to larger gaps between tracks [34,35]. To visualize this concept, Figure 2.8 illustrates the hatch spacing and overlapping concepts.

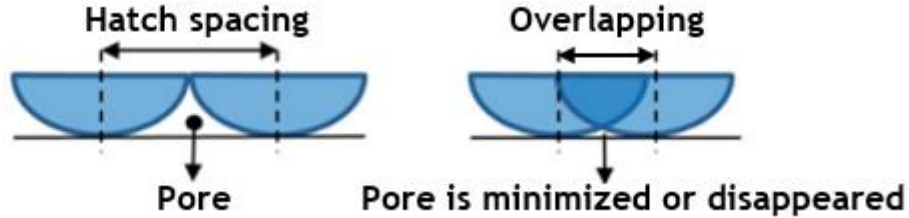


Figure 2.8 - Hatch spacing and overlapping between two printed lines. Adapted from [35]

This way, finding the right balance between hatch spacing and overlapping is important to ensure proper fusion between tracks, minimize defects, and maintain structural integrity during additive manufacturing process.

2.3.3.6 Comparison Parameters

The optimization of parameters for DED in AM is an iterative process influenced by various factors. Due to this complexity, parameter selection relies on comparing the properties of multiple printed samples to identify the optimal combination for a specific deposited material and substrate. To simplify this parametrization process, researchers have developed formulas that can predict the behaviour of the DED process and facilitate the comparison of printing results. These formulas establish relationships between two or more process parameters, enabling a more systematic approach to parameter optimization.

Equation 2.1 establishes a connection between the laser power (P), scanning speed (SS), and laser spot size (ϕ), defining the global energy density [36]:

$$\text{Global Energy Density} \left[\frac{J}{mm^2} \right] = \frac{P [W]}{SS \left[\frac{mm}{s} \right] \cdot \phi [mm]} \quad (2.1)$$

Equation 2.2 introduces the concept of volumetric energy density by incorporating not only the laser power (P), scanning speed (SS), and laser spot size (ϕ), but also the width (w) and height (h) of the deposition track [37]:

$$\text{Volumetric Energy Density} \left[\frac{J}{mm^3} \right] = \frac{P [W]}{SS \left[\frac{mm}{s} \right] \cdot h [mm] \cdot w [mm]} \quad (2.2)$$

Equation 2.3, known as the speed per feed, establishes a relationship between the scanning speed (SS) and the powder feed rate (FR). It quantifies the distance covered by the printing head to deposit 1 gram of powder [38]:

$$\text{Speed per feed} \left[\frac{mm}{g} \right] = \frac{SS \left[\frac{mm}{min} \right]}{FR \left[\frac{g}{min} \right]} \quad (2.3)$$

Equation 2.4, known as the volumetric energy density, establishes a

connection between the powder feed rate (FR), scanning speed (SS), and laser spot size (φ). It quantifies the amount of powder distributed per each square millimetre during the printing process [38]:

$$\text{Powder Deposition Density} \left[\frac{g}{mm^2} \right] = \frac{FR \left[\frac{g}{min} \right]}{SS \left[\frac{mm}{min} \right] \cdot \varphi [mm]} \quad (2.4)$$

By utilizing these formulas, manufacturers and researchers can streamline the parametrization process, reducing the need for extensive trial and error. These predictive models provide valuable insights and guidance in determining the most effective parameter combinations, enhancing the efficiency and quality of DED-based additive manufacturing.

2.3.4 Component Analysis

Understanding the efficiency and accuracy of an AM process relies on the analysis of the produced components. This chapter provides an overview of the key aspects associated with components manufactured through fused-based AM processes, with a particular focus on components built using DED techniques.

2.3.4.1 Bead Geometry

During the AM process, when the powder and substrate melt, they combine to form a melt pool accompanied by Marangoni convection forces. This phenomenon occurs due to variations in surface tension within the melt pool, leading to internal movements of the molten material. The Marangoni Effect is characterized by lower surface tension values at the centre of the melt pool and higher tension values at the solid-liquid frontier. These tension discrepancies result in radial motions and material transport within the printed material. Consequently, the Marangoni Effect plays a role in determining the dimensions of the melt pool [39].

Understanding the geometry of the melt pool is crucial for analysing the efficiency of the AM process. Figure 2.9 illustrates a schematic representation of the cross-section of a single printed track. Within this geometry, several dimensions play a significant role, including the depth (d) of the melt pool, the height (h) of the bead head, the width (w) of the substrate-track interface, and the wetting angle (θ). These dimensions are key in assessing the characteristics of the printed bead.

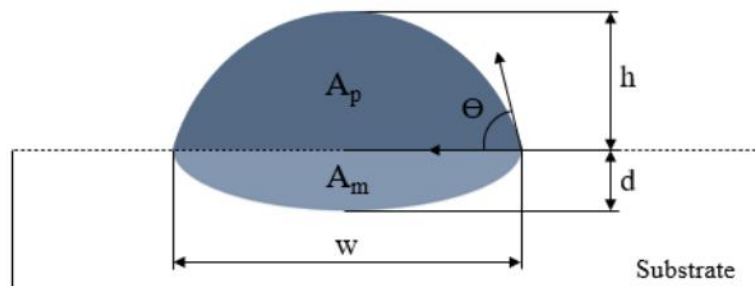


Figure 2.9 - Cross section of a single layer deposition and geometrical properties: d - depth, h - height, w - width, θ - wet angle, A_p - printed area and A_m - melted area. Adapted from [40]

Dilution

The dilution proportion refers to the percentage of the printed material that undergoes melting. To establish a strong metallurgical bond between the substrate and the cladding, a dilution ratio ranging from 15% to 30% is recommended. It is important to avoid excessive dilution as this can lead to reduced deposition yield and significant alterations in the chemical composition of the printed material [38]. Two methods can be used to calculate the dilution proportion. The first method involves calculating the ratio between the depth of the melt pool (d) and the total height ($d + h$), as given by Equation 2.5. The second method compares the ratio between the area of the melt pool (A_m) and the combined area of the printed and melted regions ($A_p + A_m$), as given by Equation 2.6. While both equations provide a means of comparing printings, the method that compares the ratio of areas (Equation 2.6) is more accurate when dealing with asymmetrical tracks [40].

$$D = \frac{d}{h + d} \quad (2.5)$$

$$D = \frac{A_m}{A_m + A_p} \quad (2.6)$$

Shape of the melt pool

The amount of substrate material, A_m , melted during the process is crucial for assessing the quality of the printed layer. Melting the substrate material facilitates a strong metallurgical bond between the printed layer and the substrate. However, excessive substrate melting results in dilution, which should be minimized to prevent degradation of the mechanical and corrosion properties of the printed layer. Controlling and reducing substrate melting is essential to maintain the desired quality [41]. Figure 2.10 illustrates the common shapes of the melted area, A_m .



Figure 2.10- Typical shapes of the melted area. Adapted from [42]

Ideally, the geometry of the melted area should exhibit a uniform and shallow profile, as depicted in Figure 2.10 a). However, achieving this desired shape in practice poses a challenge, as it requires careful selection and optimization of the printing parameters. Figure 2.10 b) depicts excessive burn-in of the substrate, while Figure 2.10 c) shows double-burn-in shape due to high scanning speed accompanied with high power level. Finally, Figure 2.10 d) represents an asymmetrical burn-in shape that can be attributed to the powder being fed from the right side, perpendicular to the direction of cladding.

The Gaussian beam is the preferred energy distribution for laser cladding with powder injection, as it promotes improved homogeneity in microstructure, reduced dilution, and higher bead quality [41]. Figure 2.11 illustrates the Gaussian distribution of laser energy and powder particles when using a lateral nozzle. Notably, when the powder particles are introduced in a Gaussian distribution, the majority of the powder is directed towards the center of the deposition line. Therefore, the orientation of both the powder jet and the laser beam significantly impact the heat flux [41].

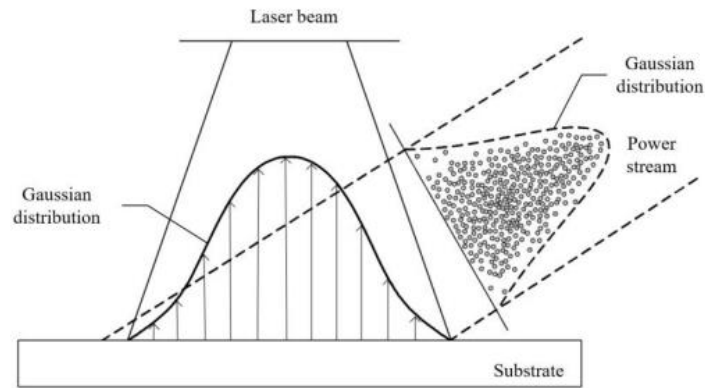


Figure 2.11- Gaussian distribution for the laser energy and for the particles for a lateral nozzle. Adapted from [43]

Wetting Angle

The wetting angle serves as a significant parameter that provides insights into the quality of the printed track. It directly correlates with the interfacial energies encompassing the liquid-vapor (γ_{LV}), solid-vapor (γ_{SV}), and solid-liquid (γ_{SL}) interfaces, as depicted in Figure 2.12.

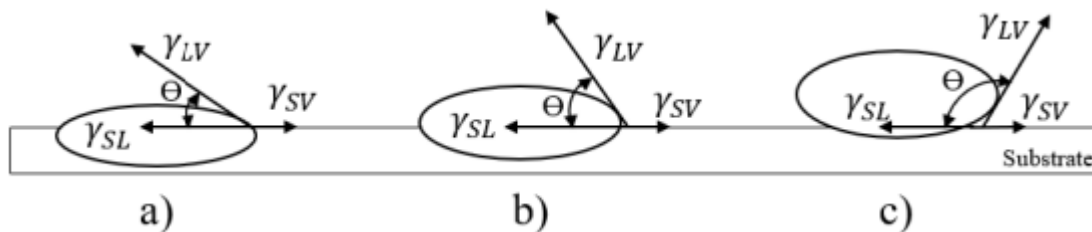


Figure 2.12- Wetting angle variation with interfacial energies. Adapted from [43]

The relationship between these energies can be expressed as:

$$\gamma_{SV} - \gamma_{SL} = \gamma_{LV} \cdot \cos(\theta) \quad (2.7)$$

Figure 2.12 b) illustrates an ideal bead formation. A higher laser energy results in increased dilution, leading to a wetting angle like the one shown in Figure 2.12 a). Conversely, oxidation is the primary cause of a wetting angle like the one depicted in Figure 2.12 c). An oxidized substrate exhibits reduced wettability by molten metal, along with lower surface energies [43].

2.4 Tool Steel Printing through DED

To gather insights into the commonly utilized parameters and substrate materials for DED of tool steels, a comprehensive literature review of several articles was conducted. These studies encompassed an analysis of various aspects such as bead geometry, dilution proportion, porosity, microstructure, and hardness. Specifically, the emphasis was placed on investigating the impact of deposition parameters on dilution proportion, bead geometry, and wetting angles. Appendix B provides a detailed list of all the articles that were reviewed for this study.

Wolosz et al. [44] deposited AISI H13 hot work tool steel powder with a particle size range of 44-150 μm on a X37CrMoV5-1 steel rod. The study focused on examining the effects of various technological parameters, such as laser spot diameter, powder flow rate, and deposition velocity, on the efficiency of cladding, clad geometry, and properties of the deposited material. They considered laser spot diameters of 1.63, 1.76 and 1.85 mm; powder flow rates of 4.76 and 5.89 g/min and deposition velocity of 2, 4, 6, 8, 10 mm/s. By altering these parameters during the experiments, the researchers investigated their influence on the shape of the clads, size of the heat-affected zone, microstructure, and hardness of the steel. The findings indicate that increasing the scanning velocity and decreasing the mass powder flow rate led to a decrease in the dimensions of the clads.

Pellizzari et al. [45] performed depositions of AISI H13 tool steel on a CuBe alloy substrate considering different parameters. The researchers explored various parameters, including laser power, powder feed rate, overlap ratio, and substrate temperature. The optimization process involved determining the optimal values for these parameters at a scan speed of 1000 mm/min. The quality of the cladding was evaluated based on several criteria, namely: geometrical features, presence of cladding defects, interfacial adhesion, and substrate over-aging. Through the experimentation, it was found that relatively high laser power and intermediate powder feed rate resulted in high-quality cladding tracks while maximizing energy and powder efficiency simultaneously. The recommended parameter ranges identified in this study were a laser power of 1800-2200 W and a powder feed rate of 8-12 g/m at a scan speed of 1000 mm/min.

Arrizubieta et al. [46] analysed printings of AISI H13 steel on wrought H13. By fixing the powder feeding rate at 0.057 g/s, a scanning speed of 14.17 mm/s and the laser beam diameter by 0.50 mm, the researchers varied the energy input from 37.81 to 88.21 J/mm². The researchers conclude that increasing energy input during the process led to a slight decrease in hardness, attributed to the increased height of deposited layers, larger secondary dendrite arm spacing, and reduced cooling rate because of greater deposited metal volume, suggesting that the variation in secondary dendrite arm spacing contributed partially to the observed hardness decrease.

Materials and Methods

3.1 Materials

3.1.1 AISI P20+Ni Tool Steel

AISI P20+Ni is a medium carbon low alloy tool steel that belongs to the family of mold steels [47]. For this study, metal chips of AISI P20+Ni were provided from a metalworking industry, to produce power feedstock for DED depositions. Table 3.1 shows the chemical composition of AISI P20+Ni [47], and the chemical composition of the obtained metal chips analysed via SEM/EDS analysis, where carbon and sulphur contents were corrected through adequate analysis.

Table 3.1- Chemical composition (wt. %) of the AISI P20+Ni steel [47]

Element	C	Mn	P	S	Si	Cr	Mo	Ni	Fe
AISI P20+Ni [48]	0.35-0.45	1.30-1.60	0.03	0.03	0.20-0.40	1.80-2.10	0.15-0.25	0.90-1.20	Rem.
AISI P20+Ni metal chips *	0.51	1.73	-	<0.0055	0.77	2.11	0.38	0.79	Rem.

* Chemical compositions corrected considering carbon-sulphur analysis made at CINFU (Centro de Formação Profissional da Indústria de Fundição).

The addition of chromium provides enhanced hardness and corrosion resistance, molybdenum contributes to improved strength and toughness. Nickel, at the same time is a key element that significantly enhances the toughness and impact resistance of the steel while improving hardenability [48]. AISI P20+Ni steel is also known for its wear resistance and good polishing performance [47]. This makes it an exceptionally versatile and extensively employed material for manufacturing industry, particularly in the production of plastic injection mold cavities and tooling and die casting components [47,48]. Table 3.2 shows some of the mechanical, thermal, and physical properties of this steel.

Table 3.2- AISI P20+Ni steel properties [47,48]

	Property	AISI P20+Ni
Mechanical Properties	Hardness	336-544 [HV]
	Yield Strength	770-980 [MPa]
	Tensile Strength	850-1100 [MPa]
Thermal Properties	Melting Point	1400-1450 [°C]
	Thermal Conductivity	29-31 [W/m. K]
	Thermal Expansion Coefficient	12.6-14.3 [µstrain/°C]
Physical Properties	Density	7700-7800 [kg/m ³]

3.1.2 AISI 4140 - 42CrMo4 Steel

The substrate used for the current study was a 42CrMo4 steel. This alloy is also known as AISI 4140, and its chemical composition is shown in Table 3.3 [49].

Table 3.3- Chemical composition (wt. %) of the AISI 4140 [49]

Element	C	Cr	Mn	Si	Mo	S	P	Fe
AISI 4140 [49]	0.38-0.43	0.80-1.10	0.75-1.00	0.15-0.30	0.15-0.25	0.040	0.035	Rem.
Substrate AISI 4140 **	0.45	1.17	0.79	0.27	0.19	0.01	0.02	Rem.

* This analysis was performed by Optical Emission Spectrometry with SpectroMAXx equipment.

The AISI 4140 steel is known for its good machinability, high mechanical strength and toughness and excellent fatigue and impact resistance. This steel finds extensive application in components such as gears, automotive parts, drilling joints for deep wells, and wind generators. Table 3.4 shows some of the mechanical, thermal, and physical properties of this steel [49]. For the current study, the substrate was not preheated for printing.

Table 3.4 - AISI 4140 steel properties [49]

	Property	AISI 4140
Mechanical Properties	Hardness	207 [HV]
	Yield Strength	415 [MPa]
	Tensile Strength	655 [MPa]
	Young's Modulus	190-210 [Gpa]
Thermal Properties	Thermal Conductivity	42.6 [W/m. K]
	Thermal Expansion Coefficient	12.2 [μ strain/ $^{\circ}$ C]
Physical Properties	Density	7850 [kg/m ³]

3.2 Powder Production

This sub-chapter outlines the actions taken in the initial practical phase of this study. Firstly, the disc milling (DM) technique was used to produce powder particles for application in the DED technology. Conversely, powder particles via planetary ball milling (PBM) were produced to study the applicability of these in Selective Laser Melting (SLM) technologies. Subsequently, the powder particles were characterized, and various properties, including flowability, density, and hardness, were measured. Disc Milling was used since previous studies [50] showed it has a high production efficiency, that helps to produce enough powder feedstock in a limited time. The application of PBM is more promising for the production of rounded particles.

3.2.1 Metal chips

Metal chips of AISI P20+Ni steel were supplied by a metalworking industry to the production of powder feedstock for the AM technologies. These metal chips are shown in Figure 3.1.

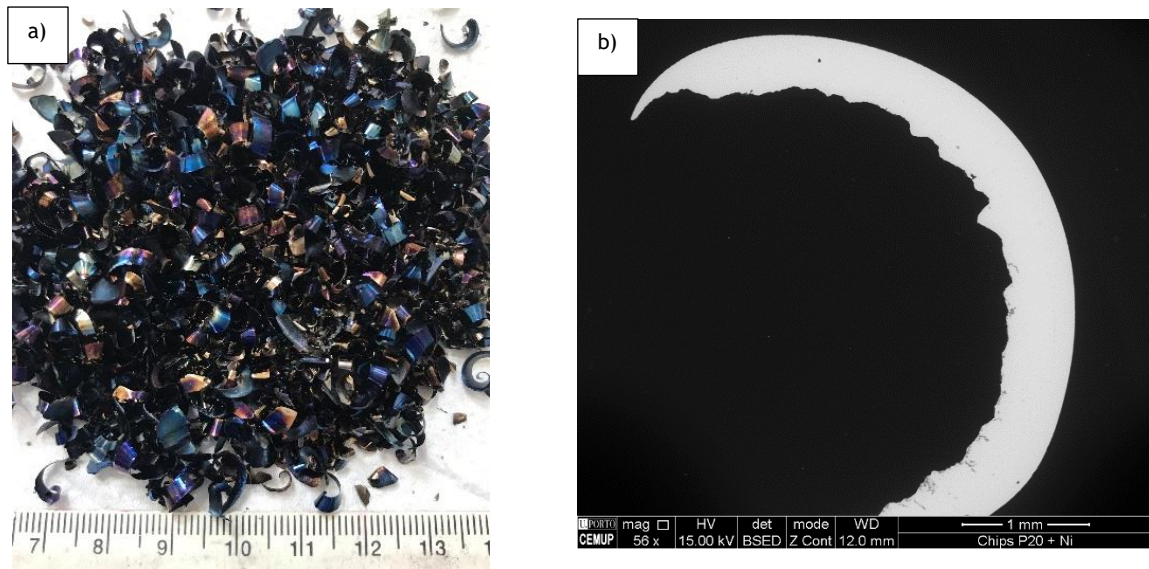


Figure 3.1- a) AISI P20+Ni Metal Chips supplied by metalworking industry. b) SEM image of metal chip used for SEM-EDS and microhardness measurements.

Since there were no machining lubricants or any form of contaminations present, there was no requirement for washing or drying the metal chips.

3.2.1.1 Powder Production for DED

The RETSCH's Vibratory Disc Mill RS 1, with a drive power of 400/700 W, was utilized as the milling equipment to produce powder for DED technology. The machine consistently operated at its maximum rotation speed, which was maintained at 1407 ± 3 rpm. The grinding bodies consist of AISI 420 martensitic stainless steel, with a jar of 250 mL volume. Prior to introducing the material, all grinding components were meticulously cleaned with ethanol and thoroughly dried to prevent any contamination. The guidelines outlined in sub-chapter 2.2.1.1 were followed when positioning the chips and grinding bodies to ensure optimal outcomes. To avoid overheating of the equipment, a noncontinuous milling procedure was implemented. The milling process was limited to a continuous operation of 5 minutes, followed by a mandatory 10-minute pause. Furthermore, after every 30 minutes of milling, a 30-minute break was incorporated for the safety of the machine. This intermittent approach aimed to maintain optimal conditions during the milling process and mitigate potential issues related to temperature and material oxidation.

To determine the milling procedure with maximum productivity for DED's feedstock, powders with size range of 38 and 212 μm were sieved and weighed. For the current study, three disc milling conditions were tested as shown in Figure 3.2.

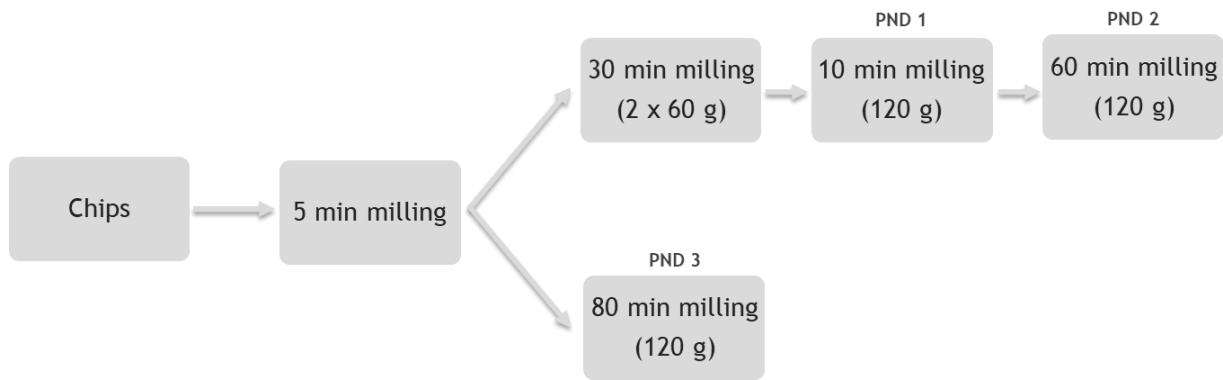


Figure 3.2- Milling conditions carried out in the current study using disc type.

As seen in Figure 3.1, primary chips were curvy-like, therefore, an initial milling of 5 minutes was performed to flatten them. The milling of procedure number 1 for disc milling (PND 1) was performed with two separate batches of 60 grams, each for 30 minutes. Subsequently, both batches were combined, resulting in a total of 120 grams, and they were milled again for 10 minutes. Procedure number 2 for disc milling (PND 2) is a continuation of PND 1, the final batch of 120 grams was milled further for another 60 minutes. Procedure number 3 for disc milling (PND 3) consists in 80 minutes milling of a single batch of 120 grams. Castanheira [51] conducted a study on the production of sustainable powders from stainless steels for DED. The PND 1 is similar to the optimized procedure developed by Castanheira [51].

3.2.1.2 Powder Production for SLM

The Planetary Ball Mill Retsch PM 100 was utilized as the milling equipment to produce powder feedstock for SLM technology. With its single grinding station and easy-to-use counterweight capable of compensating masses up to 8 kg, the Planetary Ball Mill PM 100 stands out as a high-powered benchtop model. It offers the ability to grind up to 220 mL of sample material per batch and reach maximum speed rotation of 650 rpm. A 500 mL stainless-steel jar with its protective jacket of the same material was used. Regarding to the balls used for this process, diameter sizes of 5 mm and 30 mm were used. Note that all the grinding components were cleaned and properly dried before introducing the material.

To identify the most productive milling procedure for the feedstock of SLM, powders with high range in size distribution from 20 to 53 μm , five milling conditions were tested. This specific size interval aligns most effectively with the powder dimension prerequisites pertinent to SLM printing. Prior to planetary ball milling production, the metal chips were submitted to a 5-minute milling in the disc milling equipment to flatten them. The milling parameters are shown in Table 3.5. For each condition the direction reversal was on, which means the rotational direction changed for every cycle of milling/break time.

Table 3.5 - Planetary Ball Milling Procedures (PNB)

Procedure Number (PNB)	Material Weight [g]	Ball Diam. [mm]	Ball Weight [g]	BPR	Op. Time [hr:min]	Milling-Break Time [min-min]	Total Util Milling Time [min]	Rotation Speed [RPM]
PNB 1		30			01:05	1-9	72	600
					04:20	1-3		450
PNB 2		30			01:05	1-9	150	600
		5			04:20	1-3		450
PNB 3	120	30	878	7.3:1	01:05	1-9	228	600
		5			04:20	1-3		450
PNB 4		30			03:15	2-3	306	600
		5			04:20	1-3		450
PNB 5		30			03:15	2-3	150	600
		5			01:05	1-9		450
								600

3.2.1.3 Powder Characterization

After the milling process, the powder particles were sieved to, in a first phase, understand the productivity of each milling procedure. After that, a particle size range of the powder particles were selected to be characterized by the following techniques.

3.2.1.3.1 Sieving of the Particles

The sieving of the powder particles was carried out using two different methods, considering ASTM B214 standard [52]. The first method involved the use of three standard sieves from Retsch with apertures of 212 μm and 38 μm . The second method employed four standard sieves from Retsch with apertures of 212 μm , 150 μm , 53 μm , and 20 μm . Both methods provided insights into the productivity of the powder particles for each milling procedure. However, the first method specifically allowed for the selection of powder particles within the size range of 38 μm to 212 μm , which is suitable for DED process. The second method facilitated obtaining powder particles within the size range of 20 μm to 53 μm , suitable for SLM technologies.

Prior to their utilization, the sieves underwent a thorough cleansing process. They were immersed in an ultrasonication bath containing water and detergent for approximately 5 minutes. Subsequently, the sieves were carefully dried using compressed air at a very low-pressure setting followed by hair drier. Regarding to the method of sieving, the powder particles were sieved with a vibratory machine for 10 minutes at an amplitude of 80, followed by a 10-minute break.

3.2.1.3.2 Particle Size Distribution

SEM analysis provided valuable insights into the shape and particle size, and the distribution of particle sizes of the powders. Moreover, can be analysed using image analysis technique. The software Image J was used. For this, multiple images were measured to ensure accurate results, note that any particle seen inclined in the images or those with inaccurate dimensions were excluded from the analysis.

3.2.1.3.3 Loose Density

For the determination of loose density, the ASTM B212 standard was followed, utilizing specific equipment and procedures [25]. The setup involved a funnel with a 30° angle and an orifice of approximately 2.5 mm. Additionally, a cylindrical cup with a capacity of 25 cm³ was used. The funnel was used to load the powder, allowing it to flow into the cup through the orifice. As the powder filled and exceeded the cup's capacity, a nonmagnetic spatula was utilized to level off the powder with the cup's top surface. The weight of the powder was measured, and for the calculation of the loose density, Equation 3.1 was used:

$$\text{Loose Density} \left[\frac{g}{cm^3} \right] = \frac{M [g]}{V [cm^3]} \quad (3.1)$$

where M represents the mass of the powder in the cup at the end of the procedure, and V corresponds to the volume of the cup (25 cm³). This calculation was performed three times for PND 1 from disc milling for powder range sizes of 38 and 212 μm, and for the 53 and 150 μm distribution as well. The latter distribution is a commercially recommended size for DED.

3.2.1.3.4 Tap Density

The determination of tap density followed the ASTM B527 standard [27]. The equipment utilized consisted of a funnel, a graduated glass cylinder with a capacity of 100 cm³ and a stand to support the funnel. A precise amount of 100 ± 0.5 g of powder was carefully measured and poured into the graduated cylinder by passing it through the funnel's orifice. Subsequently, the cylinder was tapped exactly 250 times in 1 minute. The powder was then examined to confirm that it was levelled, and the volume was recorded. The tap density was calculated using Equation 3.2:

$$\text{Tap Density} \left[\frac{g}{cm^3} \right] = \frac{M [g]}{V [cm^3]} \quad (3.2)$$

where mass of the powder is denoted as M , and the final volume of the tapped powder is represented as V . This procedure was repeated three times for PND 1 from disc milling for powder range sizes of 38 and 212 μm, and for the 53 and 150 μm.

3.2.1.3.5 Flowability Measurements

The flowability of the powder was assessed considering the ASTM B213 standard [21]. Before conducting the tests, the powders were subjected to a drying process at 100°C for 1 hour. The equipment setup involved a funnel, the same as the one utilized for measuring loose density, a graduated glass cylinder, and a stand. To begin the test, a precise mass of 50 grams was measured. The discharge orifice of

the funnel was manually blocked using a dry finger, and the powder was poured into the funnel without any vibration, tapping, or equipment movement. Once all the powder was inside the funnel, the finger was removed from the orifice, and simultaneously, the stopwatch was started. The stopwatch was stopped the moment all the powder completely passed through the orifice of the funnel. The elapsed time was recorded. This procedure was repeated three times using fresh powder for PN1 from disc milling technique for powder range sizes of 38 and 212 μm , and 53 and 150 μm .

3.3 Printing through Direct Energy Deposition

To ensure a systematic approach in the DED printing process, a thorough literature review was conducted to gather insights into the parameters employed in DED printings of AISI H13 since INEGI has some background on this powder [54]. This review aimed to establish a baseline for process parametrization. For each combination of parameters (laser power, powder feed rate, scanning speed), single line printings were performed and evaluated. Through careful visual analysis of the lines' top and cross-sectional views, the line exhibiting adhesion, least defects, and optimal linearity was chosen to proceed with printing planes using the same parameters. For plane parameters, overlapping can be optimized taking into consideration the overall geometry. This way, after determining the optimized parameters, the construction of a multilayered volume was initiated. Notably, the layer thickness played a crucial role in that construction, as optimizing this parameter was vital to prevent the occurrence of porosities between layers.

3.3.1 Selection of Printing Parameters

For the selection of the printing parameters, the state of art was considered - Appendix B. Although the feedstock material for this project is AISI P20+Ni tool steel, limited information was available on this specific steel. This way, AISI H13 tool steel was considered since it is one of the most studied tool steels. Therefore, three articles were selected that extensively analysed the clad geometry, dilution proportion, and wetting angles, which were the key criteria for parameter selection. The optimal parameter combinations from each article, based on the defined criteria, are listed in Appendix C.

Note that before proceeding with the actual printings, it was necessary to do the linearization of the material, to determine the maximum achievable powder feed rate that in this case was 20.48 g/min.

Thus, taking into consideration the literature analysis and the linearization, parameters for the depositions of AISI P20+Ni steel were select and are presented in Table 3.6. Conversely, the fixed parameters for the DED printings are listed in Table 3.7.

Table 3.6- Parameters for the AISI P20+Ni printings

Variable Parameters	
Laser Power	500, 900, 1800 W
Scanning Speed	120, 360, 450, 480, 852 mm/min
Powder Feed Rate	3, 4, 6, 8 g/min
Shield Gas Flow Rate	5, 20 l/s

Utilizing the parameters outlined in Table 3.6, the Design of Experiments (DOE) Taguchi L9 method was implemented to generate eight distinct combinations of parameters. The parametrization process will be further explained in Chapter 4.2 from Results and Discussion section.

Table 3.7 - Common parameters used for the AISI P20+Ni printings.

Fixed Parameters	
Shield Gas/Carrying Gas	Ar Grade 3
Carrying Gas Flow Rate	4 l/s
Stand-off distance	13 mm
Inclinations Angle	5 °
Laser Spot Size	2.1 mm

3.3.2 DED Setup

The DED equipment employed in the production of the samples for this dissertation is shown in Figure 3.3. The primary element of the equipment comprises the KUKA 6-axis industrial robot, manufactured by KUKA in Augsburg, Germany. In conjunction with this robot, the depositions were performed on a DEMMELER 3D welding table sourced from Memmingen, Germany. The table featured eight electrical resistance heating cells and had the capability to achieve temperatures of up to 600 °C; however, the preheating was not used in this study.

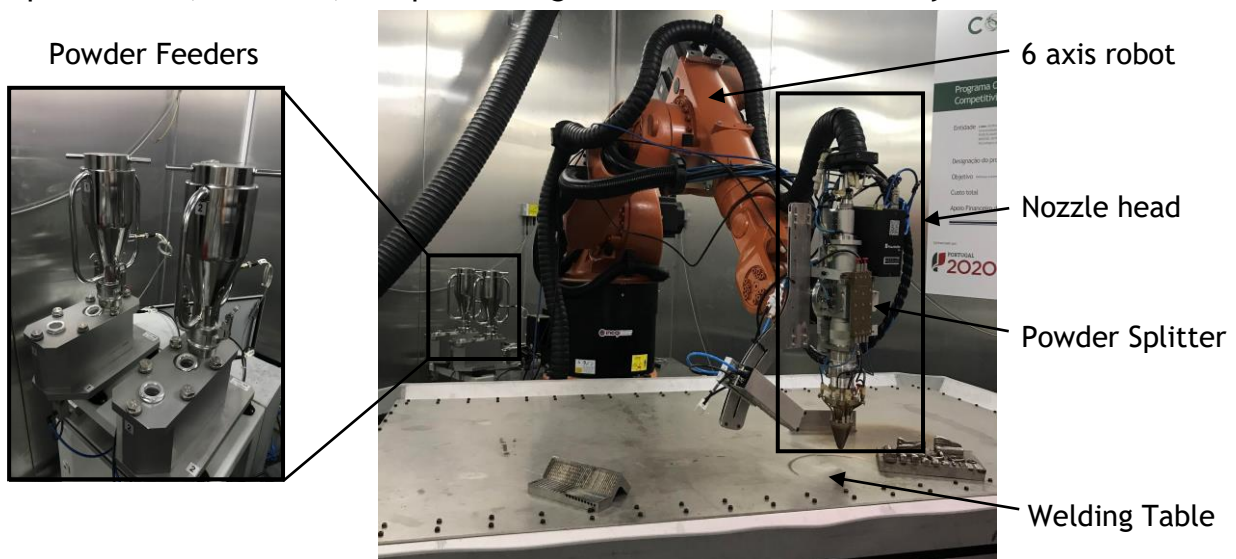


Figure 3.3 - DED equipment used for the printings.

For the deposition process, a COAX12V6 nozzle head manufactured by Fraunhofer IWS in Dresden, Germany, was used. This nozzle head possessed a cooling capacity of 6000 W, ensuring continuous operation. Additionally, it was connected to a Fraunhofer IWS powder splitter, enabling the separation of the powder material into four distinct channels. To supply the necessary powder, the equipment featured two independent Medicoat AG Disk powder feeders from Mägenwil, Switzerland. These feeders operated smoothly within a range of 0.5 g/min to 100 g/min, ensuring a pulsation-free powder flow. Furthermore, the carrying gas could be modified as required. Both the carrying and shielding gases were provided by an inert gas supply

regulated at 6 bar. For the depositions conducted in this project, argon (Ar) Grade 3 was used as the inert gas.

The energy source employed was the coherent highlight FL3000, a fiber laser manufactured by Coherent in Santa Clara, USA. This laser emitted a Gaussian distribution with a wavelength of 1070 ± 10 nm. It operated in continuous wave (CW) mode, providing a maximum power output of 3000 W.

3.4 Characterization

3.4.1 Microstructural Characterization

To study the characteristics of the powder and metal chips and the final microstructure of the printed samples via DED, the samples were submitted to a rigorous metallographic preparation. In the case of the printed samples, this preparation was initiated with a cutting procedure its cross section with aid of the Mecatome T 260 cutting machine. After, all samples were cold mounted with Epoxi Resin to help the following steps. Then, the samples were submitted to polishing with abrasive sandpapers with a sequence of 120, 180, 320, 400, 600, 1000 and 4000 mesh, and finishing with polishing clothes with diamond suspension of 6 and 1 μ m. Nital 2% was used as chemical etching to attach polished surface.

To conduct metallography observations, digital microscope (OM) Leica DVM6 A was utilized, running LAS X version 3.014 software; as well as optical microscope Leica DM4000 M, using Leica Application Suite V4.13. A scanning electron microscope (SEM) (FEI Quanta 400 FEG (ESEM, Hillsboro, OR, USA) equipment, using secondary electron (SE) or backscattered electron (BSE) modes) was utilized to perform comprehensive microscopy analyses, encompassing local, profile, and map chemical analyses. In the other hand, the chemical characterization/elemental analysis of the samples were executed using energy-dispersive X-ray spectroscopy (EDS) (EDAX Genesis X4M, Oxford Instrument, Oxfordshire, UK).

3.4.2 Mechanical characterization

Vickers hardness tests were carried out accordingly to the ISO 6507-1:2018 standard [53]. For metal chips and powder specimens, 10 indentations were made applying 25 gf indentation (HV 0.025), resorting to an indentation time of 15 seconds. For DED manufactured samples, indentation lines with a step of 20 μ m from the topmost region of the deposited area to the end of the HAZ (Heat Affected Zone) reaching the substrate material were made, applying 10 and 100 gf indentation (HV 0.1), resorting to an indentation time of 15 seconds. The equipment used to perform these tests was FALCON 300.

Results and Discussion

In this chapter, comprehensive results of the conducted research are presented, accompanied by a critical discussion of the findings. The first sub-chapter concentrates on the production, characterization, and detailed description of the feedstock powder for DED. Subsequently, the second sub-chapter delves into the production, characterization, and description of the feedstock powder for SLM. Finally, the last sub-chapter focuses on the printings carried out using the DED.

4.1 Powder Production

4.1.1 Chemical Composition

EDS analysis, being a semi-quantitative method, may not accurately detect elements such as C and O. Furthermore, the presence of C in the analysis results can be influenced due to contaminations like the manual handling of the materials. This way, it is recommended to perform a carbon-sulphur analysis to get an accurate chemical composition. Appendix D shows the chemical composition's spectra for the initial metal chips, the powder particles from the PND 1 with particle size range between 38 and 212 μm and powder particles from PNB 5 with size range between 20 and 53 μm . The explanation for the chosen particle size range of the powder produced via DM will be elucidated at the conclusion of subchapter 4.3.2. Conversely, the justification for the choice of particle size range for powder produced via PBM has already been explained in subchapter 3.2.1.2. On the other hand, Table 4.1 presents the chemical compositions obtained via SEM-EDS analysis. For the specific case of the metal chips, the chemical composition was corrected based on the carbon-sulphur analysis conducted at CINFU.

Table 4.1-Semi-quantitative chemical composition (wt. %) of metal chips and powder particles (except C and S)

	C	Si	Mo	Cr	Mn	Ni	S	Fe
Metal Chips	0.51	0.77	0.38	2.11	1.73	0.79	<0.0055	Rem.
Powder Particle PND 1 - Disc Milling	-	0.71	0.83	2.33	1.93	0.91	-	Rem.
Powder Particle PNB 5 - Planetary Ball Milling	-	0.65	0.56	2.14	1.87	0.90	-	Rem.

The chemical analysis enables a comparison of the semi-quantitative and qualitative chemical composition of the material, both before and after the milling process. This comparison provides valuable insights into the impact of the milling process on the material's chemical composition. In this manner, it is feasible to state that the chemical composition of these samples obtained through SEM-EDS analysis have slightly differences when compared to commercial AISI P20+Ni steel because it was made a semi-quantitative analysis. Note that, in EDS analysis, only a specific area is excited by the energy source. Therefore, to obtain more reliable and accurate results, many measurements should be conducted.

4.2 Powder Production for DED

4.2.1 Powder Production and Characterization

4.2.1.1. Efficiency

In accordance with the details provided in Chapter 3.2.1.1, an essential preliminary step was undertaken, involving the submission of a 5-minute milling process to all metal chips, irrespective of their procedure. This milling process resulted in the formation of particles flattened and not curvy, as shown in Figure 4.1.



Figure 4.1 - Particles after 5 minutes of milling.

After that, these metal chips underwent to three different milling procedures shown in Figure 3.2. Figure 4.2 illustrates the weight percentage of milled chips for each procedure resulting from the sieving analysis. With this analysis it is possible to conclude that the productivity of each milling procedure since, in this case, the goal was to obtain the maximum amount of powder particles in the size range of 38 and 212 μm from the metal chips. Note that besides the material loss resulting from milling procedure, there was also some loss subsequent from the sieving procedures.

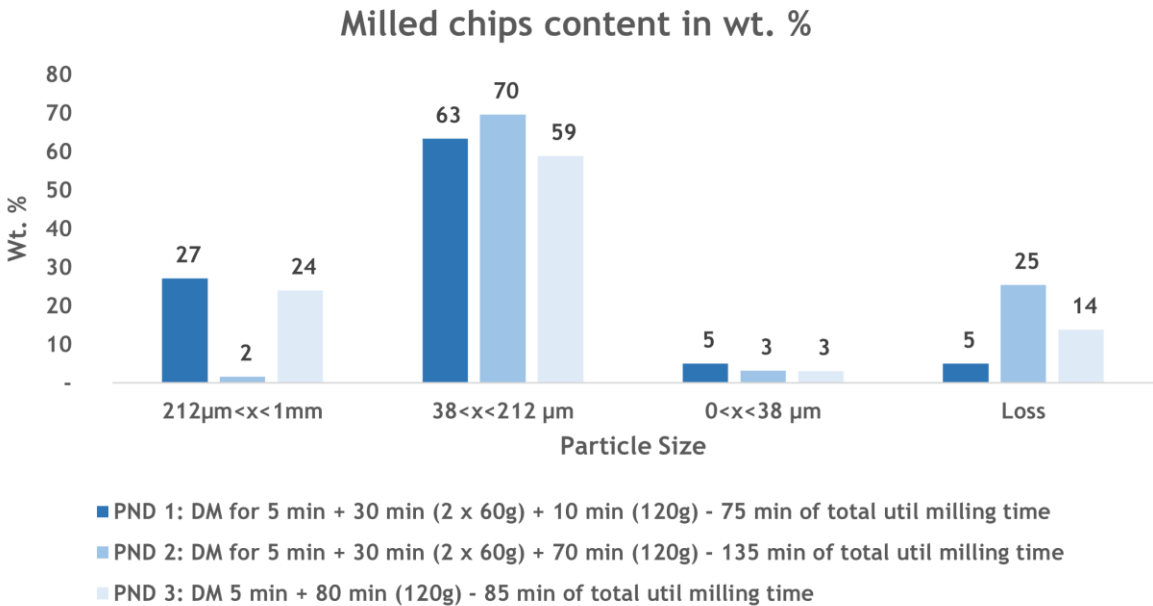


Figure 4.2 - Milled chips content in wt. % for each condition.

As depicted from Figure 4.1, PND 2 seems to have the best productivity, with 70 wt. % content of powder particles with size range between 38 and 212 μm . It is needed 135 min of util milling time to produce a batch of 120 grams with this procedure, however it involves a material loss of 25%. On the other hand, PND 1 only needs 75 minutes of milling time to obtain 63 wt. % content of powder particles with size range between 38 and 212 μm . This means that with about 56% of the milling time of PND 2, PND 1 can almost achieve the productivity of PND 2 for the powder particles range between 38 and 212 μm . Taking this in consideration, it is possible to affirm that PND 1 has a better relation of production efficiency/production time when compared to PND 2.

PND 3 presents itself as a potentially suitable approach for this study. Nevertheless, it is imperative to consider that it encompasses a substantial 59 wt. % of powder particles within the size range of 38 to 212 μm , coupled with a notable material loss of 14%. Furthermore, it should be duly acknowledged that the total optimal milling time for PND 3 exceeds that of PND 1 by a margin of 10 minutes per batch of 120 grams.

This way, considering milling time, productivity to get the highest wt. % content of powder particles with size range of 38 and 212 μm , as well as material loss, PND 1 exhibited an interesting option to proceed with this study. This procedure showcased lower energy consumption, exhibited superior sustainability and economic viability while yielding comparable results. Therefore, PND 1 remains productive as conducted by Castanheira [51].

Henceforth, the milling process persisted under PND 1 until enough powder was obtained for the DED printings. A total of fourteen milling processes were conducted, all following PND 1, resulting in a transformation of 1680 grams (14 x 120 grams) of powder. Nevertheless, the powder production was intentionally scaled up to ensure an ample supply of metallic powder for all deposition processes. After every cycle of this process, a sieving analysis separated the particles into three distinct size ranges: smaller than 38 μm , between 38 μm and 212 μm , and larger than 212 μm .

For DED printings, an estimated 1500 grams of powder were available. Approximately 18 hours of util milling time were required to generate all the powder for the DED printings, accounting for nearly 57 hours when considering break times (a 10-minute pause after every 5 minutes of milling and a 30-minute pause after every 30 minutes of milling). Therefore, on average, it takes approximately 38 hours, including break times, to produce 1 kilogram of powder.

4.2.1.2 Particle Size Distribution

Figure 4.3 illustrates the evaluation of the particle size distribution for PND 1, conducted using Image J software. Simultaneously, Table 4.2 presents the particle size distribution, aspect ratio, and average powder particle size for PND 1, as determined through image analysis.

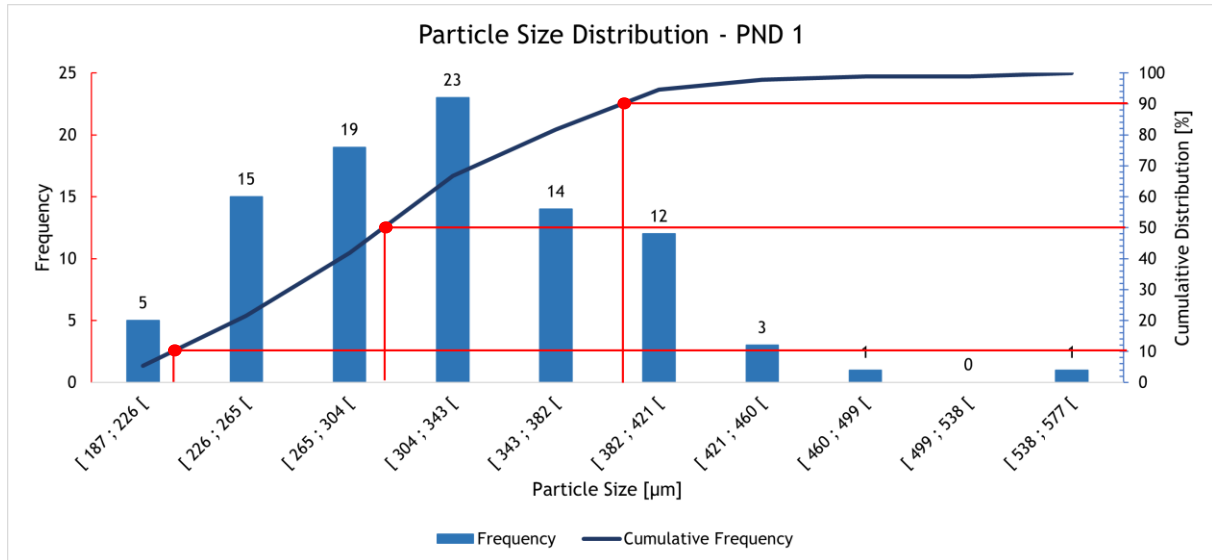


Figure 4.3 - Particle size distribution for PND 1, measured by Image J.

Upon analysing Figure 4.2, a distinct normal distribution of particle sizes can be observed for PND 1. The presence of particles with sizes smaller than 38 μm has been observed in the SEM images, however they were not considered for this analysis. This occurrence can be attributed to particle entrapment or electrostatic forces. Consequently, during the sieving process, certain particles, despite having an average size smaller than 38 μm, remain trapped and do not pass through the apertures. Conversely, particles with a size larger than 212 μm can also be observed, likely due to their highly elongated shape, enabling them to pass vertically or diagonally through the apertures.

Table 4.2 - D_{10} , D_{50} and D_{90} values for PND 1

Procedure	D_{10}	D_{50}	D_{90}	Aspect Ratio	Average powder particle size
PND 1	226 μm	304 μm	382 μm	0.51	321±51 μm

After analysing Table 4.2, it becomes evident that the powder derived from PND 1 contains particles with sizes exceeding the maximum threshold typically considered for DED, which is normally set at 150 μm. Notably, the D_{50} value indicates that 50% of the powder particles possess sizes smaller than 304 μm. Conversely, the average powder particle size is relatively substantial, measuring 321 μm. Additionally, it is noteworthy that the aspect ratio of the powder particles obtained through this procedure deviates significantly from 1. Having an aspect ratio close to 1 would signify particles with a nearly spherical shape, which is considered highly desirable for AM technology.

4.2.1.3 Particle shape

Figure 4.4 presents a SEM image depicting the particles in the size range of 38 μm to 212 μm from PND 1 (75-minute milling time). Notably, these particles exhibit a distinct flake-like shape and irregularity. These characteristics diverge from the conventional rounded or spherical powder shapes commonly used for AM printings, which are typically generated through the gas atomization process. Moreover, the cold-welding phenomenon characterized by the fragmentation and subsequent bonding of smaller particles, facilitated by the substantial pressure exerted between the powder particles during the milling process, can be already detected (Magnification of Figure 4.4). Castanheira [51] achieved powder particles of greater thickness compared to those yielded under the same processing conditions in the current study. This indicates a higher incidence of the cold-welding phenomenon, as anticipated due to the ductile nature of AISI 303 steel.

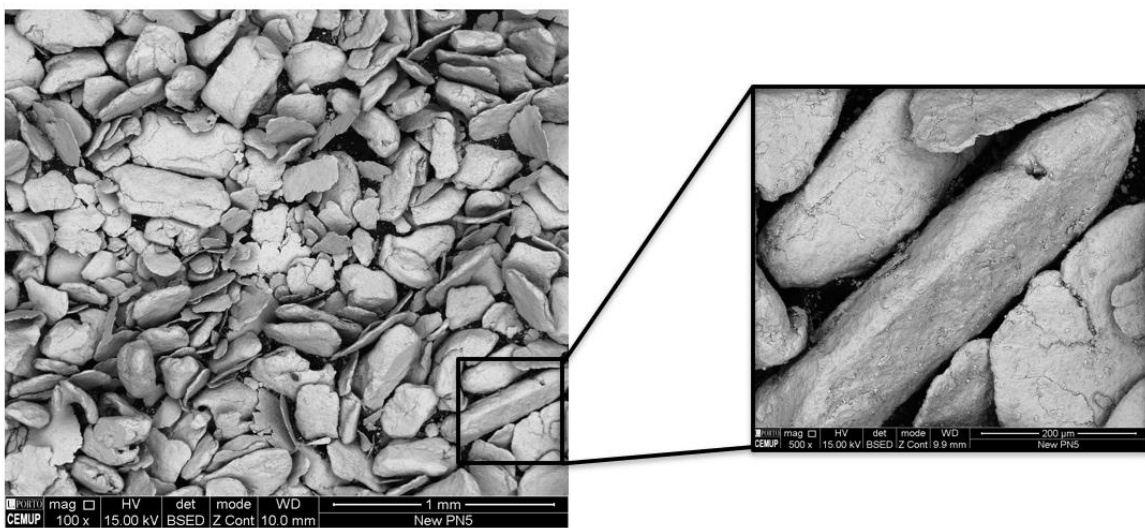


Figure 4.4 - SEM image of particles with a size between 38 μm and 212 μm resultant from PND 1

Figure 4.5 shows an SEM image of polished powder particles in the size range of 38 μm to 212 μm from PND 1 where it is possible to see the internal characteristics of these particles. Fracture process and cold-welding phenomenon is possible to detect. Concurrently, a noticeable absence of seamless cohesion is observed, attributed to the existence of microporosities, (Magnification of Figure 4.5).

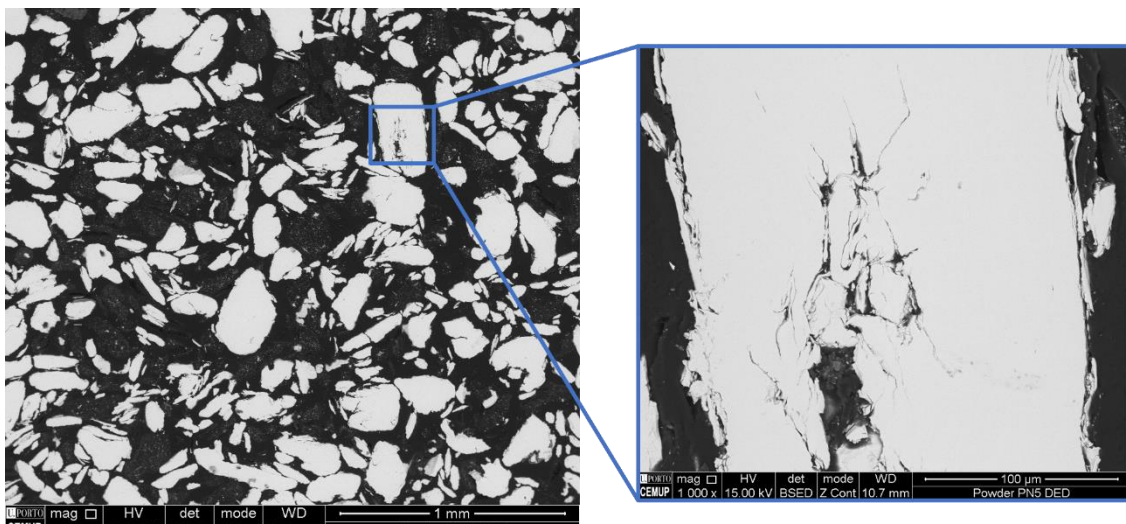


Figure 4.5 - SEM image of polished powder particle in the size range of 38 μm to 212 μm from PND 1

As shown before, PND 2 is a continuation of PND 1 due to the addition of 60 min of util milling time. Like the powder particles from PND 1, powder particles from PND 2 still present a flaky-shape and some irregularity - Figure 4.6. However, a distinctive feature stands out—these particles appear to possess an increased thickness, what is expected with the increase of milling time. Cold-welding is still detected in the powder particles from PND 2, however it was expected to also detect some particles with rounded shapes with the increase of milling time which is not clearly seen.

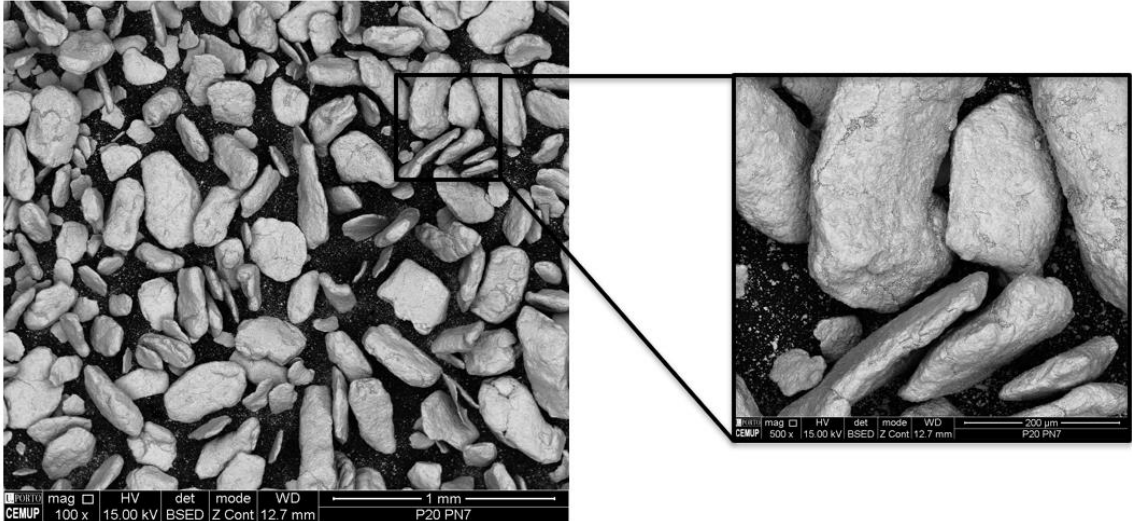


Figure 4.6 - SEM image of particles with a size between 38 μm and 212 μm resultant from PND 2

4.2.2 Density Measurements

The typical size range for metal powders utilized in DED falls between 50 and 150 μm. However, for this study it was decided to use metal powders with a size range between 38 and 212 μm, comparing them to metal powders with size range between 53 and 150 μm to understand powder properties. To assess this, indicators such as loose density, tap density, and flowability tests were evaluated. Note that the selected milling procedure to produce metal powders for this study is PND 1.

4.2.2.1 Loose Density

Table 4.3 depicts those powders with size range between 38 and 212 μm from PND 1 presents a slightly higher loose density when compared to the ones with size range between 53 and 150 μm.

Table 4.3 - Loose density results for PND 1

Sample	PND 1 (53<x<150 μm)	PND 1 (38<x<212μm)
1	2.97 [g/cm ³]	3.35 [g/cm ³]
2	2.94 [g/cm ³]	3.34 [g/cm ³]
3	2.98 [g/cm ³]	3.34 [g/cm ³]
Mean	2.96 [g/cm ³]	3.35 [g/cm ³]

As previous seen in last chapters, loose density depends on the particle size, particle size distribution and particle shape. The powders within a size range of 38 to 212 μm have a wider particle size distribution, so it is worth noting that the presence of smaller particles filling the gaps between larger particles can significantly elevate the loose density. Consequently, as the range of particle sizes expands, the loose density tends to increase accordingly.

4.2.2.2 Tap Density

Table 4.4 shows that powder particles with higher size range, in this case 38 and 212 μm , can compact or better saying, have a better settlement when compared powder with size range between 53 and 150 μm , with a lower size range. This wider particle size distribution is noteworthy because the smaller particles effectively occupy the empty spaces between the larger particles, leading to a more densely packed configuration and thus an increase in tap density.

Table 4.4 - Tap density results for PND 1

Sample	PND 1 (53<x<150 μm)	PND 1 (38<x<212 μm)
1	4.00 [g/cm ³]	4.17 [g/cm ³]
2	3.92 [g/cm ³]	4.17 [g/cm ³]
3	3.92 [g/cm ³]	4.08 [g/cm ³]
Mean	3.95 [g/cm ³]	4.14 [g/cm ³]

In Figure 4.7, it is illustrated the comparison between the results of loose and tap density for powders with size range between 53 and 150 μm from PND 1 and powders with size range between 38 and 212 μm .

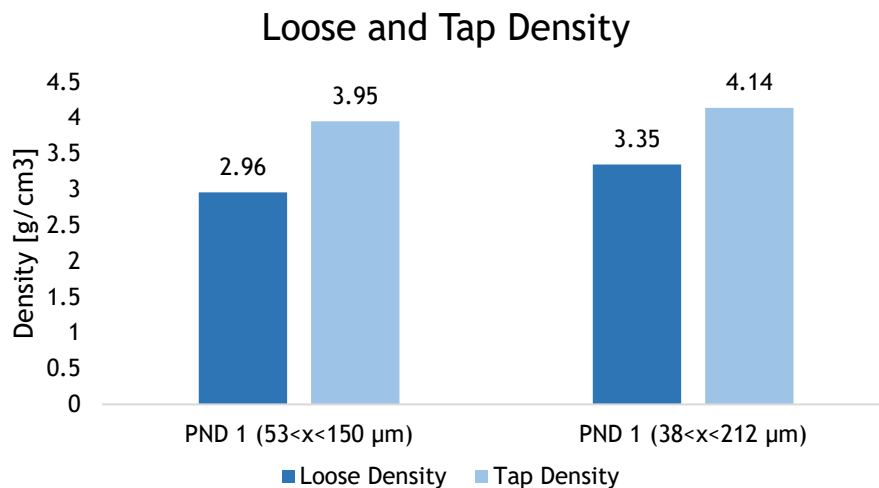


Figure 4.7 - Comparison between the tap and loose density for PND 1

In the loose state, the particles are less compacted and have more void spaces between them. This allows for greater air or empty space within the material, leading to a lower density measurement. When the material is tapped or vibrated, these void spaces are reduced, resulting in a higher density measurement. Therefore, tap density is generally higher than loose density because the compaction process increases the particle packing efficiency and reduces the amount of empty space within the material. From Figure 4.5 this occurrence is visible. On the other side, it is possible to say that powder particles with size range between 38 and 212 μm can slightly compact better, even without tapping, when compared to powder particles with size range between 50 and 150 μm . Therefore, this size range seem util ford DED.

4.2.3 Flowability Measurements

Flowability plays a crucial role in enhancing the efficiency of Additive Manufacturing processes, particularly in Directed Energy Deposition process. By conducting flowability tests, it is possible to evaluate the printability of materials, enabling them to optimize parameters and ensure smooth and consistent material flow throughout the feeding process. Table 4.5 shows the flowability measurements.

Table 4.5 - Flowability results for PND 1

Sample	PND 1 (53<x<150 µm) [s/50g]	PN1 (38<x<212 µm) [s/50g]
1	19.41	15.2
2	19.46	15.12
3	19.32	14.73
Mean	19.40	15.02

Based on these findings, it can be inferred that powders with a size range between 38 and 212 µm from PND 1 demonstrate superior flowability compared to those powders with size range between 53 and 150 µm from PND 1. It appears that the powders with a size range between 53 and 150 µm exhibit higher friction and interlocking between particles, resulting in a longer testing time and, consequently, reduced flowability compared to the other powder sample.

Castanheira [51] presented results for tap and loose density slightly lower than the ones obtained in this current study, for the same particle size range of the same milling procedure. The particle size distribution of AISI P20+Ni from this study presented a uniform particle size distribution compared to AISI 303, which may lead to better packing and this way to higher loose and tap density. At the same time, flowability for this current study is better than the one obtained in Castanheira [51].

After carefully considering the density and flowability measurements, it was decided that powder with size range between 38 and 212 µm from PND 1 would be more suitable as feedstock for DED technology. The decision was made based on the favourable combination of density and flowability characteristics exhibited by this powder, indicating its suitability for achieving optimal printing results and ensuring efficient material deposition during the DED process.

4.3 Powder Production for SLM

4.3.1 Powder Production and Characterization

4.3.1.1. Efficiency

As mentioned in Chapter 3.2.1.2, an initial step involved subjecting all the metal chips to a 5-minute milling process regardless the condition. The particles obtained from the initial milling process, which was also employed for powder production in DED, were identical to those illustrated in Figure 4.1.

Subsequently, these metal chips underwent five distinct milling procedures,

explained in Table 3.5. Figure 4.8 depicts the weight percentage of milled chips for each procedure obtained through sieving analysis. Once again, this analysis allows for an assessment of the productivity of each milling procedure, as the objective was to obtain the highest possible quantity of powder particles within the size range of 20 and 53 μm from the metal chips. It is important to note that apart from the material loss during the milling procedures, there was also some loss during the subsequent sieving processes.

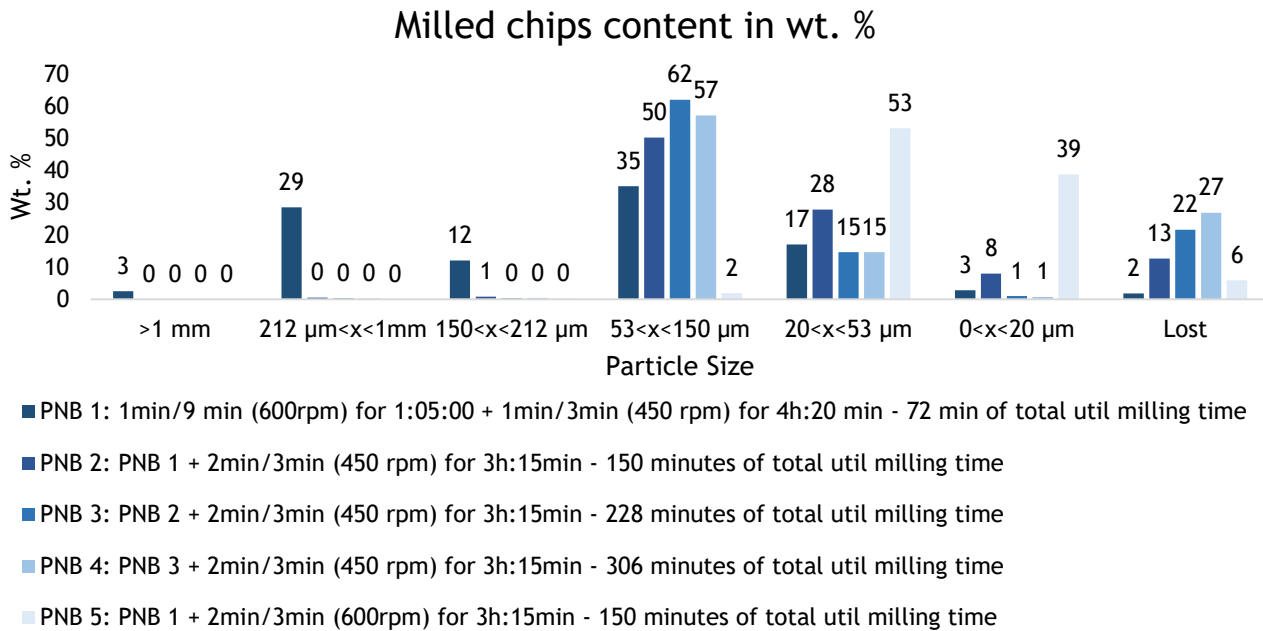


Figure 4.8 - Milled chips content in wt. % for each condition

From Figure 4.8 analysis, PNB 5 is by far the procedure with best efficiency, since it was the one with the most wt.% of particles between 20 and 53 μm , corresponding to 53%. It is also one of the tested procedures with less total milling time, 150 minutes, which makes it an optimal choice in terms of and cost-effectiveness. PNB 5 will not only exhibit lower energy consumption but also deliver comparable results when comparing to the other conditions.

PNB 1 exhibits the lowest total milling time, 72 minutes, which corresponds to half the milling time for PNB 5. Although PNB 1 consumed lower energy than PNB 5, its efficiency is approximately one-third that of PNB 5. Thus, the ratio of production time to production efficiency is not favourable for PNB 1.

When comparing PNB 2 and PNB 5, the sole difference lies in the utilization of 600 rpm instead of 450 rpm during the second cycle of the procedure, while keeping the other variables constant. Analysis of Figure 4.8 reveals that the efficiency of PNB 5 doubles in comparison to PNB 2. This suggests that employing a higher rpm, specifically 600 rpm in this case, aims to maximize the quantity of powder particles within the size range of 20 and 53 μm obtained from the metal chips.

PNB 2, PNB 3, and PNB 4 are continuous processes, each incorporating a cycle of 2 minutes milling and 3 minutes break, repeated for a duration of 3 hours and 15 minutes at 450 rpm. Transitioning from PNB 2 to PNB 3 does not offer any advantage in terms of increased milling time, as the content of milled chips by weight percentage decreases from 28% to 15%. Similarly, progressing from PNB 3 to PNB 4

maintains the same quantity of powder particles within the size range of 20 and 53 μm from the metal chips, with a weight percentage content of 15% in the milled chips. These procedures are not viable for the intended objective since productivity either decreases or remains constant with an increase in milling time.

Based on this analysis, PNB 5 demonstrates the most favourable production efficiency for particle size required for SLM process. However, due to time constraints for the realization of this dissertation, an insufficient quantity of powder feedstock was available, making it impossible to conduct density and flowability measurements, as well as printing using SLM technology.

4.3.1.2 Particle Size Distribution

Figure 4.9 depicts the particle size distribution evaluation for PNB 5, performed with the assistance of Image J software. Concurrently, Table 4.6 provides a comprehensive analysis of the particle size distribution, aspect ratio, and average particle size for PNB 5, based on image analysis.

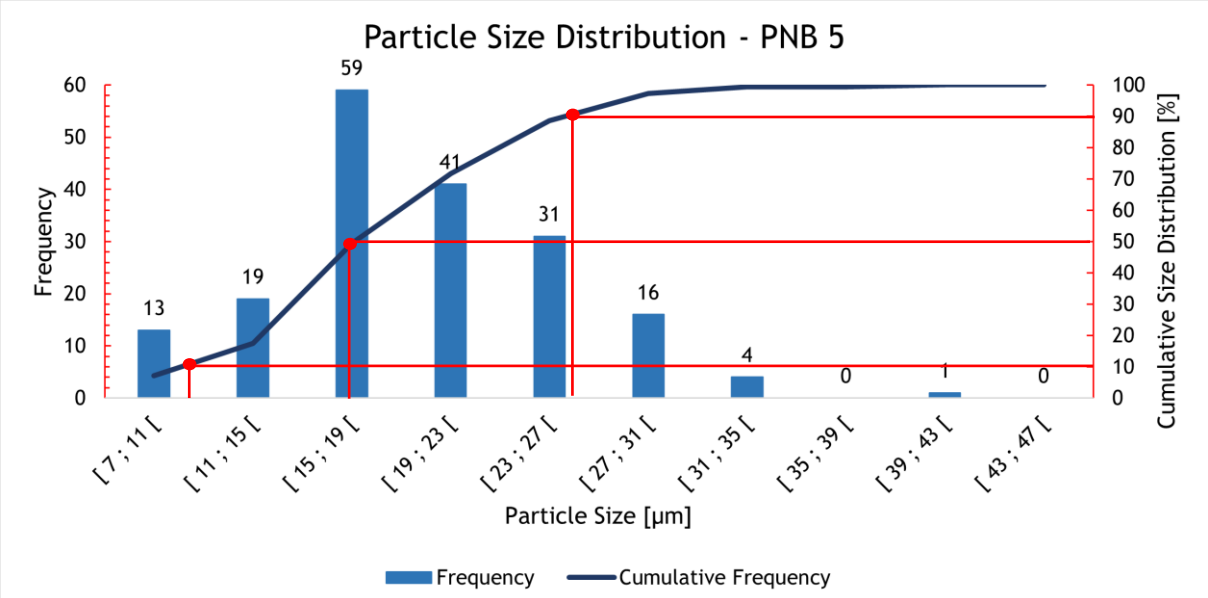


Figure 4.9 - Particle size distribution for PNB 5, measured with Image J.

A noticeable normal distribution of particle sizes is evident for PNB 5. SEM images revealed the presence of particles smaller than 20 μm . Once again, it is important to note that this happens due to entrapment of the particles or the effect of electrostatic forces during sieving. Consequently, it is conceivable that due to the extremely small size of these powder particles, they might have become suspended in the air during the sieving process and do not pass the net. Therefore, a higher percentage of particles with sizes smaller than 20 μm is observed for this particle size range analysis unlike what expected.

Table 4.6 - D_{10} , D_{50} and D_{90} values for PNB 5, according to Image J measurements.

Procedure	D_{10}	D_{50}	D_{90}	Aspect Ratio	Average Powder particle size
PNB 5	11 μm	15-19 μm	27 μm	0.72	19.92 \pm 4.69 μm

Following the analysis of Table 4.6, the D_{50} value indicates that 50% of the powder particles possess sizes smaller than the interval 15-19 μm . Conversely, the average powder particle size is 19.92 μm , which is practically the supposed low limit value for the sieving analysis. Additionally, it is noteworthy that the aspect ratio of the powder particles resulting from this procedure closely approximates 1, exhibiting a value of 0.72. An aspect ratio close to one would suggest particles with a nearly spherical shape, which is highly desirable for SLM technology as well.

Conversely, as demonstrated in Table 4.2, powder particles produce via DM exhibited an aspect ratio of 0.51. This discrepancy in aspect ratios signifies distinctions in particle morphology between the two milling methods, though it's essential to acknowledge that milling conditions also play a contributing role.

4.3.1.3 Particle shape

The powders particles resulted from milling through PNB 2 to PNB 5 were observed by SEM, and they are displayed in Figure 4.10, noted that the range size of particle analysis was 20 to 53 μm .

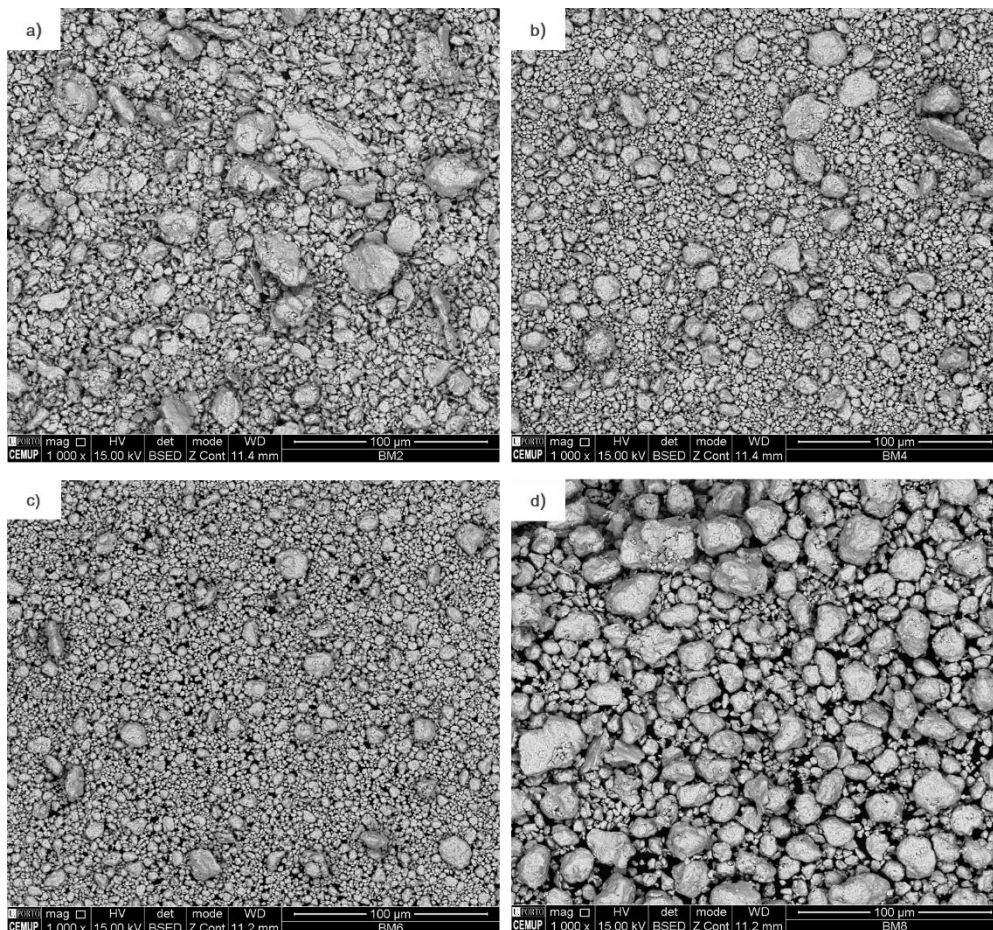


Figure 4.10 - SEM images of particles with a size between 20 μm and 53 μm resultant from a) PNB 2 b) PNB 3 c) PNB 4 and d) PNB 5

Figure 4.10 depicts that each Ball Milling Procedure resulted in the occurrence of cold welding. Figure 4.10 a) illustrates that PNB 2 generally produced angular-shaped particles, although some flaky particles are still discernible. The particle shape appears highly irregular. Adding a cycle of 2 minutes milling and 3 minutes break, repeated over a period of 3 hours and 15 minutes at 450 rpm,

obtaining PNB 3 led to powder particles with rounded shape and irregular at the same time (Figure 4.10 b)). Comparing PNB 2 and PNB 3, it is notable that a considerable number of smaller particles is present, indicating the dominance of the fracture process over cold welding. Upon examining Figure 4.10 c), which displays powder particles from PNB 4 and considering that it is a continuation of PNB 3 with an increased milling time, there appears to be no noticeable morphological alteration in the particle shape.

In contrast, Figure 4.10 d) provides an analysis of powder particles from PNB 5, where a pronounced presence of the cold-welding phenomenon is observed due to the reduced number of smaller particles. Considering that milling speed is a parameter influencing the occurrence of cold welding, it is reasonable to assert that the use of 600 rpm induced intense mechanical forces during milling, leading to the bonding of smaller powder particles and the consequent manifestation of this phenomenon. It is worth noting that PNB 2 and PNB 5 are similar procedures, differing only in the rpm used during the second cycle, transitioning from 450 rpm to 650 rpm. Comparing the particle shapes from both processes is intriguing because the increase in rpm alone resulted in a heightened cold-welding phenomenon and the formation of thicker particles with shapes closer to rounded. However, PNB 5 should be further optimized to attain rounded/spherical powder shapes with an aspect ratio close to 1, which is desirable for SLM applications.

In the context of the present investigation, the planetary ball milling technique was implemented employing ball sizes of 5 mm and 30 mm. This choice of ball dimensions draws from a study conducted by Fullenwider et al. [55], who explored the feasibility of employing a two-stage ball milling approach for recycling machining chips into an alternative feedstock powder tailored for metal additive manufacturing. This study concludes that the use of larger ball (20 mm) efficiently break up machining chips into coarse powder particles, while smaller balls (diameter = 6 mm) effectively modify the powder morphology toward a near-spherical configuration - particularly suitable for AM applications. It is noteworthy that the ball-to-powder weight ratio plays a pivotal role in determining the overall energy transfer from the milling balls to the particles, while the ball diameter stands as a critical milling parameter influencing the force per impact, stress per impact, and impact frequency [55].

Figure 4.11 provides a closer inspection of a high magnification SEM image of powder particles from PNB 5. The cold-welding effect is clearly visible, as explained before, with small particles bonding together. Additionally, despite observing powder particles with shapes approaching rounded, there are still some flake-shaped particles discernible - as depicted in Figure 4.11 a).

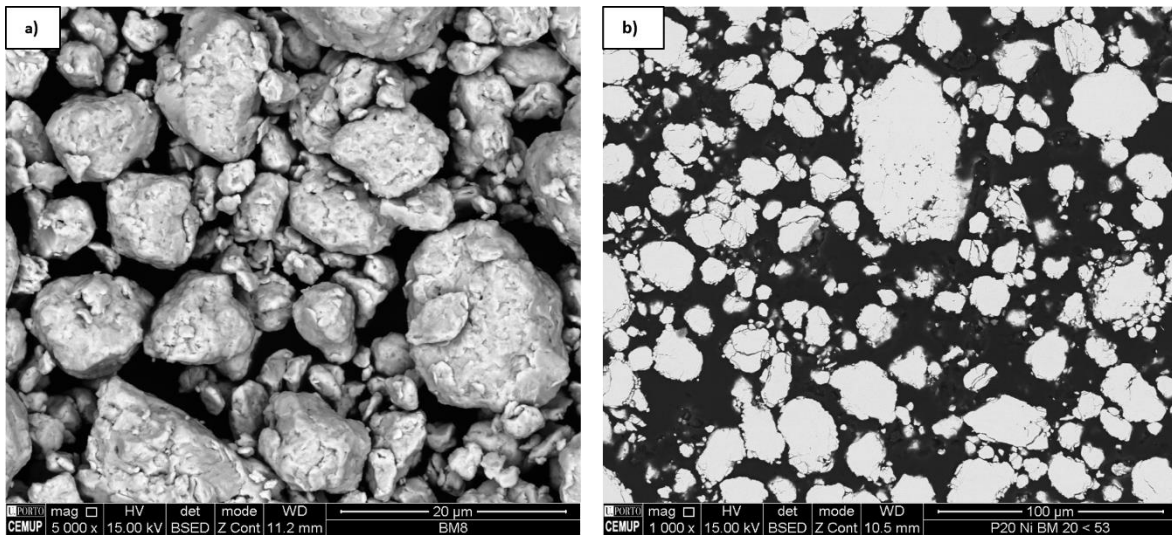


Figure 4.11 - SEM images of: a) particles with a size between 20 μm and 53 μm resultant for PNB 5. b) polished particles with a size between 20 μm and 53 μm resultant for PNB 5.

In Figure 4.11 b) it is possible to see some microporosities in the powder particles. Planetary ball milling is characterized by the repetitive collision of milling balls with powder particles, a process characterized by high-energy impacts that can result in the fracturing of particles. Within the course of this fracturing process, it is conceivable for minute voids or microporosities to emerge within the particle structure. Simultaneously, regions of compacted material and microporosities at the interfaces between particles can be attributed to the phenomenon of cold-welding.

4.3.2 Microhardness Measurements

Since the application of conventional powder metallurgy (compaction and sintering) can be interesting for rounded particles or even sintering route additive manufacturing, thus hardness measurements were performed. Table 4.7 presents the results of microhardness measurements of the original AISI P20+Ni metal chips and the powder particles produced by PND 1, via disc milling for size ranges between 38 and 212 μm ; and powder particles produced by PNB 5, via planetary ball milling for size ranges between 20 and 53 μm . In Appendix E, OM images depicting the indentations of these samples are presented.

Table 4.7 - Microhardness of the chips and powder particles.

Sample	Microhardness
AISI P20+Ni Metal Chips	532 \pm 31 HV 0.01
Powder Produced by PND 1 (38<x<212 μm) – Disc Milling	532 \pm 26 HV 0.01
Powder Produced by PNB 5 (20<x<53 μm) – Planetary Ball Milling	1730 \pm 99 HV 0.01

Based on the acquired findings, it is evident that the Vickers microhardness of the chips aligns with that of the AISI P20+Ni tool steel, as presented in Table 3.2 [47,48]. Simultaneously, the powder produced via disc milling, PND 1, demonstrates a comparable Vickers microhardness value to that of the AISI P20+Ni metal chips.

This outcome can be attributed to the fact that the plastic deformation experienced during both the machining process, to produce metal chips, and the milling process, to obtain powder, was insufficient to induce work-hardening in these samples. It should be noted that plastic deformation results in work-hardening, a phenomenon that strengthens the material. This occurs as dislocations are impeded in their mobility, and new dislocations may form, ultimately promoting an enhancement in material strength. On the other hand, when comparing the powder produced via disc milling, PND 1, with that obtained through planetary ball milling, PNB5, a significant increase in hardness values becomes apparent. This phenomenon is anticipated due to the higher energy intensity and generation of elevated impact forces in planetary ball milling compared to disc milling. These intense forces induce severe plastic deformation of the particles, consequently resulting in an increase in hardness values. Moreover, this process leads to a greater accumulation of internal strain, further contributing to the grain refinement of powder structures. However, there was no opportunity to perform EBSD and TEM analysis.

4.4 Printings through Direct Energy Deposition

4.4.1 Parametrization Process

The initial phase of printing with DED involves the parametrization process. It is crucial to thoroughly examine the specific feedstock and substrate materials, along with the variables and features of the printing equipment, to determine the ideal parameters for a successful DED process. This chapter highlights the significant steps taken and the results obtained during the investigation and selection of optimized printing parameters.

4.4.1.1 Line Printings

Design of Experiments (DOE) was performed using Taguchi L9 Method to build 8 different parameter combinations, however final parameters combinations were selected according to the equipment and previous results [54]. Initially, 8 lines were printed while varying the laser powder, scanning speed, and powder feed rate, with the shielding gas set at 20 l/s. Subsequently, 11 additional lines were printed with the shielding gas set at 5 l/s. The remaining parameters discussed in Chapter 3.3.1 were held constant for printing. Table 4.8 outlines the parameters applied for these lines, considering crucial process variables like energy density and powder deposition density.

Table 4.8 - Printing parameters according to the literature review, combined considering the Taguchi L9

Line	Laser Power [W]	Scanning Speed [mm/s]	Powder Feed Rate [g/min]	Global Energy Density [J/mm ²]	Powder Deposition Density [g/mm ²]
1	500	14.2	8	17	0.004
2	900	14.2	3	30	0.002
3	500	7.5	6	32	0.006
4	900	7.5	8	57	0.008
5	1800	14.2	6	61	0.003
6	1800	8.0	4	107	0.004
7	500	2.0	3	119	0.012
8	1800	6.0	8	143	0.011

Figure 4.12 depicts the top views of the first 8 printed lines through DED.

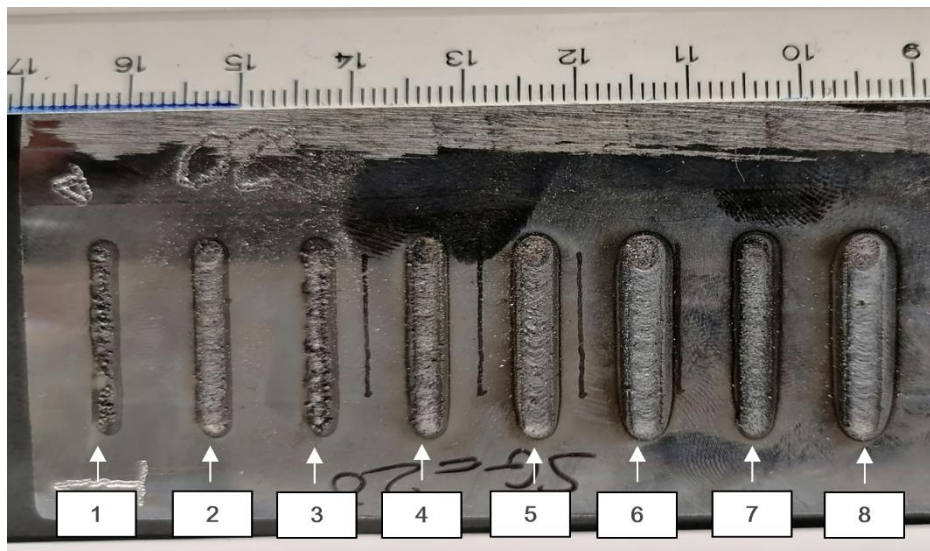


Figure 4.12 - Top views of the first 8 printed lines

Lines 1, 2, 3, and 4 appear excessively thin, with minimal amounts of printed material and discontinuities. Moreover, several unmelted powder particles can be observed surrounding these lines. Line 7 also appears slightly thin, however the global energy density and powder deposition density is higher, when compared to the first analysed lines. The combination of both scanning speed and powder feed rates being low, leads to a high global energy density, and in this case, it is possible to see that despite being a thin layer, it looks like it is high in height. This will be confirmed in the cross-section view in Figure 4.13.

Lines 5, 6, 7 and 8 exhibit noticeable burn marks in the outer regions. Lines 5, 6 and 8 were the lines where laser power was the highest, being 1800 W. However, when comparing line 5 with lines 6 and 8, it becomes apparent that line 5 has a rougher printed surface, likely due to a higher scanning speed, which ultimately results in a lower overall energy density. Line 6 and 8 look quite interesting because they have a bright printing surface.

Based on this visual analysis, it can be concluded that using low power lasers and high scanning speeds does not lead to compelling depositions. The lines with higher global energy density appeared to be potential candidates for further study. However, a more thorough examination of cross-sections will be conducted to gain a better understanding of how these parameters influence the results.

Figure 4.13 displays the cross-section views of the first eight printed lines. Table 4.9 presents the corresponding geometrical measurements obtained from images of Figure 4.13 using the Image J software.

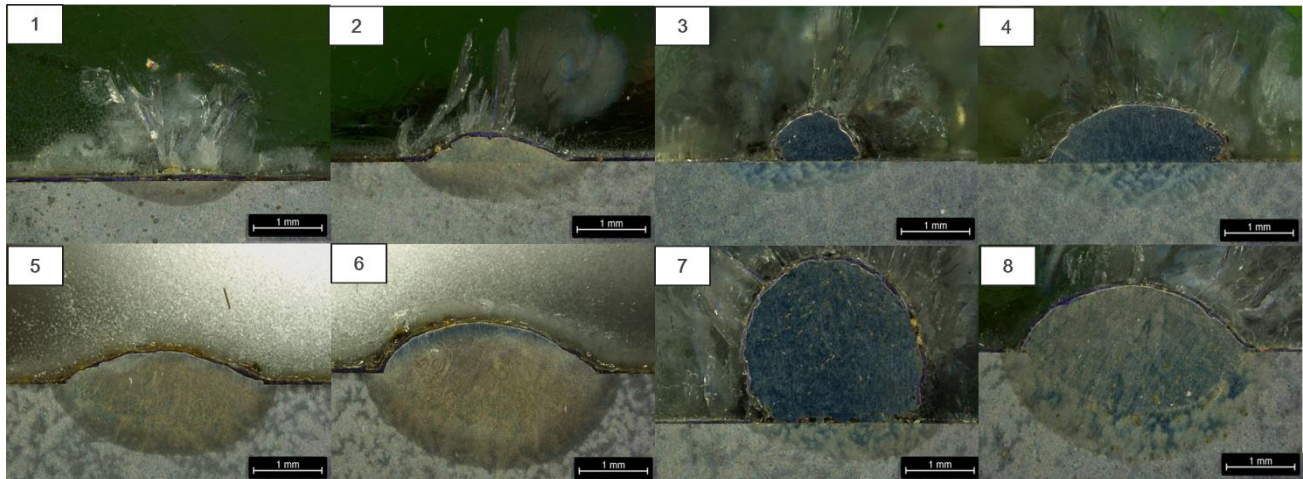


Figure 4.13 - Cross section views of the first 8 printed lines.

Table 4.9- Geometrical measurement results of the first 8 printed lines.

Line	w [mm]	h [mm]	d [mm]	AR h/w	θ [°] left	θ [°] right	Am [mm ²]	Ap [mm ²]	D [%]
1	1.40	-	0.16	-	-	-	-	-	-
2	1.99	0.25	0.35	0.12	43	28	-	0.39	-
3	1.07	0.66	0.23	0.62	39	61	-	0.58	-
4	2.42	0.76	0.41	0.31	57	40	-	1.45	-
5	2.78	0.44	0.71	0.16	41	20	1.53	0.76	67
6	3.12	0.73	0.93	0.23	62	41	2.41	1.53	61
7	1.94	2.10	0.32	1.08	-	47	-	4.69	-
8	3.14	0.89	1.03	0.28	54	42	2.56	2.00	56

This illustrates the considerable influence of the examined processing parameters (laser power, scanning speed, and powder feed rate) on both the production of the deposition and its adhesion to the substrate.

Initially, it is evident that lines 1, 2, 3, 4, and 7 exhibit no dilution due to the absence of fusion between the printed material and the substrate. Conversely, dilution and the formation of a heat affected zone (HAZ) are observed only in lines 5, 6, and 8. Nevertheless, no internal defects, such as porosities or lack of fusion, are detected in any of the deposited lines.

Line 1 exhibits no height at all due to low powder deposition density, resulting from a combination of high scanning speed and low potential. Additionally, lines 2, 3, and 4 demonstrate low depth, which can be attributed to their low global energy

density arising from a combination of high scanning speed, low laser power and small feeding rates. Similarly, Line 7 displays a low depth, but paradoxically, a high height, resulting from a high global energy deposition. Furthermore, this line exhibits relatively high angles and reveals substantial discrepancy values between the left and right angle. Such characteristics are highly undesirable as they compromise the final properties of the depositions. Consequently, based on these observations, Lines 1, 2, 3, 4, and 7 are disregarded from further consideration.

Line 5, despite showing the phenomenon of dilution, presents low bead height which is a result of high scanning speed with low powder feed rate leading to a low powder density deposition. Both line 6 and 8 show an interesting bead geometry. Both lines used the same amount of laser powder, but both global energy density and powder deposition density for line 8 are higher than line 6 which led to higher bead high. At same time, line 8 presents lower dilution when compared with line 6 though it was made by a lower scanning speed (despite using the same laser power) but with a higher powder feeding.

Upon analysing the different characteristics, it is concluded that, in terms of visual appearance, lines 6 and 8 are the most suitable in the initial phase. Nevertheless, the bead height of line 8 shows a better combination of scanning speed and powder feed rate which might be an appropriate selection of parameters for the next printing steps.

As presented in Table 3.6, new lines were printed reducing the shielding gas to 5 l/s due to the hypothesis of turbulence at high flow rate. New printing lines are illustrated in Figure 4.14. In addition to the parameters presented in Table 4.8, three new conditions were tested as listed in Table 4.10.

Table 4.10 - Printing parameters for lines 17 to 19

Line	Laser Power [W]	Scanning Speed [mm/s]	Powder Feed Rate [g/min]	Global Energy Density [J/mm ²]	Powder Deposition Density [g/mm ²]
17	500	4.0	3	60	0.006
18	900	2.0	3	214	0.012
19	900	6.0	8	71	0.011

*Lines 9 to 16 are equivalent with lines 1 to 8 from Table 4.8, respectively.

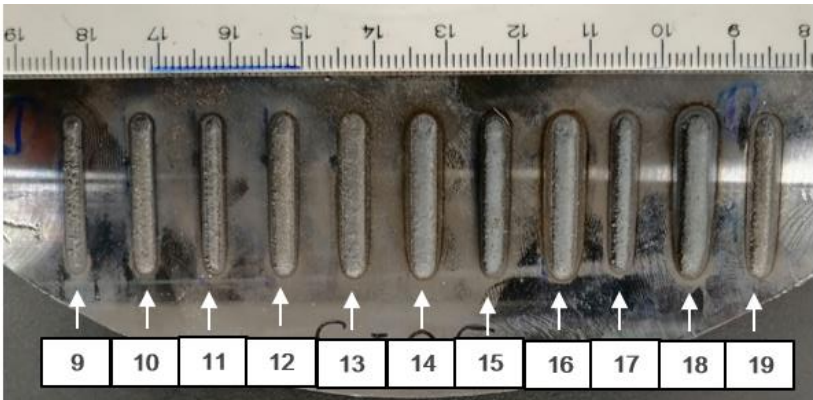


Figure 4.14 - Top views of lines 9 to 19

Visual observations, Figure 4.14, shows that reducing the shielding gas flow rate from 20 l/s to 5 l/s resulted in better metallic aspect and a surface that is more uniform and less rough. This can be attributed to reduced turbulence during printing. In comparison to the first 8 lines, these new experiments exhibit fewer signs of burning. There is also the possibility that before, for the first 8 lines, the shielding gas flow rate was too high which ended up spreading the powder around the track.

Lines 9 to 13 exhibit a notably diminutive width, once again, due to reduced powder deposition density. This is a combination of high scanning speed with too low powder feed rate, which indicates there is less time for the material to fully melt, consequently leading to a consistent presence of unmelted particles within the lines. Moreover, excessively high scanning speeds can give rise to lack of fusion and porosity.

Line 14 appears as an interesting deposition just by its metallic and bright surface that presents. Cross-section analysis will help to evaluate this line. On the other hand, lines 15, 17, and 19 appear excessively thin. When comparing lines 15 and 17, a twofold increase in scanning speed is observed, consequently leading to a reduction in global energy deposition by half. A reduction in energy density results in a reduced heat input into the material, potentially causing inadequate melting of the deposited material and compromising the bonding to the substrate. Comparing line 15 with line 18, where the laser power was nearly doubled, the global energy density also approximately doubled. This higher heat input into the material fosters more efficient melting and fusion, consequently resulting in a broader deposition in line 18.

Figure 4.15 illustrates the cross-sectional views of each line, such as bead, dilution and HAZ. Moreover, Table 4.11 presents the measurements obtained using the Image J software, offering quantitative data corresponding to each line's characteristics.

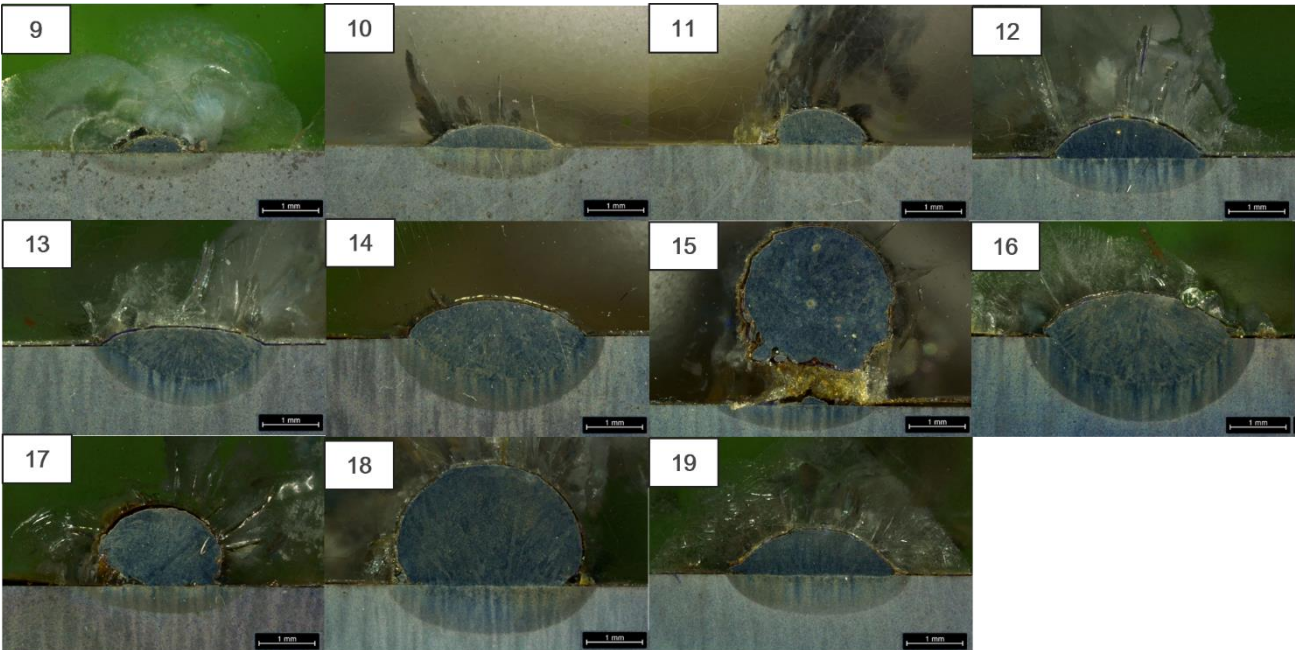


Figure 4.15 - Cross section views of lines 9 to 19

Table 4.11- Geometrical measurement results of lines 9 to 19.

Line	w [mm]	h [mm]	d [mm]	AR h/w	θ [°] left	θ [°] right	Am [mm ²]	Ap [mm ²]	D [%]
9	0.99	0.32	0.26	0.32	36	51	-	0.24	-
10	2.32	0.39	0.35	0.17	32	30	-	0.61	-
11	1.52	0.63	0.20	0.42	139	48	-	0.77	-
12	2.53	0.69	0.40	0.27	48	39	-	1.33	-
13	2.87	0.36	0.87	0.13	35	26	1.91	0.75	72
14	3.12	0.70	1.02	0.22	57	40	2.68	1.48	64
15	-	-	-	-	-	-	-	-	-
16	3.20	0.83	1.26	0.26	48	56	3.56	1.78	67
17	1.30	1.37	0.30	1.05	-	96	-	2.34	-
18	2.94	2.14	0.60	0.73	-	131	-	5.95	-
19	2.89	0.79	0.50	0.27	45	41	-	1.71	-

Thus, it becomes apparent that lines 9, 10, 11, 12, 15, 17, 18, and 19 exhibit a noticeable absence of dilution. These specific lines correspond to the deposition parameters with the lowest laser power, namely 500 W and 900 W. It appears that employing lower power is ineffective in facilitating dilution and establishing a bond between the printed and substrate materials. The energy provided is insufficient for achieving this outcome. Consequently, the parameters associated with these lines are automatically excluded.

Unlike lines 14 and 16, line 13 exhibits a small bead height despite displaying dilution. This could be attributed to the combination of a high scanning speed and a low powder feed rate, resulting in a lower density of powder deposition. Upon comparing line 14 and line 16, both exhibit interesting cross-section characteristics. Line 16 demonstrates a higher overall energy density compared to line 14, because despite having the same laser power, the scanning speed for line 16 is slightly lower. Consequently, more energy is available to melt the substrate, as evidenced by the greater depth observed in Figure 4.13 and Table 4.11. Furthermore, line 16 displays a slightly greater height in comparison to line 14. Additionally, the aspect ratio (AR), representing the ratio between height and width, is higher for line 16. Considering these factors collectively, it was determined that the combination of parameters from line 16 would be adopted for further investigation in the study.

4.4.1.2 One-layered Printings

Considering the combination of parameters from line 16, it was decided to initially produce three different one-layered printings of 25 x 25 mm with overlapping of 40, 50 and 60 %. Figure 4.16 and 4.17 presents the top and cross-section views for these constructed layers, respectively. Moreover, Appendix F presents the cross-section views with higher amplification to a better understanding of the surface quality of these one-layered printings.

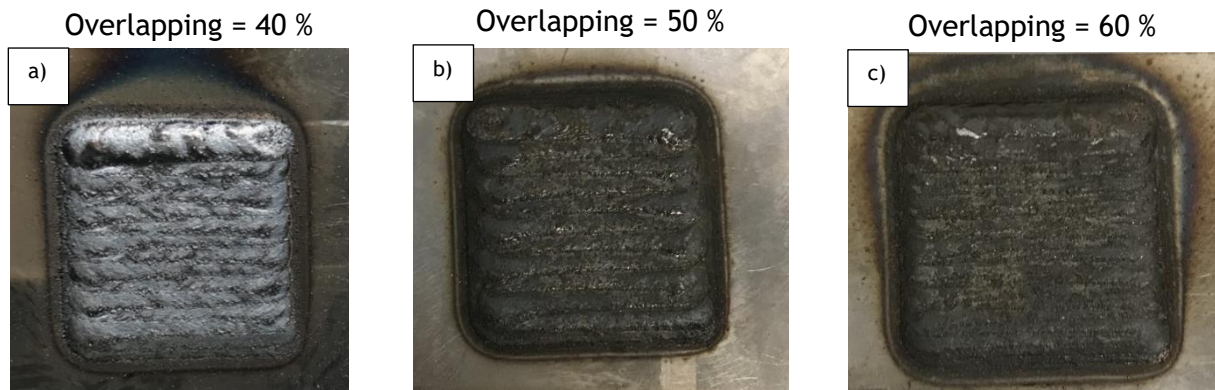


Figure 4.16 - Top view of the layers with combination of parameters from line 16 with: a) 40% overlapping, b) 50% overlapping and c) 60% overlapping.

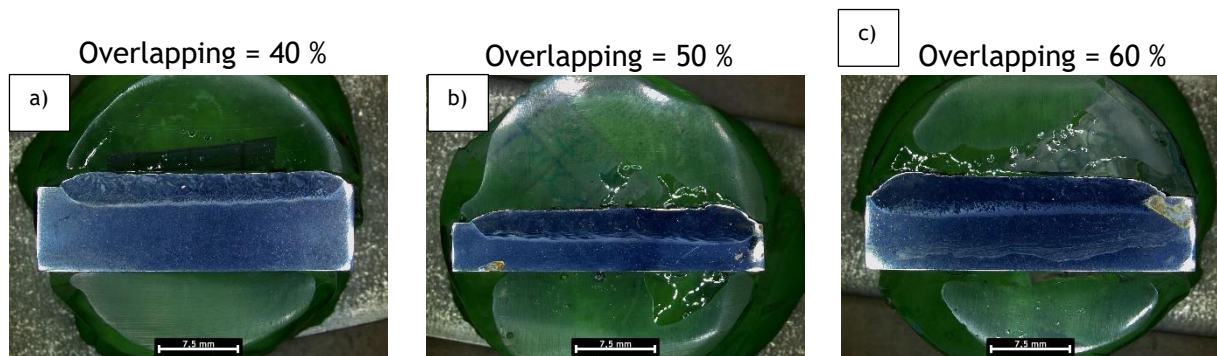


Figure 4.17 - Cross section view of the layers with combination of parameters from line 16 with: a) 40% overlapping, b) 50% overlapping and c) 60% overlapping.

In Figure 4.16 a), the top view of this one-layered printing appears interesting with a metallic colour, however, upon closer inspection, it becomes apparent that the substrate exhibits a burned area, likely a consequence of high laser power density. Moreover, a visual examination of the cross-section view reveals several noticeable defects. Analysing Figure 4.16 b) and c), the top section appear with more surface roughness when comparing to the previous layer - Figure 4.16 a). However when analysing the cross-section views, Figure 4.17 b) and c) and taking into account Appendix F, they appeared to present less amount of defects when compared to the previous layer, during experimental work, standing out layer produced with 60% of overlapping that seem to presents less deffects, only by analysing at naked eye. However, an in-depth analysis of Appendix F reveals the presence of various defects, including irregular shaped pores, classified as porosities due to lack of fusion, and spherical gas pores. To address these defects, particularly the lack of fusion porosities, a viable solution was to increase the global energy density by raising the laser power from 1800 W to 1900 W, ensuring complete melting of the powder feedstock. Consequently, two more one-layered printings were performed with

overlapping of 50% and 60%, using the combination of parameters from line 16, with the sole modification being the laser power set at 1900 W - represented in Figure 4.18.

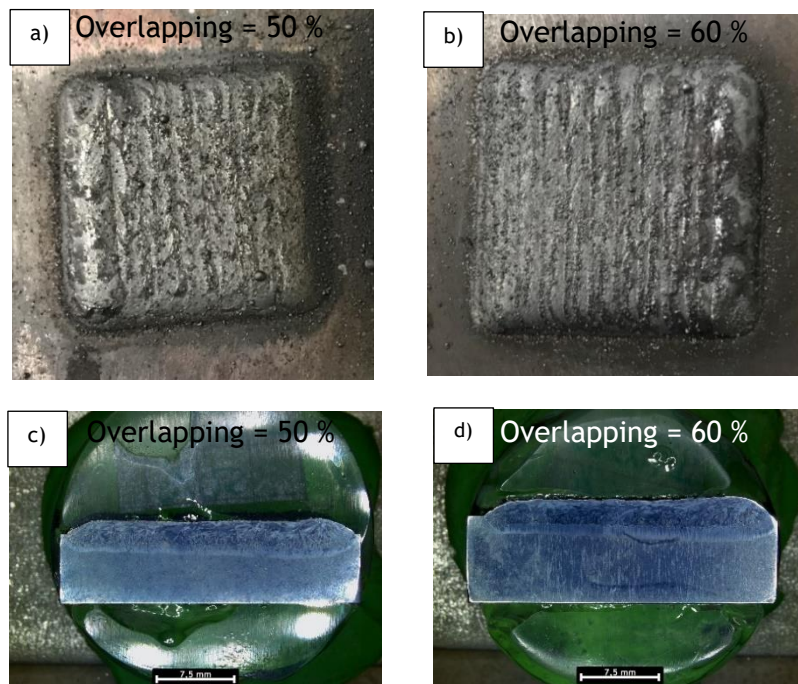


Figure 4.18 - Top and Cross-section views of the layers with combination of parameters from line 16 (laser power of 1900 W) with: a) 50% overlapping, b) 60% overlapping, c) 50% overlapping and c) 60% overlapping.

Analysing the top view of these new one-layered printings, Figure 4.18 a) and b), it is possible to see presence of oxidation, specially in the substrate material. However, the deposited material presents a more intense metallic colour when compared to the one-layered printings from Figure 4.16 b) and c). Regarding visual observation, the sample with overlapping of 50%, represented by Figure 4.18 a) and c), shows a rougher surface when compared to the sample with 60% of overlapping, represented by Figure 4.18 b) and d). During the experimental work, these two samples represented in Figure 4.18 were subjected to microscopic observation (MO analysis), revealing a higher quality surface compared to the previous three samples depicted in Figure 4.16. This suggests that these samples exhibit a reduced number of defects, such as lack of fusion porosities and keyhole pores. Notably, the sample represented in Figure 4.18 b) and d), where overlapping refers to 60%, displayed the most promising results (0.28 mm² of porosit area). For the next step of this research, the production of a multilayered volume through DED technology, it was decided to proceed with the combination of parameteres from this last mentioned sample. Due to time constrains, the decision of the optimization of parameters relied on visual inspection during the experimental work. Nevertheless, a more rigorous analysis has been conducted using the Image J software, considering Appendix F, to measure the area of porosities observed on the surface of each sample. The results of this analysis are presented in Table 4.12. Considering the outcome of the porosity area analysis, the decision regarding the best combination of parameters for the production of the multilayered volume may have been different. Possibly, the combination of parameters from sample C or D would have yielded promising results.

Table 4.12 - Combination of printing parameters and porosity area for one-layered printing samples.

One-layered Printing	Laser power [W]	Scanning Speed [mm/s]	Powder Feed Rate [g/min]	Overlapping [%]	Porosity area [mm ²]
A	1800	6.0	8.0	40	0.23
B				50	0.33
C				60	0.16
D	1900			50	0.17
E				60	0.28

4.4.1.3 Multilayered Printings

The parameters for the multiple-layered printings were predetermined to be those specified in line 16, just by changing laser power for 1900 W with a 60% overlapping (combination of parameters from sample E of the one-layered printing). When printing more than one layer, two critical variables need to be defined. Firstly, the rotation between successive layers must be determined. As the raster path consistently presents all lines in the same direction, it is customary to alter the direction of the lines from one layer to the next. Secondly, the height of the subsequent layers must be established. The stand-off distance remains consistent at 13 mm, mirroring the approach employed in line printings. However, for subsequent layers, careful consideration of height displacement is required to ensure the proper construction of consecutive layers. Consequently, the average height of the initial layer is measured, affording an indication of the necessary displacement along the z-axis for the ensuing layer. In the case of the optimized layer, sample E, height measurements were obtained at various locations using a calliper, culminating in an average height of 1.09 mm. To foster strong cohesion between the consecutive layers, it is advisable for the two layers to be positioned near one another. This way it was established a height of 1.09 mm, with a zig-zag printing strategy with 90° rotation between subsequent lines.

Considering these factors, two multilayered volumes, consisting of 6 layers, were produced for the purpose of investigating microstructure, microhardness, and potential defects across building direction. Figure 4.19 illustrates both multilayered volumes consisting of six layers each.



Figure 4.19 - Printed multilayered volume with the optimized parameters.

Upon analyzing Figure 4.19, notable observations can be made regarding the printed material. The surface exhibits a prominent degree of extreme oxidation, giving a dark appearance and a notably rough texture. Furthermore, the substrate

indicates a burnt aspect, likely attributed to the utilization of a high laser power setting of 1900 W. This finding leads to an initial conclusion that the protection conditions were not adequate for AISI P20+Ni steel. Additionally, the surrounding areas of these printed volumes exhibit significant traces of powder spattering, where particles were expelled or scattered during the process, resulting in surface irregularities and imperfections in the final print. Furthermore, unmelted powders are discernible on the surface of the volumes. Considering these observations, it is strongly advised to optimize the process parameters for future depositions, as the quality of these volumes does not meet expectations. However, due to time constraints, the study proceeded with these samples.

4.4.1.3.1 Microstructure Analysis

To perform the microstructure analyses, the printed material was selected as the subject of investigation. Figure 4.20 presents the cross-section view of the final multilayered volume. Note that this sample was subjected to chemical etching.

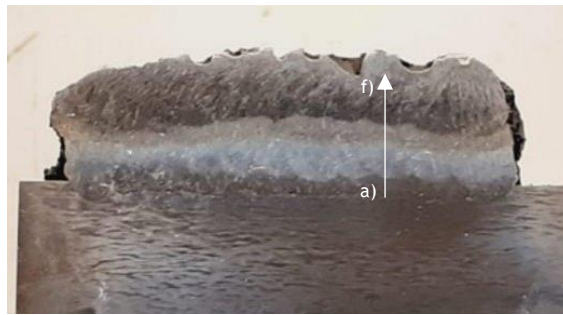


Figure 4.20- Cross section view of the printed multilayered volume

This printed volume comprises six layers, almost distinguishable on the etched surface. Nevertheless, notable defects are observed close to the substrate, as seen in Figure 4.20. When evaluating the efficacy of powder metallurgy techniques, particularly AM methods like DED, studying porosity becomes crucial. This is attributed to the direct influence of porosity on the resultant material's mechanical properties. As depicted in Figure 4.21 a), the presence of lack of fusion porosities, characterized by their irregular shapes, is discernible adjacent to the interface between the deposited and substrate material. The presence of these defects may be attributed to insufficient energy input. The global energy deposition for this deposition is 151 J/mm^2 , where the laser power is 1900 W and scanning speed is 6 mm/s, considering the laser spot size of 2.1 mm. Figure 4.21 b) presents porosities identified as gas entrapment.

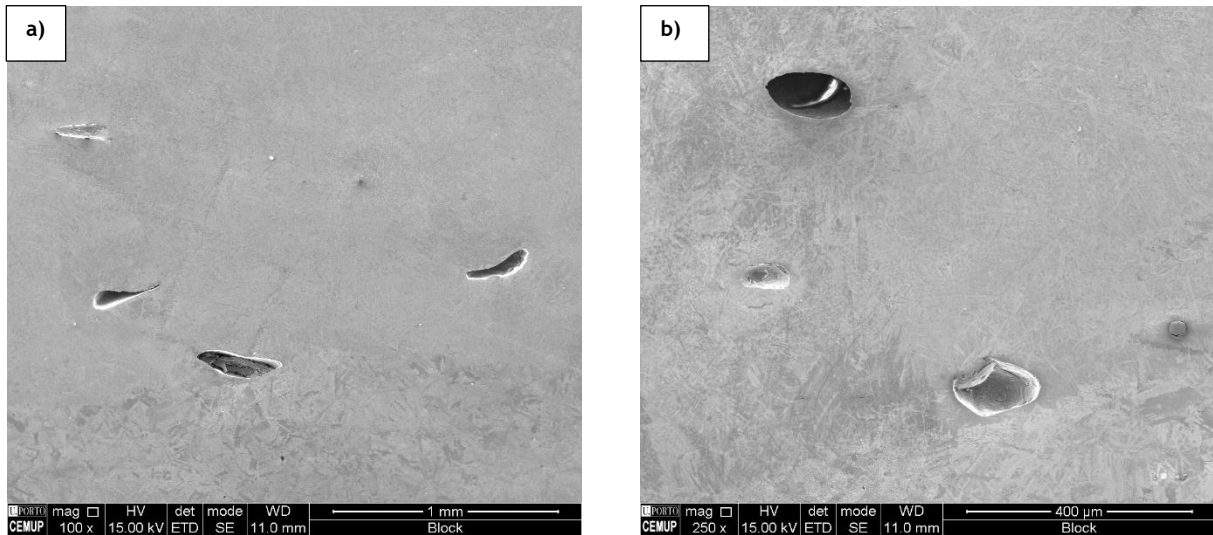


Figure 4.21 - SEM-BEI images of the porosities of the printed multilayered volume

The microstructure of the deposited AISI P20+Ni steel is depicted in Figure 4.22, where a) refers to a zone close to the substrate, and f) to the top most region as mentioned in Figure 4.20 .

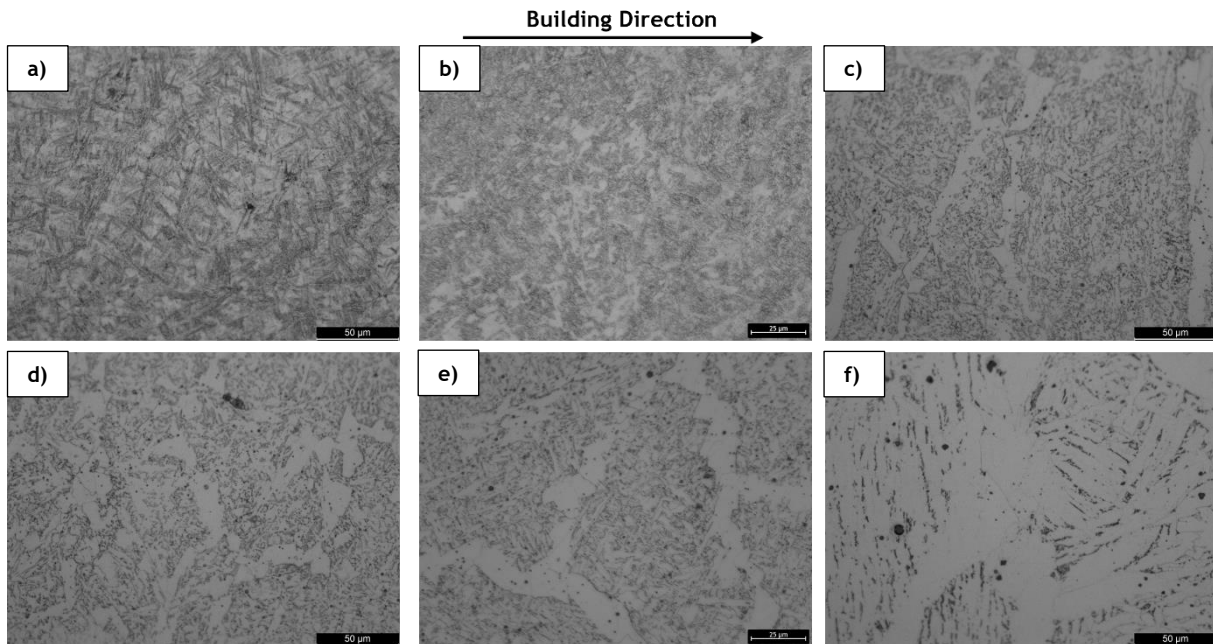


Figure 4.22 - OM images of the deposited material

Figure 4.22, confirms that the microstructure of the printed material changes along the built direction, i.e., in the beginning of the printing there is a combination of tempered martensite. Martensite is a hard and brittle phase that forms during rapid quenching from the austenitizing temperature. When subjected to tempering, martensite becomes more ductile and less brittle, a quality highly sought after for mold applications, which holds particular relevance for this specific material. This way, it can be inferred that in the first deposited layer, there is formation of martensite because the metal suffers a fast cooling due no pre-heating of the substrate. After, in subsequent layers, the martensite will become tempered due to the heat generated. Leaving the dilution and reaching to the top most region, the martensite reduces, ferrite appears, martensite weakens and becomes more rounded. Moreover, dark and fine particles are appeared.

4.4.1.3.2 Evolution of Chemical Composition Analysis

The chemical analysis on the cross section along the building direction was carried out to evaluate the severe microstructure change seen in Figure 4.22. Table 4.13 presents the SEM-EDS results, encompassing distinct regions of the examined samples. It is noteworthy to mention that the designations of the layers—Layer 1, Layer 2, and Layer 3—refer to locations in proximity to the substrate, progressing along the build direction. This progression culminates with the layer termed "almost top", corresponding to the region farthest from the substrate.

Table 4.13 - Chemical composition of different parts of the multilayered volume (wt. %)

	C	Si	Cr	Mn	Mo	S	Ni	Fe
AISI P20+Ni Metal Chips	0.51	0.77	2.11	1.73	0.38	<0.0055	0.79	93.70
Almost Top *	0.67	0.3	1.46	0.66	-	-	-	96.91
Layer 3 *	0.49	0.34	1.81	0.91	-	-	-	96.45
Layer 2 *	0.66	0.56	2.12	1.27	-	-	-	95.39
Layer 1 *	0.76	0.46	2.05	1.43	0.45	-	-	94.85
Substrate *	0.72	0.49	1.37	1.05	-	-	-	96.37

* Chemical composition obtained via SEM-EDS analysis.

Note that, once again Carbon should not be considered for this semi-quantitative analysis, since it is not possible to obtain an accurate result for it. From this first analysis it is possible to see that when it goes from the substrate to the layer 1, the amount of Cr and Mn significantly increases. This outcome aligns with expectations, as this region encompasses a combination of the substrate material and the deposited material. However, tracing the development along the built direction of this sample, an apparent decrease in the contents of certain elements, namely Si, Cr, and Mn, becomes apparent. To gain a more comprehensive understanding of this phenomenon and to validate these findings, a secondary chemical composition analysis was conducted. In this case, a profile of the sample was investigated, as seen in Figure 4.23. Afterwards, a punctual SEM-EDS analysis was performed in some constituents of the final printed multilayered volume, Figure 4.24, where Appendix G presents the EDS spectra for this analysis.

Printed Block - Chemical Composition Evolution

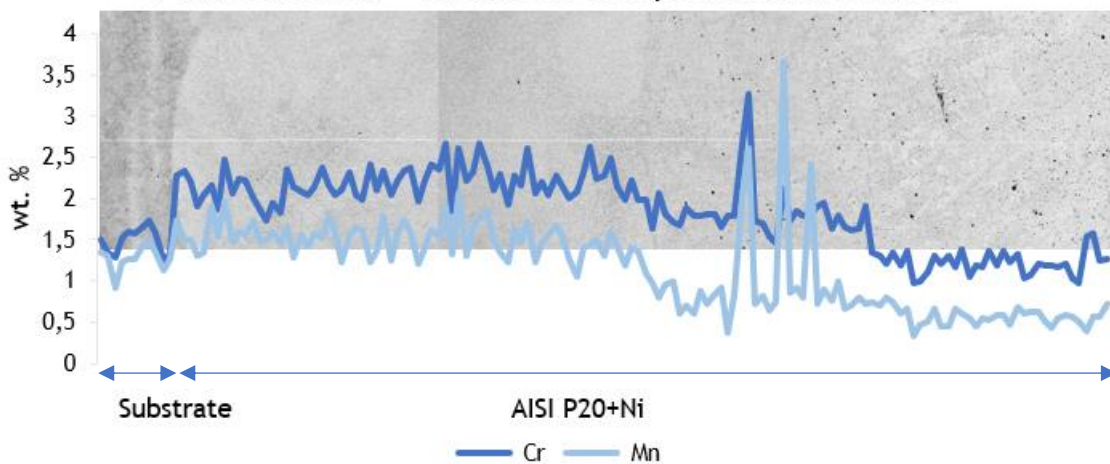


Figure 4.23- Chemical Composition Profile for the printed multilayered volume

Figure 4.23 refers only to Cr and Mn wt. % since they were the elements that underwent the greatest change. However, in Appendix H it is possible to verify the evolution of other elements such as Si, Mo and Ni. From this analysing it is possible to verify that Cr and Mn wt. % decreases along the built direction of the final printed multilayered volume. This is not an interesting evolution because these two elements play crucial roles in enhancing the performance and versatility of the steel. Chromium is strategically incorporated into steel to increase its resistance to corrosion, wear, and hardenability. Conversely, manganese contributes to the steel's toughness, rendering it less susceptible to cracking or fracturing during real-world applications.

Alloying elements, notably Cr, Mn, and Ni, play a significant role in shaping the microstructure of steel. In this case, the reduction in allowing elements can affect the stability of certain phases. The presence of alloying elements such as Cr and Ni plays a pivotal role in stabilizing the austenitic phase (γ) at elevated temperatures, characterized by its face-centred cubic (FCC) crystal structure. Consequently, when rapid cooling is encountered, like during the initial stages of printing in this study, martensite is formed. Conversely, it is noteworthy that based on the data presented in Figure 4.23, and the considerations outlined in Appendix H, the content of Cr and Ni tends to diminish along the build direction. This decrease in Cr and Ni content implies that austenite becomes progressively less stable at higher temperatures. Taking this into considerations, along with the fact that cooling rate is getting slower along the build direction, the presence of ferrite becomes increasingly evident. It is essential to note that ferrite exhibits a body-centred cubic (BCC) crystal structure [56].

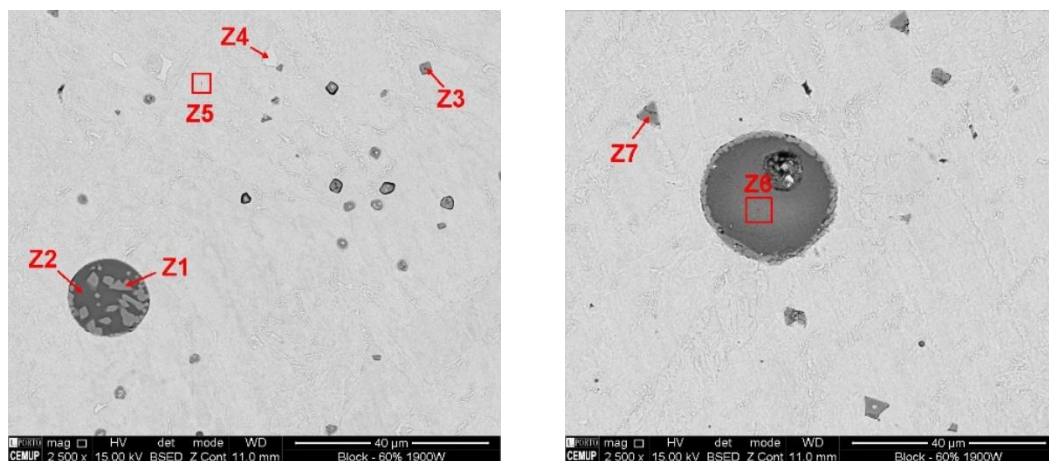


Figure 4.24 - SEM BEI images from the top surface of the deposited AISI P20+Ni material

Figure 4.24 shows localized analysis to identify dark particles seen in OM observations. The SEM-EDS analyse, Appendix G, confirmed that Z1, Z2, Z3, Z6 and Z7 correspond to oxides due to high concentrations of oxygen content. Notably, these spectra manifest elevated concentrations of chromium and manganese, clearly indicating the presence of corresponding oxides - specifically chromium oxide and manganese oxide. This way, the formation of these oxides can contribute to the reduction of Cr and Mn in the matrix of the printed material. Moreover, this decline is attributed to the migration of these elements to the slag, thereby promoting the

formation of oxides. Regrettably, this outcome holds potential drawbacks, as it has the capacity to compromise the mechanical properties of the printed material. Note that Chromium enhances the steel's corrosion resistance by forming a protective oxide layer on the surface, known as passivation. This is crucial for molds and dies used in environments where exposure to moisture or corrosive agents could occur. In the other hand, manganese enhances toughness and impact resistance, since it promotes the formation of fine-grained structures and helps prevent brittle fracture, making the material more resistant to cracking and impact loads [56].

4.4.1.3.3 Microhardness Measurements

Figure 4.25 presents a graph with a profile of Vickers microhardness along the printed multilayered volume.

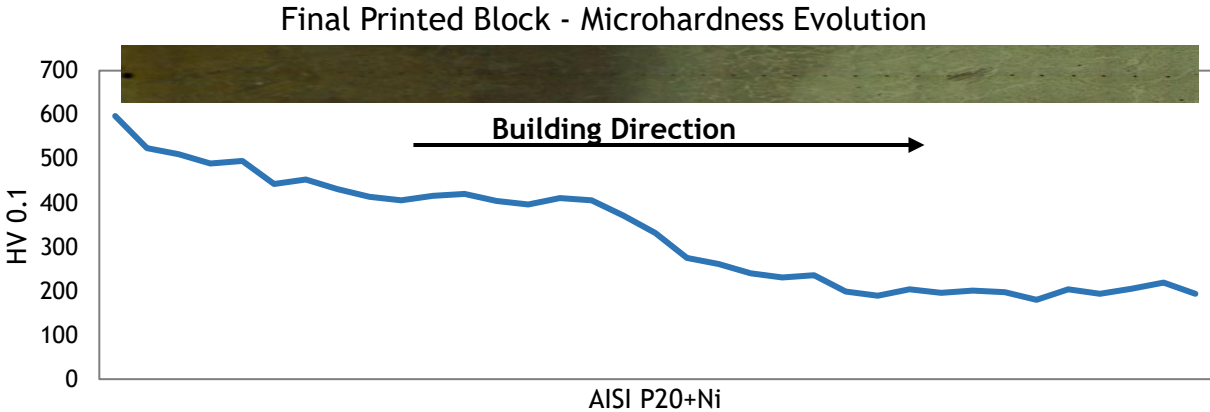


Figure 4.25 - Microhardness along the printed multilayered volume (deposited material)

The decrease in the Vickers microhardness values along the building direction is readily evident. As previous stated, in proximity to the substrate, a prevalence of martensite is observable, signifying elevated hardness values within that region. The diminution of hardness values along the build direction can be attributed to two principal factors. Initially, the decrease in the quantity of martensite dispersed through the material as the build progresses. Note that martensite is a hard and brittle phase. In contrast, the increase in the prevalence of oxides, particularly those of chromium, along the profile of the printed material. This increase in the concentration of chromium oxide implies a reduction of chromium content within the matrix. When chromium is available in the steel matrix, due to its strong affinity for carbon, there is formation of carbides [56]. These carbides are hard and contribute to the overall hardness of the material. However, since this element migrated to the slag, promoting the formation of oxides, it will not contribute to the improvement of hardness but its decrease along build direction.

Conclusions and Future Works

5.1 Conclusions

The primary objective of this study was to develop and characterize sustainable metal powders for utilization in additive manufacturing processes. This objective was achieved, yielding satisfactory outcomes.

AISI P20+Ni tool steel powder particles, from machining chips supplied from industry, were produced successfully through disc and planetary ball milling. In the case of disc milling, three distinct procedures were executed, and procedure number 1 for disc milling (PND 1) emerged as the most promising among the experimented methods. This procedure involved a milling duration of 75 minutes and led to the production of irregular and flake-like powder particles within the size range of 38 to 212 μm . This size range was specifically chosen for subsequent DED printings due to its favourable attributes in terms of tap density, loose density, and flowability when compared with the powder particles with size range of 53 and 150 μm . Consequently, the powder from PND 1, with particle sizes ranging from 38 to 212 μm , was selected for DED printing due to its superior energy efficiency and reduced time requirements. A total of 1500 grams of this selected metal powder was prepared for DED printing.

On the other hand, in the context of planetary ball milling, five different procedures were executed to determine the optimal approach for producing metal powder suitable for potential printing using selective laser melting (SLM) technology. Procedure number five (PNB 5) exhibited the most favourable outcomes when compared to the other methods, being one of the procedures with lowest total util milling time presented the best productivity, which has demonstrated the most favourable production time to production efficiency ratio. Powder from PNB 5 displayed a pronounced presence of cold-welding, leading to the formation of more rounded powder particles. However, due to constraints in time, density measurements and flowability evaluations were not conducted, and printing via SLM was not feasible due to the limited quantity of produced powder.

The DED printing process utilizing powder from PND 1 allowed for the deposition of feedstock on a non-preheated substrate. The process of identifying the optimal parameter combination for printing proved to be a challenging and time-consuming endeavour. Employing the DOE Taguchi L9 method, various parameter combinations were explored, and single lines were printed for assessment. Based on visual and geometrical analyses, the optimal parameter combination was determined. Subsequent parametrization involved the printing of five distinct single layers to study dilution percentage. The finalized parameters for printing the multilayered volume were established as follows: a laser power of 1900 W, a scanning speed of 6 mm/s, a powder feed rate of 8 g/min, and an overlapping of 60%. These parameters were employed for the construction of the multilayered volumes used for evaluating microstructure, porosity, chemical composition, and microhardness.

The analysis of the multilayered volume revealed defects at the interface between the substrate material, AISI 4140, and the deposited material, AISI P20+Ni. Specifically, lack of fusion and keyholing porosities were observed in the deposited

AISI P20+Ni, particularly near the interface. Furthermore, the microstructure of AISI P20+Ni exhibited variations along the build direction. An exploration of the chemical composition indicated a decline in chromium and manganese content within the steel matrix, leading to the formation of oxides. Furthermore, microhardness measurements were conducted, indicating a decrease in Vickers hardness values along the build direction. This decrease was attributed to the diminishing presence of martensite, which contributes to hardness, and the increased prevalence of oxides, particularly chromium oxide.

In conclusion, this study underscores the significance of parameter optimization in managing porosity and achieving desired material properties. The successful production and characterization of metal powders for AM processes, as well as the in-depth analysis of their behaviour in printing, contributes valuable insights to the realm of additive manufacturing.

5.2 Future Works

Upon the conclusion of this study, there remain avenues for further testing and experimentation to enhance and complete the scope of this research. These potential avenues for further research serve to amplify the comprehensiveness and depth of the undertaken work, providing a foundation for enhanced outcomes and expanded insights. The following suggestions are proposed for consideration:

- Conduct the milling process within a controlled atmosphere to prevent the occurrence of oxide formation in printed components.
- Execute Electron Backscatter Diffraction (EBSD) analyses on powder particles produced through planetary ball milling to elucidate the marked increase in hardness.
- Explore the potential benefits of printing on a preheated substrate to assess the feasibility of mitigating porosity defects.
- Perform Directed Energy Deposition printing within a controlled atmosphere.
- Undertake a heat treatment process on the printed multilayered volume to potentially elevate the mechanical properties of the material.
- Conduct wear tests to ascertain the viability of producing a functional coating.
- Pursue parameter optimization to approach the production of a near net shape part.
- Regarding powder production via planetary ball milling, perform density and flowability measurements, and proceed with printing utilizing Selective Laser Melting technology.
- Engage in the composition of a scientific article to disseminate the findings of this study.

References

- [1] Hernandez, Pedro M.; Campos, D.; Socorro, P.; Benitez, A.; Ortega, F.; Diaz, N. Electroforming applied to manufacturing of microcomponents. In *Mesic Manufacturing Engineering Society International Conference 2015*; Canela, J.M., Corral, I.B., Eds.; Elsevier Ltd.: Amsterdam, The Netherlands, 2015; Volume 132, pp. 655-662.
- [2] Batista, Catarina Duarte, Adriana André Martins das Neves de Pinho Fernandes, Maria Teresa Freire Vieira, and Omid Emadinia. "From Machining Chips to Raw Material for Powder Metallurgy—A Review." *Materials* 14, no. 18 (September 20, 2021): 5432. <https://doi.org/10.3390/ma14185432>
- [3] Broadbent, Clare. "Steel's Recyclability: Demonstrating the Benefits of Recycling Steel to Achieve a Circular Economy." *The International Journal of Life Cycle Assessment* 21, no. 11 (March 21, 2016): 1658-65. <https://doi.org/10.1007/s11367-016-1081-1>.
- [4] Metal Recycling Factsheet, EuRIC AISBL - Recycling: Bridging Circular Economy & Climate Policy, 2019.
- [5] Bendikiene, Regita, Antanas Ciuplys, and Lina Kavaliauskiene. "Circular Economy Practice: From Industrial Metal Waste to Production of High Wear Resistant Coatings." *Journal of Cleaner Production* 229 (August 2019): 1225-32. <https://doi.org/10.1016/j.jclepro.2019.05.068>.
- [6] Zhang, Jie; Gelin, Jean-Claude.; Sahli, M.; Barrière, Thierry. Manufacturing of 316L Stainless Steel Die Mold by Hot Embossing Process for Microfluidic Applications". *J. Micro Nano-Manuf.* 2013, 1, 041003.
- [7] Seifi, Mohsen, David L. Bourell, William Frazier, and Howard Kuhn, eds. *ASM Handbook, Volume 24: Additive Manufacturing Processes - 15.2 Particle Sizing*, 2020.
- [8] How to Obtain the Best Results with the Vibratory Disc Mill RS 200, Retsch GmbH, Germany.
- [9] Product Information - Vibratory Disc Mill RS 200 Retsch GmbH, 2016.
- [10] C. Suryanarayana, "Mechanical Alloying and Milling," *Progress in Materials Science*, p. 184, January 2007.
- [11] Wilkening, Martin, Andre Düvel, Florian Preishuber-Pflügl, Klebson da Silva, Stefan Breuer, Vladimir Šepelák, and Paul Heitjans. "Structure and Ion Dynamics of Mechanosynthesized Oxides and Fluorides." *Zeitschrift Für Kristallographie - Crystalline Materials* 232, no. 1-3 (September 22, 2016): 107-27. <https://doi.org/10.1515/zkri-2016-1963>.
- [12] Powder metallurgy - Vocabulary, ISO 3252:2019, 2019.
- [13] Oberg, Erik Jones, Franklin D. Horton, Holbrook L. Ryffel, Henry H. McCauley, Christopher J. Brengelman, Laura. (2020). *Machinery's Handbook (31st Edition) - 7.4.2.3 Friction and Flow Characteristics of Particles*. Industrial Press.
- [14] Mahboubi Soufiani, A., M.H. Enayati, and F. Karimzadeh. "Fabrication and Characterization of Nanostructured Ti6Al4V Powder from Machining Scraps." *Advanced Powder Technology* 21, no. 3 (May 2010): 336-40. <https://doi.org/10.1016/j.apt.2009.12.018>.
- [15] Afshari, Elham, and Mohammad Ghambari. "Characterization of Pre-Alloyed Tin Bronze Powder Prepared by Recycling Machining Chips Using Jet Milling." *Materials & Design* 103 (August 2016): 201-8. <https://doi.org/10.1016/j.matdes.2016.04.064>.
- [16] Rofman, O. V., A. S. Prosviryakov, A. V. Mikhaylovskaya, A. D. Kotov, A. I. Bazlov, and V. V. Cheverikin. "Processing and Microstructural Characterization of Metallic Powders Produced from Chips of AA2024 Alloy." *JOM* 71, no. 9 (June 11, 2019): 2986-95. <https://doi.org/10.1007/s11837-019-03581-x>.
- [17] Mendonça, Claudiney de Sales Pereira, Adhimar Flávio Oliveira, Leonardo Albergaria Oliveira, Manoel Ribeiro da Silva, Mirian de Lourdes Noronha Motta Melo, and Gilbert Silva. "Structural and Magnetic Properties of Duplex Stainless Steel (UNS S31803) Powders Obtained by High Energy Milling of Chips with Additions of NbC." *Materials*

- Research 21, no. 1 (October 30, 2017). <https://doi.org/10.1590/1980-5373-mr-2017-0717>.
- [18] A. López-Córdoba and S. Goyanes, "Food Powder Properties," in Reference Module in Food Science: Elsevier, 2017.
- [19] D. L. Bourell, W. Frazier, H. Kuhn, and M. Seifi, "16. Powder Characterization for Metal Additive Manufacturing," in ASM Handbook®, Volume 24 - Additive Manufacturing Processes: ASM International, 2020.
- [20] Bruno, Thomas J. Deacon, Ryan Jansen, Jeffrey A. Magdefrau, Neal Mueller, Erik Vander Voort, George F. Yang, Dehua. (2019). ASM Handbook, Volume 10 - Materials Characterization (2019 edition) - 6.2.4 Flowability of Powders. ASM International.
- [21] Standard Test Method for Flow Rate of Metal Powders, ASTM B 213 - 97, 1997.
- [22] Standard Test Methods for Flow Rate of Metal Powders Using the Carney Funnel, ASTM B 964 - 09, 2009.
- [23] O. D. Neikov and N. A. Yefimov, "Chapter 1 - Powder Characterization and Testing," in Handbook of Non-Ferrous Metal Powders (Second Edition). Oxford: Elsevier, 2019, pp. 3-62.
- [24] "Gas Pycnometer Belpycnol." Microtrac MRB. <https://www.microtrac.com/products/gas-adsorption-measurement/densitymeasurement/belpycno-l/>
- [25] Standard Test Method for Apparent Density of Free-Flowing Metal Powders Using the Hall Flowmeter Funnel, ASTM B 212 - 99, 1999.
- [26] Standard Test Method for Apparent Density of Non-Free-Flowing Metal Powders Using the Carney Funnel, ASTM B 417 - 00, 2000.
- [27] Standard Test Method for Determination of Tap Density of Metallic Powders and Compounds, ASTM B 527 - 93, 1993.
- [28] Standard Terminology for Additive Manufacturing Technologies, ASTM F2792- 12A, 2012.
- [29] Svetlizky, David, Mitun Das, Baolong Zheng, Alexandra L. Vyatskikh, Susmita Bose, Amit Bandyopadhyay, Julie M. Schoenung, Enrique J. Lavernia, and Noam Eliaz. "Directed Energy Deposition (DED) Additive Manufacturing: Physical Characteristics, Defects, Challenges and Applications." *Materials Today* 49 (October 2021): 271-95. <https://doi.org/10.1016/j.mattod.2021.03.020>.
- [30] E. Oberg, F. D. Jones, H. L. Horton, H. H. Ryffel, C. J. McCauley, and L. Brengelman, "7.4.9.4 Directed Energy Deposition (DED)," in *Machinery's Handbook* (31st Edition): Industrial Press, 2020.
- [31] I. Gibson, D. Rosen, and B. Stucker, *Additive Manufacturing Technologies - 3D Printing, Rapid Prototyping, and Direct Digital Manufacturing*, Second ed. London: Springer, 2015.
- [32] Bourell, David L. Frazier, William Kuhn, Howard Seifi, Mohsen. (2020). ASM Handbook®, Volume 24 - Additive Manufacturing Processes - 20.3.4 Motion. ASM International
- [33] D. L. Bourell, W. Frazier, H. Kuhn, and M. Seifi, "20.3 Components of Directed Energy Deposition Systems," in ASM Handbook®, Volume 24 - Additive Manufacturing Processes: ASM International, 2020.
- [34] R. M. Mahmood, S. I. P. AG, Ed. *Laser Metal Deposition Process Of Metals, Alloys, And Composite Materials*. 2018, p. 215.
- [35] Pei, Wei, Wei Zhengying, Chen Zhen, Li Junfeng, Zhang Shuzhe, and Du Jun. "Numerical Simulation and Parametric Analysis of Selective Laser Melting Process of AlSi10Mg Powder." *Applied Physics A* 123, no. 8 (July 25, 2017). <https://doi.org/10.1007/s00339-017-1143-7>.
- [36] Dass, Adrita, and Atieh Moridi. "State of the Art in Directed Energy Deposition: From Additive Manufacturing to Materials Design." *Coatings* 9, no. 7 (June 29, 2019): 418. <https://doi.org/10.3390/coatings9070418>.

- [37] Yang, Wei, Xiaoxun Zhang, Fang Ma, Sensen Dong, and Juzhe Jiang. "Selective Laser Melting of 1.2738 Mold Steel: Densification, Microstructure and Microhardness." *Materials Research Express* 8, no. 1 (January 1, 2021): 016525. <https://doi.org/10.1088/2053-1591/abd96a>.
- [38] Ferreira, André Alves, Rui Loureiro Amaral, Pedro Correia Romio, João Manuel Cruz, Ana Rosanete Reis, and Manuel Fernando Vieira. "Deposition of Nickel-Based Superalloy Claddings on Low Alloy Structural Steel by Direct Laser Deposition." *Metals* 11, no. 8 (August 22, 2021): 1326. <https://doi.org/10.3390/met11081326>.
- [39] Goodarzi, Dara Moazami, Joonas Pekkarinen, and Antti Salminen. "Effect of Process Parameters in Laser Cladding on Substrate Melted Areas and the Substrate Melted Shape." *Journal of Laser Applications* 27, no. S2 (February 1, 2015). <https://doi.org/10.2351/1.4906376>.
- [40] Mazzarisi, Marco, Sabina Luisa Campanelli, Andrea Angelastro, and Michele Dassisti. "Phenomenological Modelling of Direct Laser Metal Deposition for Single Tracks." *The International Journal of Advanced Manufacturing Technology* 111, no. 7-8 (October 20, 2020): 1955-70. <https://doi.org/10.1007/s00170-020-06204-x>.
- [41] Goodarzi, Dara Moazami, Joonas Pekkarinen, and Antti Salminen. "Effect of Process Parameters in Laser Cladding on Substrate Melted Areas and the Substrate Melted Shape." *Journal of Laser Applications* 27, no. S2 (February 1, 2015). <https://doi.org/10.2351/1.4906376>.
- [42] D. De Lange et al., "Influence of Intensity Distribution on the Meltpool and Clad Shape for Laser Cladding," *International Journal of Human Resources Development and Management*, January 2005.
- [43] E. Toyserkani, A. Khajepour, and S. Corbin, *Laser Cladding*. Florida: CRC Press, 2005, p. 280.
- [44] Wołosz, Patrycja, Agata Baran, and Marek Polański. "The Influence of Laser Engineered Net Shaping (LENSTM) Technological Parameters on the Laser Deposition Efficiency and Properties of H13 (AISI) Steel." *Journal of Alloys and Compounds* 823 (May 2020): 153840. <https://doi.org/10.1016/j.jallcom.2020.153840>.
- [45] Wołosz, Patrycja, Agata Baran, and Marek Polański. "The Influence of Laser Engineered Net Shaping (LENSTM) Technological Parameters on the Laser Deposition Efficiency and Properties of H13 (AISI) Steel." *Journal of Alloys and Compounds* 823 (May 2020): 153840. <https://doi.org/10.1016/j.jallcom.2020.153840>.
- [46] Park, Jun Seok, Joo Hyun Park, Min-Gyu Lee, Ji Hyun Sung, Kyoung Je Cha, and Da Hye Kim. "Effect of Energy Input on the Characteristic of AISI H13 and D2 Tool Steels Deposited by a Directed Energy Deposition Process." *Metallurgical and Materials Transactions A* 47, no. 5 (March 8, 2016): 2529-35. <https://doi.org/10.1007/s11661-016-3427-5>.
- [47] He, Jeremy. n.d. "DIN 1.2738 Steel | AISI P20+Ni Tool Steel." Otai Special Steel. Accessed March 10, 2023. <https://www.astmsteel.com/product/1-2738-steel-p20-ni-tool-steel/>.
- [48] "DIN 1.2738 Tool Steel | AISI P20+Ni." n.d. Halden Special Steel. <https://www.round-bars.com/products/din-1-2738-tool-steel-aisi-p20ni/>.
- [49] AZO Materials. 2019. "AISI 4140 Alloy Steel (UNS G41400)." AZoM.com. August 7, 2019. <https://www.azom.com/article.aspx?ArticleID=6769>.
- [50] Emadinia, Omid. 2020. "Application of Disk Milling to Produce Metal Powder from Industrial Chips." In *Euro PM2020 Virtual Congress*.
- [51] Castanheira, Lara. "Production of Sustainable Powders for Direct Energy Deposition (DED)". Master's dissertation, University of Porto, 2022.
- [52] Standard Test Method for Sieve Analysis of Metal Powders, ASTM B214, 2016.
- [53] *Metallic materials – Vickers hardness test – Part 1: Test method*, ISO 6507-1, 2018.
- [54] Monteiro, Luca. "Production of Tools by Additive Manufacturing for Tube Bending Machines". Master's dissertation, University of Porto, 2023.

- [55] Fullenwider, Blake, Parnian Kiani, Julie M. Schoenung, and Kaka Ma. "Two-Stage Ball Milling of Recycled Machining Chips to Create an Alternative Feedstock Powder for Metal Additive Manufacturing." *Powder Technology* 342 (January 2019): 562-71. <https://doi.org/10.1016/j.powtec.2018.10.023>.
- [56] Santos, Henrique. 2017. *Tratamentos Térmicos*.
- [57] Ostolaza, Marta, Jon Iñaki Arrizubieta, Aitzol Lamikiz, and Magdalena Cortina. "Functionally Graded AISI 316L and AISI H13 Manufactured by L-DED for Die and Mould Applications." *Applied Sciences* 11, no. 2 (January 15, 2021): 771. <https://doi.org/10.3390/app11020771>.
- [58] Baek, Gyeong Yun, Gwang Yong Shin, Eun Mi Lee, Do Sik Shim, Ki Yong Lee, Hi-Seak Yoon, and Myoung Ho Kim. "Mechanical Characteristics of a Tool Steel Layer Deposited by Using Direct Energy Deposition." *Metals and Materials International* 23, no. 4 (July 2017): 770-77. <https://doi.org/10.1007/s12540-017-6442-1>
- [59] Joshi, Sameehan S., Shashank Sharma, Sangram Mazumder, Mangesh V. Pantawane, and Narendra B. Dahotre. "Solidification and Microstructure Evolution in Additively Manufactured H13 Steel via Directed Energy Deposition: Integrated Experimental and Computational Approach." *Journal of Manufacturing Processes* 68 (August 2021): 852-66. <https://doi.org/10.1016/j.jmapro.2021.06.009>.
- [60] Arrizubieta, Jon Iñaki, Magdalena Cortina, Arantza Mendioroz, Agustín Salazar, and Aitzol Lamikiz. "Thermal Diffusivity Measurement of Laser-Deposited AISI H13 Tool Steel and Impact on Cooling Performance of Hot Stamping Tools." *Metals* 10, no. 1 (January 20, 2020): 154. <https://doi.org/10.3390/met10010154>.
- [61] Son, Jong Youn, Hi Seak Yoon, Ki Yong Lee, Sang Hu Park, and Do Sik Shim. "Investigation into High-Temperature Interfacial Strength of Heat-Resisting Alloy Deposited by Laser Melting Process." *Metals and Materials International* 26, no. 3 (July 3, 2019): 384-94. <https://doi.org/10.1007/s12540-019-00335-x>.
- [62] Lee, Seulbi, Jaewoong Kim, Do-Sik Shim, Sang-Hu Park, and Yoon Suk Choi. "Micro-Cracking in Medium-Carbon Steel Layers Additively Deposited on Gray Cast Iron Using Directed Energy Deposition." *Metals and Materials International* 26, no. 5 (January 3, 2020): 708-18. <https://doi.org/10.1007/s12540-019-00589-5>.
- [63] Telasang, Gururaj, Jyotsna Dutta Majumdar, Nitin Wasekar, G. Padmanabham, and Indranil Manna. "Microstructure and Mechanical Properties of Laser Clad and Post-Cladding Tempered AISI H13 Tool Steel." *Metallurgical and Materials Transactions A* 46, no. 5 (February 24, 2015): 2309-21. <https://doi.org/10.1007/s11661-015-2757-z>.
- [64] Borges, B., L. Quintino, Rosa M. Miranda, and Phil Carr. "Imperfections in Laser Cladding with Powder and Wire Fillers." *The International Journal of Advanced Manufacturing Technology* 50, no. 1-4 (December 22, 2009): 175-83. <https://doi.org/10.1007/s00170-009-2480-2>.
- [65] Joshi, Sameehan S., Abhishek Sharma, Shashank Sharma, Sangram Mazumder, Mangesh V. Pantawane, Srinivas A. Mantri, Rajarshi Banerjee, and Narendra B. Dahotre. "Cyclic Thermal Dependent Microstructure Evolution During Laser Directed Energy Deposition of H13 Steel." *Transactions of the Indian Institute of Metals* 75, no. 4 (February 28, 2022): 1007-14. <https://doi.org/10.1007/s12666-022-02544-2>.
- [66] Masaylo, Dmitriy, Sergei Igoshin, Anatoly Popovich, Alexey Orlov, Artem Kim, and Vera Popovich. "Microstructural and Hardness Behavior of H13 Tool Steel Manufactured by Ultrasound-Assisted Laser-Directed Energy Deposition." *Metals* 12, no. 3 (March 5, 2022): 450. <https://doi.org/10.3390/met12030450>.

Appendices

Appendix A: Accepted conference submission to ESIAM23

Upcycling a Tool Steel Residue for Additive Manufacturing Application

Mariana Cunha¹, Fahad Zafar¹, Omid Emadina^{2*}, Manuel. Vieira^{1,2}

1 Faculdade de Engenharia, Universidade do Porto, s/n, R. Dr. Roberto Frias, 4200-465 Porto, Portugal

2 LAETA/INEGI: Instituto de Ciência e Inovação em Engenharia Mecânica e Engenharia Industrial, Campus da FEUP, R. Dr. Roberto Frias 400, 4200-465 Porto, Portugal

*Correspondence: oemadina@inegi.up.pt

Abstract:

Metal residues from machining industry usually go through downcycling approach. Adding value to these new raw materials is noteworthy giving new life for other applications. This objective can be attained through solid and/or fusion processing such as mechanical milling and gas atomization, respectively, to produce feedstocks for powder metallurgy applications. However, production efficiency and powder characteristics (such as particle size, shape, size distribution, surface area, and powder properties including density and flowability) are essential.

This study investigated the upcycling of AISI P20+Ni steel chips for additive manufacturing (AM) purposes. The powder production involved two different techniques i.e., vibratory disc milling (VDM) and planetary ball milling (PBM). Directed energy deposition (DED) and Laser powder bed fusion (L-PBF) can be solutions to use these upcycled powders. Thus, the milled powders were sieved to analyse the production efficiency. Then, the size range of 38-212 μm was selected for DED and that of 20-53 μm for L-PBF. Regarding the VDM process, the milling time was variable whereas the rpm varied for the PBM as well as time. These changes were performed to optimize the efficiency and powder characteristics.

Powders produced by VDM presented a flaky morphology whereas those produced by PBM had rounded shape. Microstructural analysis and microhardness analyses were also performed to evaluate the consolidation of the particles and work-hardening effect. Although the VDM powder was not spherical, it was tested for the DED process, lines were printed and evaluated for the bead and dilution analyses, correlated with energy density. Then, some blocks were printed for microstructural, chemical and hardness analyses. This study concludes that the upcycled AISI P20+Ni feedstock is printable by DED though it requires strict atmospheric control during milling and printing. Moreover, further optimizations should be taken into account to achieve a chemical composition stability in the printed alloy.

Key words: upcycling; additive manufacturing; mechanical milling, powder characteristics, microstructure, and mechanical properties

Appendix B: Review on Printings of Tool Steels

Table A.1 - Review on printings of tool steels.

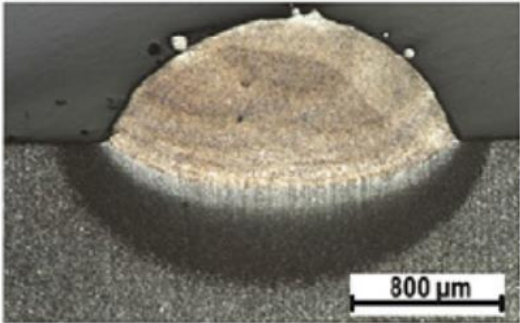
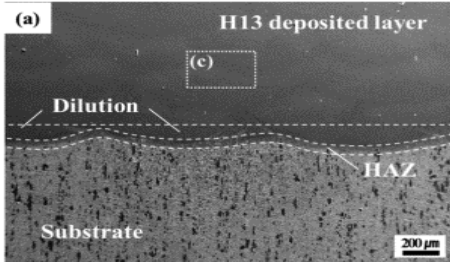
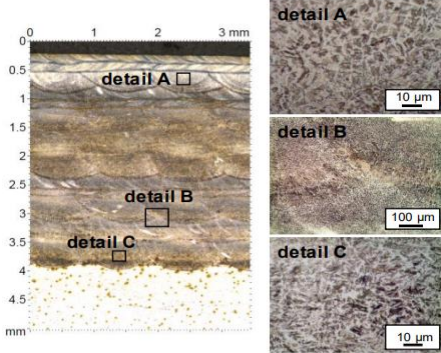
Reference	Alloy	Particle Size and Shape	Substrate	Process/Application	Objectives	Carrying Gas; Flow Rate	Volume Energy Density	Laser Spot Size	Laser Power	Scanning Speed	Powder Feeding Rate	Conclusions
[46]	AISI H13	100µm; Spherical	Wrought H13	DED	Studying the effect of varying the energy input, by fixing the powder feeding rate, scanning speed and the laser beam diameter.	Argon	37.81-88.21 J/mm ²	0.56 mm	-	850 mm/min	3.42 g/min	The height of the deposited layer increased with the energy input and also increased with the powder-feeding rate with the same energy input; A larger molten alloy puddle was formed on the substrate with relatively higher energy input. Average hardness slightly decreased with increasing energy input
[57]	AISI H13/AISI 316 L	H13: 53-150µm 316L: 45-125µm		DED	A functionally graded material composed of AISI 316L to AISI H13 was manufactured, and its microstructure and hardness analysed.	Argon	-	1.8 mm	600-625 W	450-550 mm/min	H13: 0-3.3 g/min 316L: 0-5 g/min	Linear variation of the constituents does not always result in linear variation of the properties. Severe crackings and several lack of fusion.
[58]	AISI H13	120µm; Spherical	D2	DED	Microstructure observation, hardness, wear, and impact tests were conducted to examine the mechanical and metallurgical properties of the sample. The resulting properties were then compared to the heat-treated tool steel.	Argon	-	1.00 mm	900 W	850 mm/min	5 g/min	The microstructures of the deposited H13 specimens reveal fine cellular-dendrite solidification structures resulting from the melting and rapid cooling process. Notably, the H13-deposited specimen demonstrated exceptional toughness in the impact test, exhibiting quasi-cleavage fracture morphology and displaying high total absorption energy. The study suggests that the deposited H13 layer is effective for forming dies requiring high toughness.
[59]	AISI H13	D10-60µm D50-90µm D50-110µm	-	DED	Studying the effect of varying the processing parameters on the microstructure and phase evolution in L-DED samples.	-	77-30 J/mm ²	1.00 mm	350 W	348 588 888 mm/min	-	The findings revealed a cellular structure in the samples, with varying morphologies and concentrations of solute elements depending on laser fluence and identified the dominant post-heating effects on microstructural transformations in different regions of the samples.
[60]	AISI H13	53-150µm; Spherical	AISI 1045	DED	Studying the thermal diffusivity of laser-deposited AISI H13 measured experimentally using flash and lock-in thermography	Argon	-	-	600 W	450 mm/min	3.3 g/min	The thermal diffusivity of laser-deposited AISI H13 tool steel was lower than that of the reference cast material. The reduction in thermal diffusivity was attributed to the microstructure developed during rapid cooling, where the fine grain size hindered heat transfer. No defects were found at interface between the AISI H13 and substrate AISI 1045.

Reference	Alloy	Particle Size and Shape	Substrate	Process/Application	Objectives	Carrying Gas; Flow Rate	Volume Energy Density	Laser Spot Size	Laser Power	Scanning Sped	Powder Feeding Rate	Conclusions
[61]	AISI H13	50-150µm; Spherical	SKG61	DED	In this study, the interfacial strength between a hot work tool steel H13 deposited on an SKD61 steel substrate using direct energy deposition (DED) process was investigated.	Argon	-	-	900W	850 mm/min	5.5 g/min	Remarkably, no cracks or delamination were observed at the cross-section of the specimen, highlighting the effectiveness of the DED process. Shear tests were conducted at various temperatures, revealing that while cracks initiated in the deposited region at room temperature, fracture occurred only in the substrate regions at higher temperatures. Nevertheless, the interface exhibited remarkable bonding strength as no interfacial cracking or delamination was observed across all test temperatures.
[62]	AISI H13	Mean size of 87 µm. Powder size distribution of 63 µm (D10), 84 µm (D50) and 115 µm (D90); spherical	Gray cast iron	DED	DED technique was employed to additively deposit AISI H13 powders onto gray cast iron, forming both single tracks and multi-layers. To comprehend the formation of micro-cracks, a comprehensive analysis was conducted, involving multi-scale microstructure characterization, along with thermal analysis utilizing finite element method.	-	-	-	900 W	850 mm/min	5 g/mm	In the single-track deposition, no cracks were detected; however, cracks were observed in the single-layer, double-layer, and even triple-layer depositions. Additionally, micro-pores were observed along the melt flow next to the graphite in the substrate in both single-layer and double-layer depositions.
[63]	AISI H13	100 µm; Spherical	AISI H13	Laser Cladding	In this study, a comprehensive analysis was conducted to examine the microstructure and mechanical properties, specifically wear resistance and tensile strength, of a hardened and tempered AISI H13 tool steel substrate. The investigation involved laser cladding with AISI H13 tool steel powder, both in its as-clad state and after undergoing post-cladding conventional bulk isothermal tempering through heat treatment at 823 K (550 °C) for 2 hours.	Argon	133 J/mm ²	-	-	-	-	The laser-clad zone exhibits a combination of martensite, retained austenite, and carbides with high hardness. Isothermal tempering transforms the microstructure into tempered martensite with uniformly dispersed carbides. The laser cladding process induces residual compressive stress, which decreases after tempering. Micro-tensile testing reveals brittle failure in specimens machined across or transverse to the cladding direction, while samples sectioned parallel to the cladding direction exhibit ductile failure with elongation. Additionally, the laser-clad and post-cladding tempered samples demonstrate superior wear resistance compared to conventionally treated AISI H13 tool steel.
[44]	H13	44-150µm	X37CrMoV 5-1 steel rod	Laser Cladding	The study investigated the impact of various technological parameters on the efficiency of cladding geometry and the properties of the deposited material. Specifically, changes were made to the laser spot diameter, powder flow rate, and deposition velocity, while maintaining a constant laser power.	Argon		1.63 1.76 1.85 mm	500 W	120 240 360 480 600 mm/min	4.76 5.89 g/min	Based on their findings, the study concludes that the highest efficiency was achieved at a lower scanning velocity. Furthermore, the dimensions of the clads decrease with higher scanning velocity and lower mass powder flow rate. The refinement of the microstructure is influenced by both the scanning velocity and the size of the laser spot.

Reference	Alloy	Particle Size and Shape	Substrate	Process/Application	Objectives	Carrying Gas; Flow Rate	Volume Energy Density	Laser Spot Size	Laser Power	Scanning Speed	Powder Feeding Rate	Conclusions
[64]	AISI H13		AISI H13	Laser Cladding	The goal of this work is to address the need for manufacturing guidelines and procedures in laser cladding, aiming to reduce defects and enhance service quality and productivity in both component repair and manufacturing processes. The study focuses on shape and microstructural defects commonly observed in laser clads, including contact angle, total clad height, lack of fusion, porosity, and cracks. By investigating the use of filler wire and powder on various substrates, the research aims to provide an overview of prevalent defects and propose strategies to minimize their occurrence in real productive environments	-		0.6 mm	700 W	600 mm/min	14 g/min	Powder-based cladding exhibits a higher deposition rate compared to wire-based cladding, indicating greater productivity. Moreover, powder clads tend to have smoother and more regular shapes, while wire clads are more sensitive to factors like wire feeding rate and positioning relative to the laser beam and substrate. Porosity is more prevalent in powder clads due to gas absorption, but it can be mitigated by increasing the total heat input. However, this may increase the risk of hot cracking in certain alloys. Cold cracking, on the other hand, is more likely in wire clads due to rapid cooling and limited ductility, but it can be prevented with immediate annealing following the laser cladding process.
[65]	H13	D10-60µm D50-90µm D90-110µm; Spherical	-	DED	In this study, the evolution of finescale microstructure in H13 steel fabricated through laser directed energy deposition was investigated. Analysis techniques such as X-ray diffraction, scanning electron microscopy, and site-specific transmission electron microscopy were employed.	-	77 J/mm ²	-	350 W	348 mm/min	9.5 g/min	. The findings revealed cellular solidification of austenite grains followed by their transformation into ferrite/martensite, with the presence of carbide-rich precipitates at cell boundaries and junctions. Site-specific transmission electron microscopy further identified these precipitates as Mo-V and Cr-rich carbides, while the martensitic matrix contained pockets of retained austenite.
[45]	H13	<45µm-4.99% 45<x<106µm-94.76% >106µm-0.25%	CuBe	Direct Laser metal deposition	The objective of this study is to utilize direct laser metal deposition (DLMD) to deposit a single-layer of H13 tool steel cladding onto a precipitation hardening copper-beryllium (CuBe) alloy substrate. The research focuses on optimizing process parameters such as laser power, powder feed rate, overlap ratio, and substrate temperature at a scan speed of 1000 mm/min for both single-track and single-layer cladding. The quality of the cladding is assessed based on its geometrical features, defects, interfacial adhesion, and the potential impact on substrate over-aging.	Argon			1600 1800 2000 2200 W	1000 mm/min	8 10 12 16 g/min	This study examined the influence of powder feed rate and laser power on various aspects of single-track samples in laser cladding. The research focused on cross-section geometrical features, interfacial adhesion, defects distribution, and microhardness. Optimal results were obtained with relatively high laser power (1800-2200 W) and intermediate powder feed rate (8-12 g/m) at a processing speed of 1000 mm/min. These parameters were found to be effective in achieving high-quality cladding tracks while maximizing energy and powder efficiency. Lack-of-fusion and gas -entrapment were observed.
[66]	H13	45-90µm (d10 = 53 µm d50 = 72 µm d90 = 91 µm))	-	DED	The primary objective of this paper is to address the issue of anisotropic mechanical properties in metal additive manufacturing using Laser-Directed Energy Deposition (L-DED). By introducing US assistance and employing a specially designed cooling system, the research aims to investigate the impact on the grain structure and mechanical properties of the L-DED-produced samples. Additionally, the study incorporates post-process heat treatments such as annealing, quenching, and tempering to further enhance the material properties and evaluate their influence on anisotropy reduction.	Argon		3 mm	1200 W	720 mm/s	15g/min	This study showcased a promising application of ultrasonic (US) assistance in the laser-directed energy deposition (L-DED) process for H13 tool steel. The use of US assistance resulted in the formation of an equiaxed microstructure, enhancing both the microstructural and mechanical uniformity in samples with smaller heights. Notably, the H13 tool steel exhibited a more refined equiaxed microstructure characterized by an increased number of third-order dendrites. Additionally, the US assistance effectively eliminated "keyhole" defects that are commonly observed in molten conventional L-DED materials.

Appendix C: Selection of printing parameters for DED

Table A.2 - Articles considered for the selection of the printing parameters.

Reference	Laser Power [W]	Scanning Speed [mm/min]	Powder Feed Rate [g/min]	Cross Section
[44]	500	120	5,89	
[54]	900	850	5	
[56]	600	450	3,3	

Appendix D: Chemical Composition of Metal Chips and Powders for DED and SLM technology

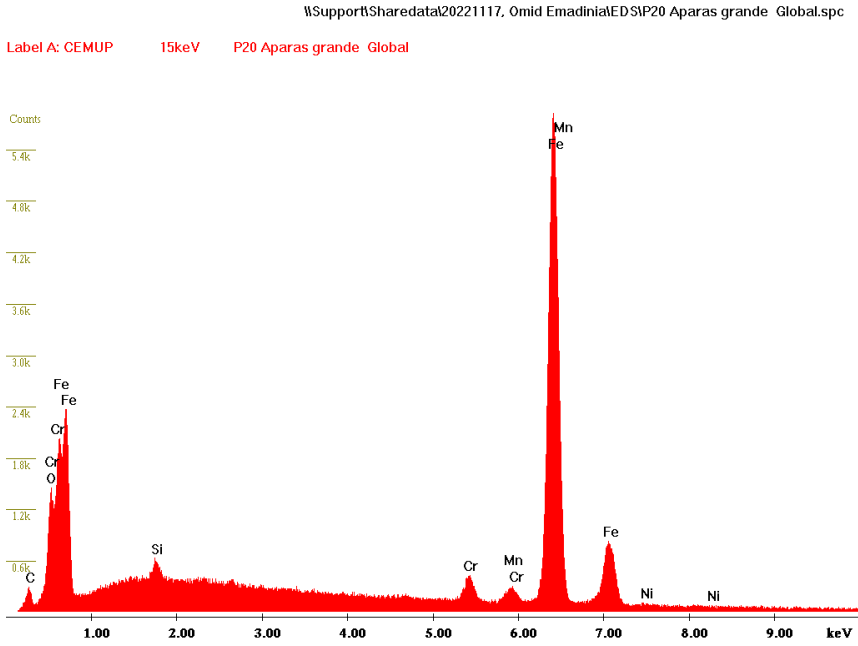


Figure A.1 - EDS spectra of AISI P20+Ni metal chip

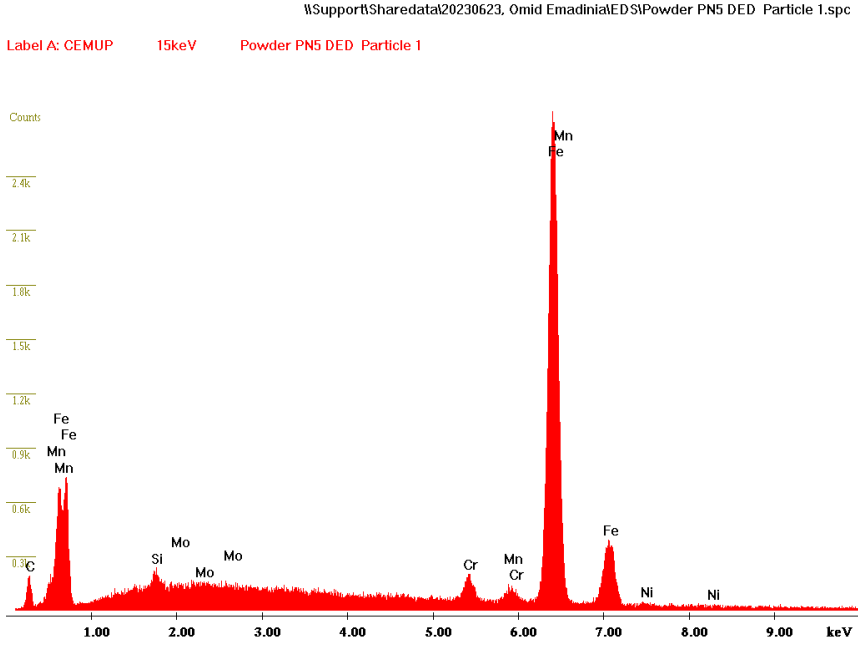


Figure A.2 - EDS spectra of powder particle with size range between 38 and 212 μm from PND 1 (Sample 1).

Label A: CEMUP 15keV Powder PN5 DED Particle 2

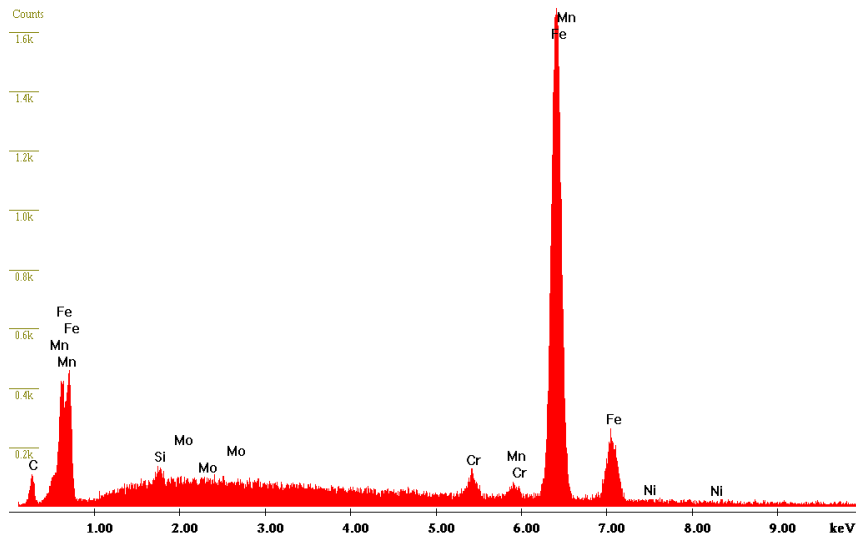


Figure A.3 - EDS spectra of powder particle with size range between 38 and 212 μm from PND 1 (Sample 2).

Label A: CEMUP 15keV P20 Ni BM 20 < 53 Particle 1

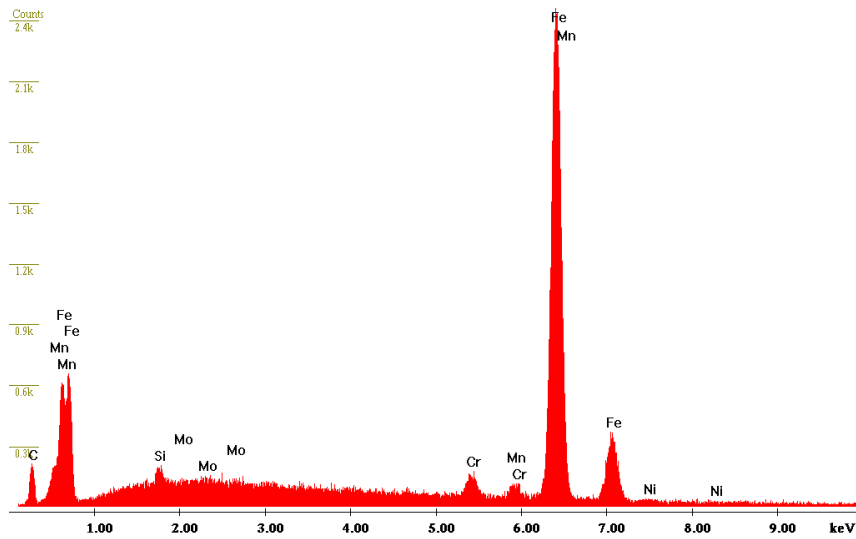


Figure A.4 - EDS spectra of powder particle with size range between 20 and 53 μm from PNB 1 (Sample 1).

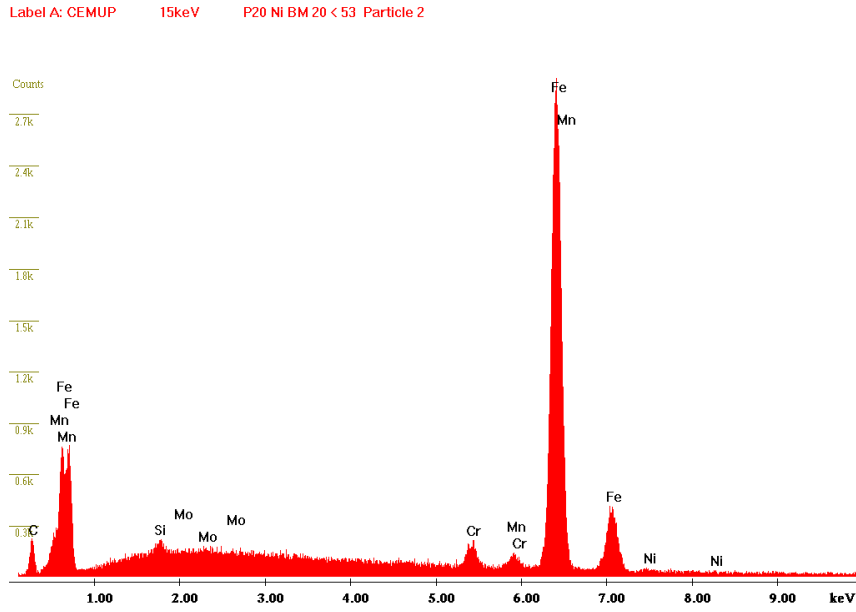


Figure A.2 - EDS spectra of powder particle with size range between 20 and 53 μm from PNB 1 (Sample 2).

Appendix E: OM images illustrating the indentations resulting from Vickers hardness tests.

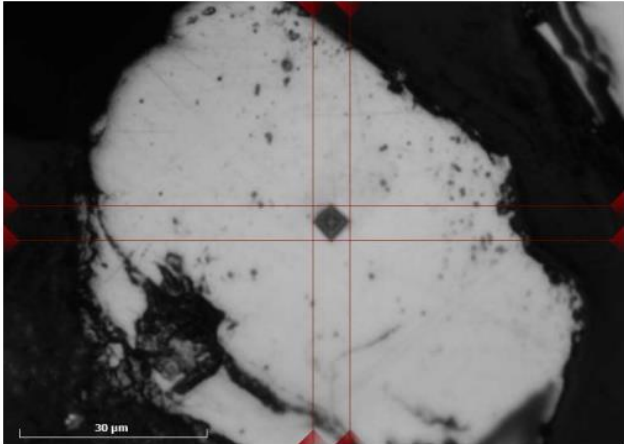


Figure A.3 - OM Image from indentation (536 HV 0.01) from metal chip

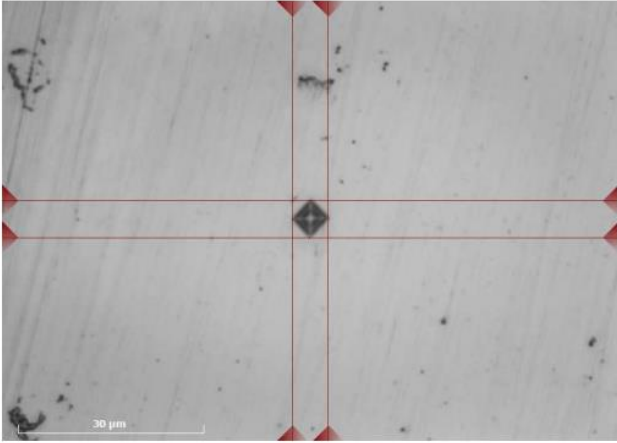


Figure A.4 - OM Image from indentation (559 HV 0.01) from powder particle produced by disc milling (PND 1) - (38<x<212 μm)

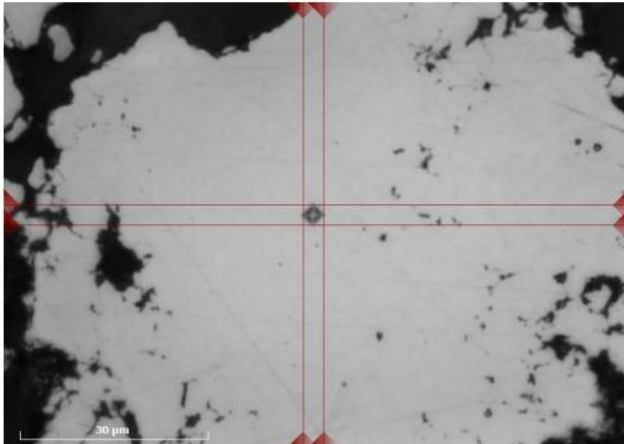


Figure A.4 - OM Image from indentation (1752 HV 0.01) from powder particle produced by planetary ball milling (PNB 1) - (20<x<53 μm)

Appendix F: Cross section views from one layered printing

Table A.3- Combination of printing parameters and porosity area for one-layered printing samples

One-layered Printing	Laser power [W]	Scanning Speed [mm/s]	Powder Feed Rate [g/min]	Overlapping [%]	Porosity area [mm ²]
A	1800	6.0	8.0	40	0.23
B				50	0.33
C				60	0.16
D	1900			50	0.17
E				60	0.28

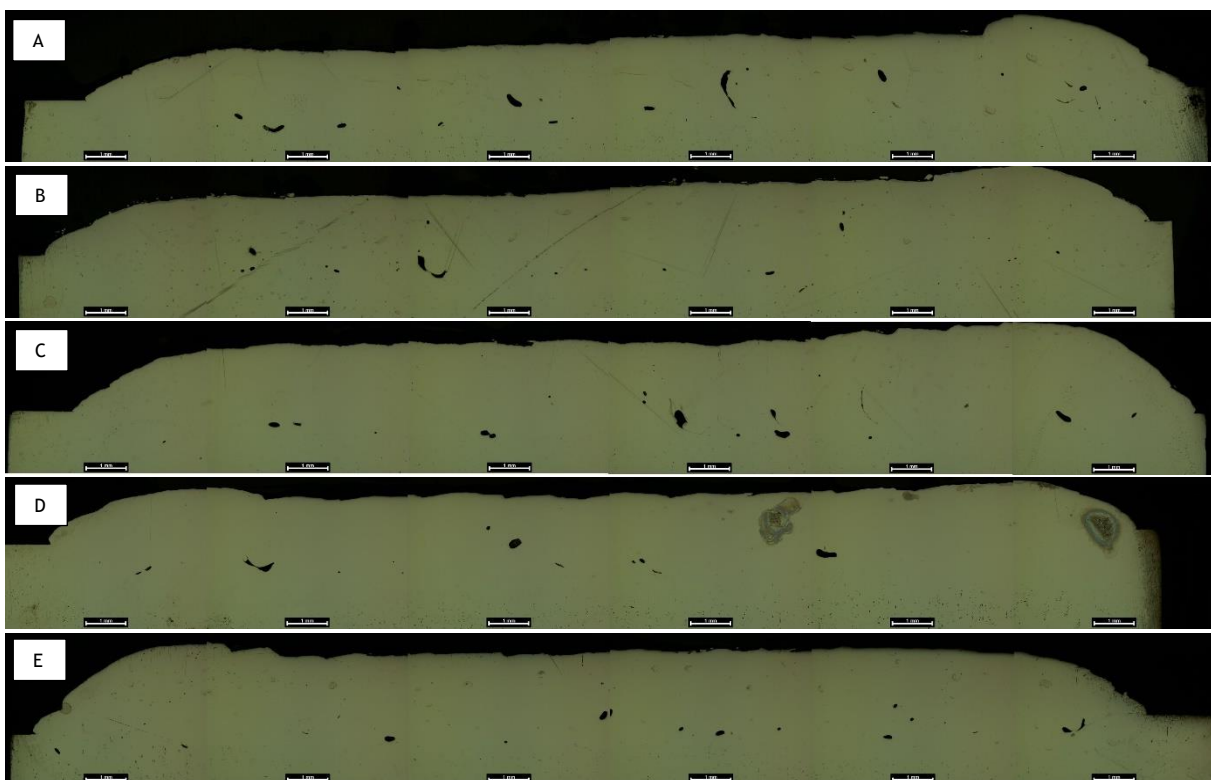


Figure A.7 - Cross section view of one-layered printings

Appendix G: EDS Spectra images from the printed multilayered volume

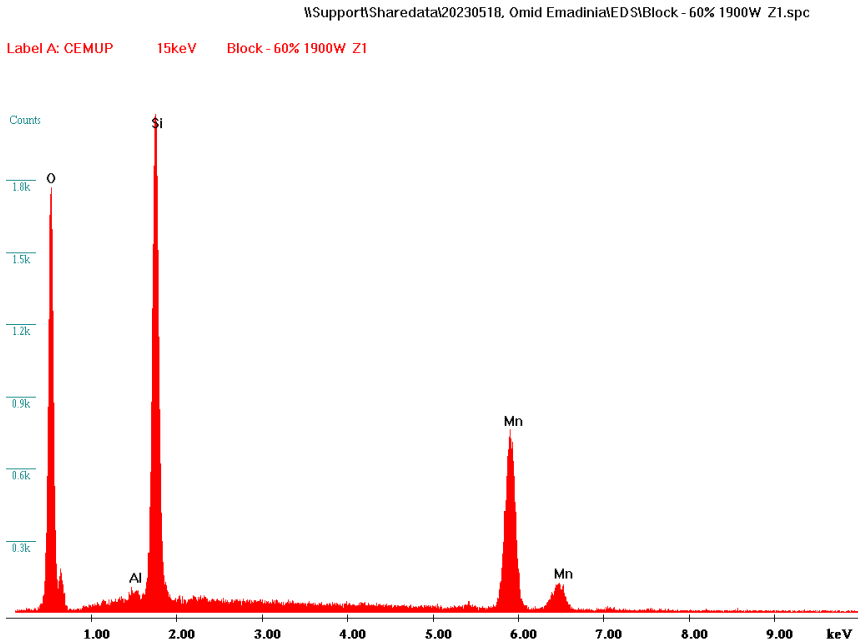


Figure A.8- EDS punctual spectra of Zone 1 from printed multilayered volume.

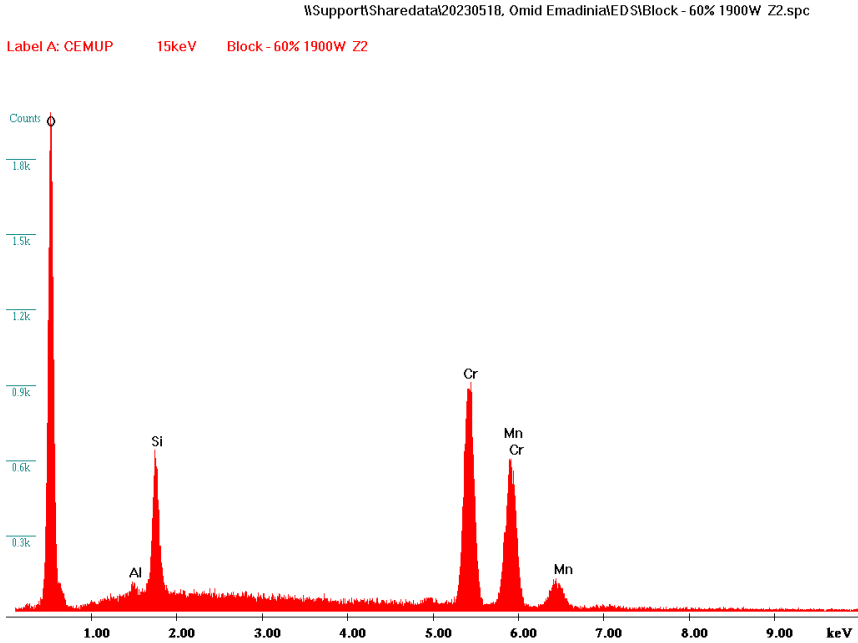


Figure A.9 - EDS punctual spectra of Zone 2 from printed multilayered volume.

Label A: CEMUP 15keV Block - 60% 1900W_Z3

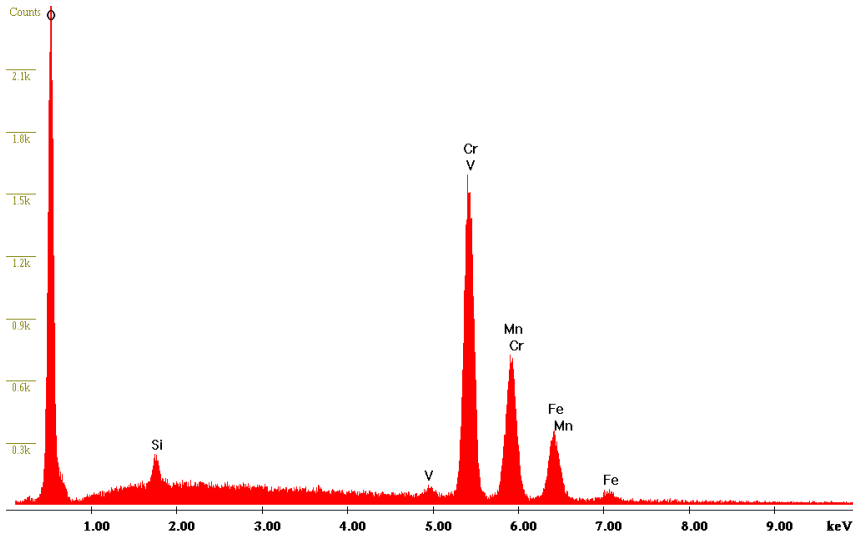


Figure A.10 - EDS punctual spectra of Zone 3 from printed multilayered volume.

Label A: CEMUP 15keV Block - 60% 1900W_Z4

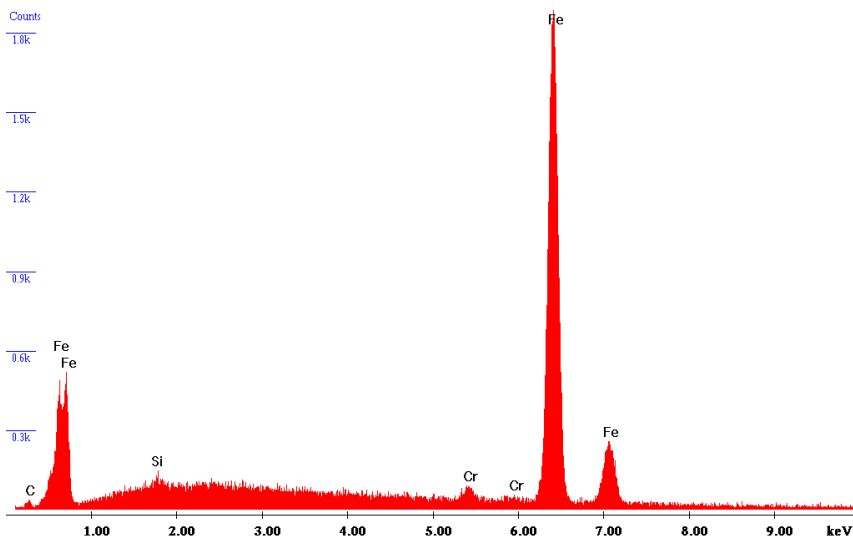


Figure A.11 - EDS punctual spectra of Zone 4 from printed multilayered volume.

Label A: CEMUP 15keV Block - 60% 1900W_Z5

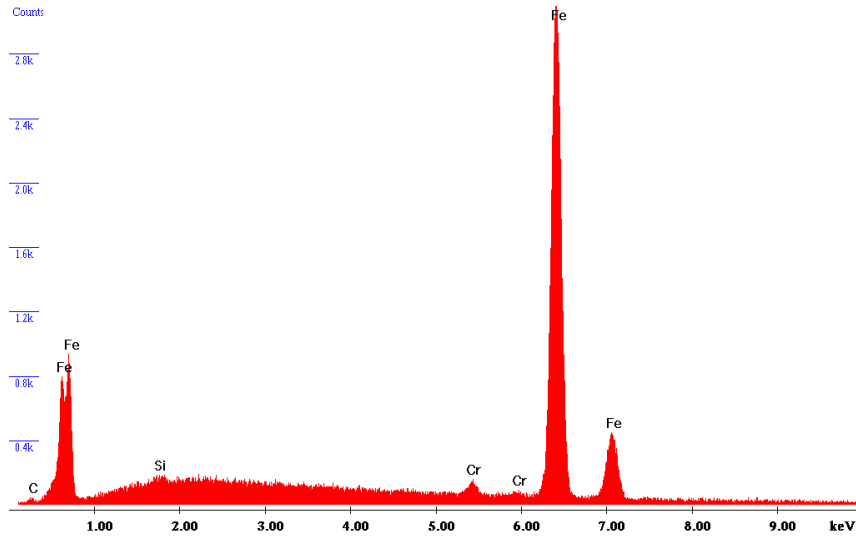


Figure A.12 - EDS punctual spectra of Zone 5 from printed multilayered volume.

Label A: CEMUP 15keV Block - 60% 1900W_Z6

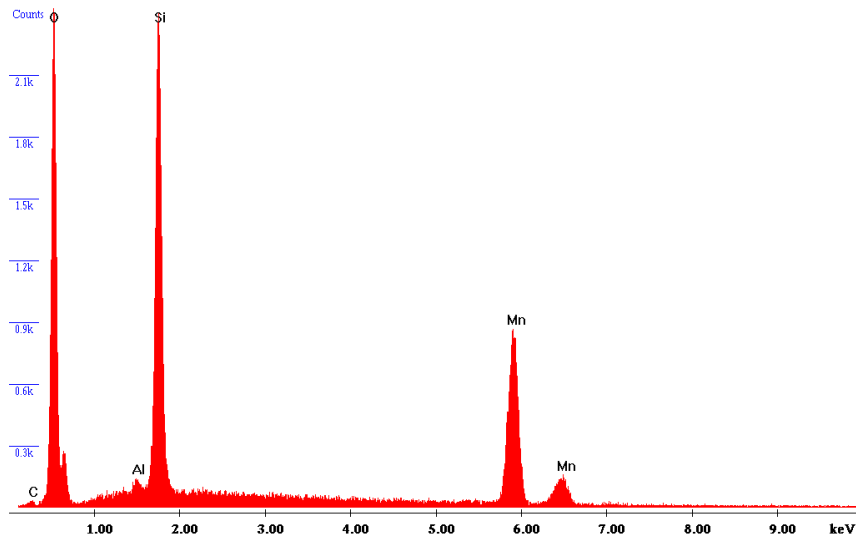


Figure A.13 - EDS punctual spectra of Zone 6 from printed multilayered volume.

Label A: CEMUP 15keV Block - 60% 1900W Z7

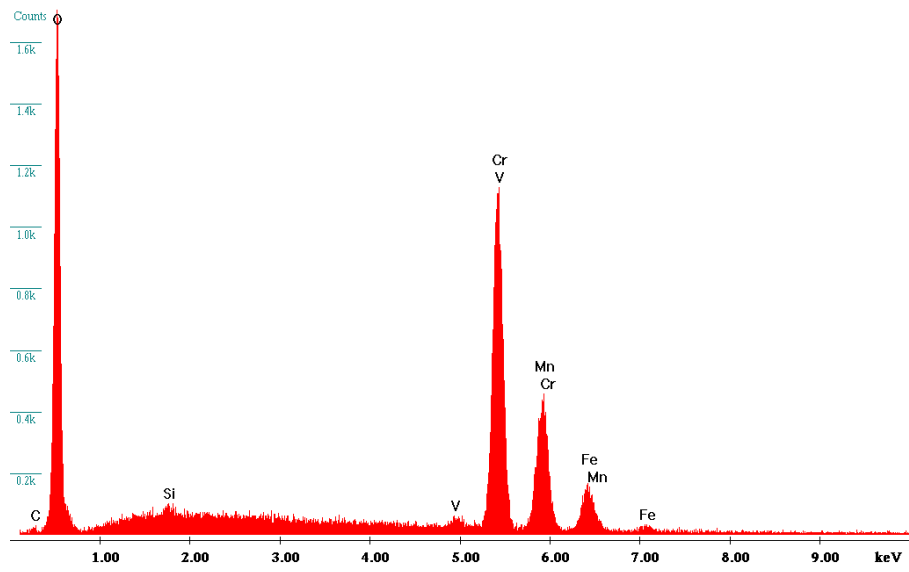


Figure A.14 - EDS punctual spectra of Zone 7 from printed multilayered volume.

Appendix H: Chemical Composition Profile for the printed multilayered volume

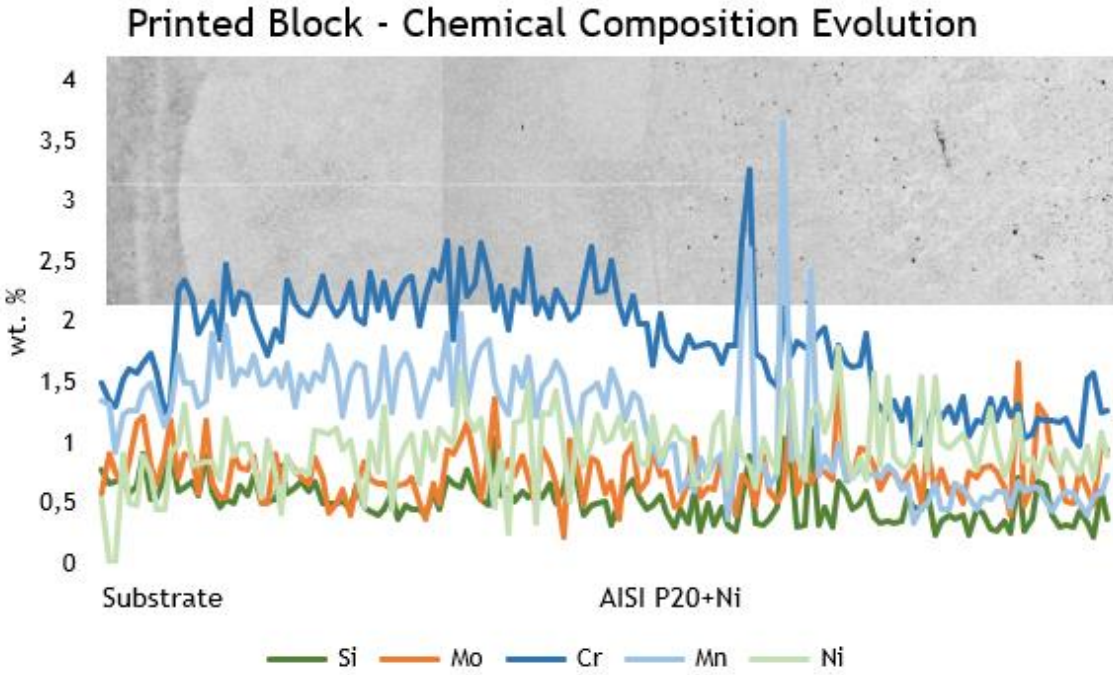


Figure A.15 - Chemical Composition profile for the printed multilayered volume